UNIVERSIDADE DE BRASÍLIA

INSTITUTO DE GEOSCIÊNCIAS

PROGRAMA DE PÓS-GRADUAÇÃO EM GEOLOGIA

ARTHUR SANTOS DA SILVA

DISSERTAÇÃO DE MESTRADO Nº 473

AREA DE CONCENTRAÇÃO: MINERALOGIA E PETROLOGIA

METAMORFISMO DE *UHT* E *HP* NO DOMÍNIO BACAJÁ, CRÁTON DO AMAZONAS

BRASÍLIA - DF

2021

ARTHUR SANTOS DA SILVA

DISSERTAÇÃO DE MESTRADO Nº 473

METAMORFISMO DE *UHT* E *HP* NO DOMÍNIO BACAJÁ, CRÁTON DO AMAZONAS

Dissertação apresentada à Universidade de Brasília, como requisito parcial do Programa de Pós-Graduação em Geologia para a obtenção do título de Mestre em Geologia.

Área de concentração: Mineralogia e Petrologia

Profº Dr. Elton Luiz Dantas

Orientador

Profº Dra. Eliza Inez Nunes Peixoto

Co-orientadora

BRASÍLIA-DF

2021

Ficha catalográfica elaborada automaticamente,
com os dados fornecidos pelo(a) autor(a)

SS586m
Santos da Silva, Arthur
Metamorfismo de UHT e HP no domínio Bacajá, Cráton do Amazonas / Arthur Santos da Silva; orientador Elton Luiz Dantas; co-orientador Eliza Inez Nunes Peixoto. -- Brasília, 2021.
132 p.

Dissertação (Mestrado - Mestrado em Geologia) -- Universidade de Brasília, 2021.

1. Metamorfismo. 2. Granulito. 3. Paleoproterozoico. 4. Modelamento metamórfico. 5. Geocronologia U-Pb. I. Dantas, Elton Luiz, orient. II. Nunes Peixoto, Eliza Inez , co orient. III. Título.

ARTHUR SANTOS DA SILVA

METAMORFISMO DE *UHT* E *HP* NO DOMÍNIO BACAJÁ, CRÁTON DO AMAZONAS

Dissertação apresentada à Universidade de Brasília, como requisito parcial do Programa de Pós-Graduação em Geologia para a obtenção do título de Mestre em Geologia.
Área de concentração: Mineralogia e Petrologia

Aprovada em 07 de maio de 2021

Profº Dr. Renato de Moraes – USP (titular externo)

Profaº Dra. Maria Emília S. Della Giustina (titular interno)

Profº Dr. Elton Luiz Dantas

Orientador

Profº Dra. Eliza Inez Nunes Peixoto

Co-orientadora

BRASÍLIA-DF

2021

A todos que sofrem por serem apenas quem são

AGRADECIMENTOS

O autor expressa seus mais sinceros agradecimentos a todos que contribuíram para o desenvolvimento dessa dissertação, especialmente a:

Aos meus pais pelo apoio incondicional em minha decisão de deixar o Pará para cursar o mestrado em Brasília. A todos da minha família de Brasília que me acolheram da melhor maneira possível!

Ao Ronaldo por todo companheirismo e amor nessa longa jornada quem estamos trilhando juntos.

Aos laços que criei em Brasília especialmente minha amizade com Gabriela, Juliana e Nazaré e os demais colegas da pós-graduação.

A Juliana Rezende por todas as conversas e discussões super importantes sobre granulitos.

Aos professores, alunos e técnicos da Unifesspa, por trabalhos anteriores desenvolvidos na área de estudo, pela proposição da ideia inicial desse trabalho e pelo auxílio no trabalho de campo, especialmente a Filipe A. Oliveira, e ao Ari pela disponibilidade do uso dos laboratórios.

Agradecimento especial a Gilmara, minha orientadora durante a graduação e agora colaboradora durante o mestrado, que sempre me ajudou e socorreu nos momentos de necessidade.

Ao Elton e Eliza pela orientação e colaboração durante esses dois anos. Por todo o aprendizado repassado sobre esse vasto mundo geológico!

Aos professores do IG que tive contato ao longo de disciplinas e monitorias, obrigado pelos conhecimentos repassados.

A minha psicóloga Gicélia por me acompanhar desde 2018 e conseguir com que eu leve a vida de uma maneira mais leve.

Aos técnicos do laboratório de laminação, microssonda e geocronologia da UnB pelo auxílio e suporte durante a preparação e análise das amostras. A técnica Gisele Marques do laboratório de Microanálises da UFPA pela preparação de amostras e a Gilmara pela aquisição das imagens no MEV.

O presente trabalho foi realizado com apoio da Coordenação de Aperfeiçoamento de Pessoal de Nível Superior -Brasil (CAPES) - Código de Financiamento 001.

Ao INCT Estudos Tectônicos (CNPq, FAPDF, CAPES) pelo suporte às atividades de pesquisa.

“*I’m also a we and we march with pride*”
Nomi Marks

RESUMO

Na porção sul do Domínio Bacajá, sudeste do Cráton Amazônico, afloram rochas de alto grau metamórfico divididas em: cinturão granulítico Novolândia e Complexo Cajazeiras. O cinturão Novolândia é composto por rochas para- e ortoderivadas metamorfisadas em fácies granulito que são variavelmente migmatíticas. Dois resíduos distintos de migmatitos aluminosos registram metamorfismo horário, atingindo condições de ultra alta temperatura com a assembleia $Grt_{(manto)}$ ± Opx ± Sil ± Rt + L (Kfs + Pl + Qz + Ilm) e condições P-T entre ~8-9 kbar/1050-1060 ºC e 7.7–8.8 kbar/970-995 ºC seguida por descompressão-resfriamento com $Grt_{(borda)}$ + Crd ± Opx ± Sil + L (Kfs + Pl + Qz + Ilm) em 6.5-7 kbar/875-925 ºC e 6-6.5 kbar/840-850 ºC posteriormente resfriamento isobárico com $Grt_{(borda)}$ + Bt + Crd ± Sil (Kfs + Pl + Qz + Ilm) e 6-7 kbar/700-800 ºC e 4-7.5 kbar/650-730 ºC. As rochas paraderivadas possuem fontes detríticas arqueanas (3,3-2,6 Ga); os protólitos dos granulitos félsicos tem idade mínima de cristalização em ~2.76 Ga. Os protólitos dos granulitos máficos e anfibolitos foram cristalizados em 2,08 Ga e 2,03 Ga, respectivamente. Idades de metamorfismo variam entre ~2,07-2,09 Ga, interpretadas como idades de resfriamento em direção ao *solidus*, e uma idade mais nova de ~1,92 Ga. Esse cinturão foi provavelmente representa um orógeno quente de longa duração, o que desencadeou as temperaturas elevadas, as quais também podem ter sido porporcionadas devido ao extenso magmatismo juvenil coevo ao metamorfismo. Uma faixa E-W ocorrem rochas supracrustais que provavelmente representam uma grande zona de cisalhamento transcorrente que divide o Cinturão Novolândia do Complexo Cajazeiras. O Complexo é composto por rochas ígneas e metamórficas. As rochas metamórficas ocorrem como lentes restritas entre as rochas ígneas e foram metamorfisadas em fácies granulito. Elas são divididas em dois grupos: os de granulitos baixa pressão, com silimanita; e os de alta pressão com cianita. Os alta pressão experimentaram um metamorfismo horário com condições pré-pico com a assembleia $Grt_{(núcleo)}$ + Bt ± Ky ± Ms + Qz +Kfs + Rt + L em condições ~10-11 kbar/780-800 ºC, seguida por aumento progressivo de P-T atingindo condições de alta pressão com $Grt_{(manto)}$ + Bt + Ky +Rt + Kfs + Qz + Rt + Gr + L, seguida por descompressão-aquecimento atingindo condições de alta temperatura com $Grt_{(borda)}$ + Sill + Crd + Spl + Kfs + Qz + Ilm + Gr + L em 4.4–5.3 kbar/895–915 °C e finalizando com resfriamento isobárico com $Grt_{(rim)}$ + Bt + Sill + Crd + Kfs + Pl + Qz + Ilm + Gr + L em >3-5 kbar/700-798°C. Essas rochas foram formadas em um ambiente orogênico quente em processos de subducção-colisão.

PALAVRAS-CHAVE: PALEOPROTEROZOICO, GRANULITO, METAMORFISMO, GEOCRONOLOGIA U-Pb, PSEUDOSEÇÃO, CRÁTON AMAZÔNICO

ABSTRACT

The Novolândia granulite belt, south Bacajá domain, Amazonian Craton, is composed of para- and orthoderived rocks metamorphosed under granulite to amphibolite facies that are variably migmatic. Two distinct aluminous granulitic residue registers metamorphism with a clockwise P-T path reaching UHT conditions with the assemblage $Grt_{(manto)}$ ± Opx ± Sil ± Rt + L (+ Kfs + Pl + Qz + Ilm) and P-T conditions of ~8-9 kbar/1050-1060 ºC and 7.7–8.8 kbar/970-995 ºC followed by decompression-cooling $Grt_{(borda)}$ + Crd ± Opx ± Sil + L (+ Kfs Pl + Qz + Ilm) at 6.5-7 kbar/875-925 ºC e 6-6.5 kbar/840-850 ºC and later near-isobaric cooling with $Grt_{(borda)}$ + Bt + Crd ± Sil (Pl + Kfs + Qz + Ilm) with 6-7 kbar/700-800 ºC and 4-7.5 kbar/650-730 ºC. Aluminous granulites have Archean detrital sources (3.3-2.6 Ga), felsic granulites protoliths have a minimum crystallization age of ~2.74 Ga. Mafic granulites and amphibolites protoliths were crystallized at 2.08 Ga and 2.03 Ga, respectively. All lithologies show metamorphic ages ranging between 2.1 Ga and 2.07 Ga, interpreted as cooling ages to the solidus, and an outlier of 1.92 Ga. This belt was probably developed in a long-lived hot orogen, which was the main cause of the UHT metamorphism, which was also probably enhanced by extensive juvenile granitoid and local mafic magmatism. Low-grade supracrustal rocks in a E-W trending zone probably representing a major transcurrent shear zone dividing the Novolândia belt from the Cajazeiras complex. The Cajazeiras complex is composed of igneous and metamorphic rocks. The Metamorphic ones occur as restrited lenses amog igneous rocks and were metamorphosed under granulite facies. They were divided into two groups: (i) low-medium pressure sillimanite-bearing granulites, and high-pressure (HP) kyanite-bearing granulites. The HP rocks experienced a clockwise P-T path with medium/high-pressure late pre-peak $Grt_{(core)}$ + Bt ± Ky ± Ms + Qz +Kfs + Rt + L with P-T conditions of ~10-11 kbar/780-800 ºC followed by progressive P-T increase reaching high-pressure conditions $Grt_{(mantle)}$ + Bt + Ky +Rt + Kfs + Qz + Rt + Gr + L with 10.6–14 kbar/820–850ºC, which were succeeded by decompression-heating that reached high temperature conditions $Grt_{(rim)}$ + Sill + Crd + Spl + Kfs + Qz + Ilm + Gr + L with 4.4–5.3 kbar/895–915 °C and later near-isobaric cooling $Grt_{(rim)}$ + Bt + Sill + Crd + Kfs + Pl + Qz + Ilm + Gr + L with >3-5 kbar/700-798°C. These HP granulites were probably formed in a hot orogenic setting, associated with the subduction-collision process.

KEY-WORDS: PALEOPROTEROZOIC, GRANULITE, METAMORPHISM, U-Pb DATING, PSEUDOSECTION MODELING, AMAZONIAN CRATON

SUMÁRIO

CAPÍTULO 1 – INTRODUÇÃO

LISTA DE FIGURAS

CAPÍTULO 1

CAPÍTULO 2

CAPÍTULO 3

LISTA DE TABELAS

CAPÍTULO 2

CAPÍTULO 3

CAPÍTULO 1 - INTRODUÇÃO

1 INTRODUÇÃO

1.1 APRESENTAÇÃO

A região das vilas Cruzeiro do Sul e Descoberta, interior de Marabá-PA, alvo da presente pesquisa, constitui parte da porção sul do domínio Bacajá, o qual corresponde a um segmento da província Maroní-Itacaiúnas (Tassinari e Macambira, 2004), onde afloram rochas de alto grau metamórfico agrupadas no Granulito Novolândia e Complexo Cajazeiras (Félix-Silva et al., 2016). Antes da presente dissertação, poucos estudos foram realizados no região estudada (e.x., Almeida et al., 2016; Barbosa et al., 2016;), a partir dos quais se definiram as principais relações de campo e petrográficas entre as unidades de alto grau metamórfico aflorantes. No entanto, ainda é escasso ou mesmo ausente, de forma sistemática e quantitativa, estudos termobarométricos e geocronológicos para as rochas da região. Tendo em vista a vasta ausência de dados no sul do Bacajá, a presente dissertação é proposta visando contribuir com o entendimento da evolução geológica da região.

A dissertação apresenta-se estruturada em forma de capítulos. O capítulo 1, contém informações gerais da pesquisa: apresentação do trabalho, a natureza do problema e justificativas, a localização da área de estudo, objetivos, metodologia e o contexto geológico regional.

O capítulo 2 trata do artigo intitulado: "*First report of Paleoproterozoic ultra-high temperature metamorphism in the SE Amazonian Craton, Brazil*". Este trabalho apresenta dados de geologia, petrografia, termobarometria e geocronologia do cinturão granulítico Novolândia, que registra a primeira ocorrência de granulitos Paleoproterozoicos que atingiram temperaturas ultra altas no Escudo Brasil central do Cráton Amazônico.

O Capítulo 3 é intitulado: "*The missing record of high-pressure-(ultra)high-temperature granulites in the Amazonian Craton, Brazil*". Este capítulo apresenta dados de geologia, petrografia e termobarometria das lentes de granulitos de alta pressão que ocorrem entre os granitoides e charnockitos englobados no Complexo Cajazeiras. Essas rochas representam a primeira descoberta de rochas de alta pressão no Cráton Amazônico.

O Capítulo 4 sumariza as principais conclusões obtidas a partir dos artigos e da dissertação como um todo.

1.2 NATUREZA DO PROBLEMA E JUSTIFICATIVA

A caracterização metamórfica de orógenos pré-cambrianos representa uma das mais importantes ferramentas para a compreensão de processos tectônicos atuantes no período do seu desenvolvimento (ex., Brown, 2009, 2007; Brown e Johnson, 2018; Harley, 2016; Sizova et al., 2014). A porção mais interna de diversos orógenos são marcadas por rochas que experimentaram metamorfismo de alto grau, dentre as quais destacam-se os granulitos de temperatura ultra alta e de alta pressão (e.x., Khondalite Belt, Craton do Norte da China, Jiao e Guo, 2020; Wu et al., 2017). Define-se como metamorfismo de temperatura ultra alta (*UHT)* como uma subdivisão do metamorfismo em fácies granulito com temperaturas que excedam 900 ºC e pressões entre 7-13 kbar (Harley, 1998) ou rochas que experimentaram gradientes termais excedam 75 ºC kbar $^{-1}$, ou aproximadamente 20 ºC km^{-1} (Brown, 2007; Stüwe, 2007). Por outro lado, granulitos de alta pressão (*HP*) são separados em dois grupos: (1) o tipo de temperatura alta a ultra alta, que possui mesopertita coexistindo com cianita e foi formado em condições acima de 900 ºC e 15 kbar; e (2) o tipo de temperaturas moderadas e retroeclogitos, possuem texturas simplectíticas ou poiquilíticas com intercrescimento de clinopiroxênio-plagioclásio, que foram formadas em condições de 700-850 ºC e 14 kbar (O'Brien e Rötzler, 2003).

A determinação das trajetórias *P-T* e idades dessas associações metamórficas é uma das principais ferramentas utilizadas na determinação de ambiente tectônico e evolução metamórfica de orógenos (e.g. Brown e Johnson, 2018; Liu e Wei, 2020; Tam et al., 2012). Nesse contexto, destaca-se o domínio Bacajá, que é um orógeno colisional (Macambira et al. 2009Vasquez e Rosa-Costa, 2008), que apresenta vasta gama de rochas metamorfisadas em fácies granulito (Vasquez e Rosa-Costa, 2008), cuja a caracterização metamórfica é extremamente limitada (Feio et al., 2016). O DB foi estabelecido durante o Paleoproterozoico, durante o amalgamento do supercontinente Columbia (Zhao et al., 2002), período esse, em um contexto global, que foram formados diversos cinturões que apresentam rochas de alto grau metamórfico (ex., *Khondalite Belt*, Cráton do Norte da China, Jiao e Guo, 2020; Wu et al., 2017).

O projeto do Geologia e Recursos Minerais do Estado do Pará (Vasquez e Rosa-Costa, 2008) indica que na área de estudo aflora a associação Granulítica Arqueana/Paleoproterozoica, na qual são incluídos: (i) o Complexo Cajazeiras, (ii) o Granulito Novolândia, (iii) o Ortogranulito Máfico Rio Preto; e *greenstone belts* e rochas relacionadas (iv) a Sequência de Rochas Supracrustais 1. Na literatura, a área tem sido reportada através de mapeamento geológico (Ref.), iniciação científica (Ref.) e trabalhos de conclusão de curso (Ref.), liderados principalmente por pesquisadores Universidade Federal do Sul e Sudeste do Pará. O compilado desses dados foi utilizado como base para classificação das unidades, padrões estruturais e fácies petrográficas.

A Sequência de Rochas Supracrustais 1 é representada na área pela Serra Misteriosa, com um trend regional WNW-ESE, é sustentada por quartzitos puros ou com muscovita e foliados, subordinamente ocorrem micaxistos (Vasquez e Rosa-Costa, 2008). Trabalhos anteriores sugerem que essas sequências seriam possivelmente greenstone belts correlatos ao greenstone Três Palmeiras (Cristo, 2018; Macambira et al., 2009; Vasquez, 2006). São ausentes estudos que definam de maneira precisa a origem e idade dessas sequências em todo o Bacajá.

No Granulito Novolândia trabalhos anteriores sugerem protólito Mesoarqueano e metamorfismo em ~2,06 Ga (Macambira et al., 2006). Porém, não existe um panorama geral das idades de cristalização dos protólitos dos diferentes tipos de granulitos, bem como das fontes detríticas e idades de metamorfismo, além da idade de migmatização que é expressiva na unidade. Quanto às condições de pressão e temperatura obtidas anteriormente, Feio et al. (2016) indicam alta temperatura com base em termobarometria convencional. Entretanto dados de modelamento metamórfico ainda são necessários para ratificar esses dados e estabelecer trajetórias metamórficas de Pressão-Temperatura-tempo (P-T-t), tendo em vista as temperaturas equivocadas que termômetros convencionais podem resultar devido a troca tardia de Fe-Mg em granulitos (Pattison et al., 2003).

Quanto ao Ortogranulito Máfico Rio Preto, idades de cristalização em ~2,63 Ga e metamorfismo em ~2,07 Ga foram obtidas pela CPRM (Vasquez and Rosa-Costa, 2008). Na área de Cruzeiro do Sul, trabalhos da CPRM indicam a presença dessa unidade, divergentemente de mapeamentos realizados pela Unifesspa na escala de 1:50.000. Por outro lado, foram descritas variedades de enclaves anfibolíticos/granulíticos máficos hospedados nas outras unidades que poderiam ser relacionados ao OMRP. A ausência de dados geocronológicos até o momento impossibilitou melhor definição.

Por fim, o Complexo Cajazeiras apresenta grande diversidade de rochas ígneas e metamórficas. Idades obtidas anteriormente a esse estudo indicam idades de cristalização entre 2,9 Ga e 3,0 Ga para os ortognaisses do Complexo Cajazeiras e metamorfismo em 2,06 Ga (Macambira et al., 2006; Vasquez e Rosa-Costa, 2008). Para as rochas metamórficas paraderivadas, as fontes detríticas variam de Paleoproterozoicas a Mesoarqueanas (Macambira et al., 2006). Mesmo assim, o enquadramento estratigráfico ainda é incerto da região de

Cruzeiro do Sul, tendo em vista que as idades obtidas anteriormente foram realizadas em outras localidades do domínio Bacajá e podem estar associadas a outras unidades de idades distintas as da região desse trabalho. As condições de P-T-t nunca foram estudadas neste complexo. Dentre as questões abertas sobre o domínio Bacajá, destacam-se:

- ✓ Existem rochas de *UHT* e *HP*?
- ✓ Quais são suas trajetórias *P-T-t*?
- ✓ Quais são as idades de seu protólitos? Qual a idade do metamorfismo de *UHT* e *HP*?
- ✓ Como esses dois metamorfismos se relacionam entre si de maneira temporal e espacial?
- ✓ Em que contexto tectônico foram formadas essas rochas?

Assim, as informações a serem obtidas acerca das idades diferentes associações, bem como as condições e trajetórias *P-T*, deverão permitir um avanço considerável na compreensão dos processos de formação, evolução e estabilização da crosta Arqueana/Paleoproterozoica da área de Cruzeiro do Sul-Descoberta.

1.3 LOCALIZAÇÃO E ACESSO

A área de estudo possui cerca de 1050 km² e está localizada no sudeste do Pará, entre os municípios de Marabá, São Felix do Xingu, Novo Repartimento e Itupiranga, as principais sedes são as vilas Cruzeiro do Sul e Descoberta. Está situada entre as folhas topográficas Rio Bernadinho (SB.22-X-C-I) e Rio Cajazeiras (SB.22-X-C-II).

O acesso à área referida é realizado a partir do município de Marabá por via terrestre (Fig. 1.1) seguindo pela Rodovia Transamazônica (BR-230) em direção ao município de Itupiranga até o quilometro oito da BR-230. Então, vira-se à esquerda e segue-se por cerca 180 quilômetros em vicinais não pavimentadas com tráfego periódico até a vila Cruzeiro do Sul. A partir desta, o acesso aos afloramentos é feito por vicinais não pavimentadas.

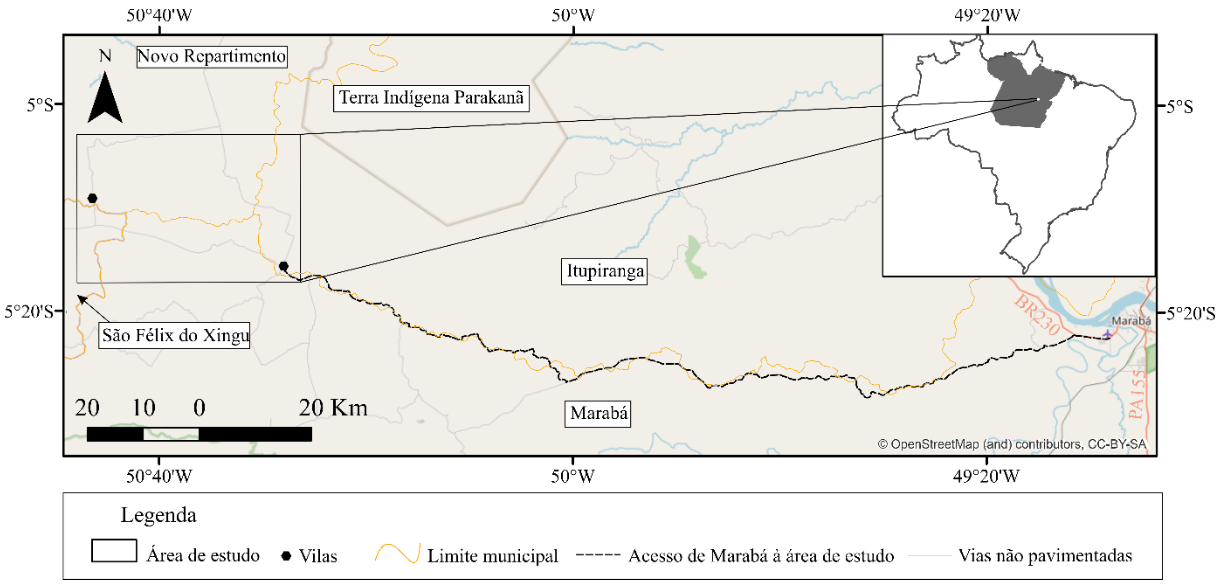

Figura 1.1 Mapa de acesso à região de Cruzeiro do Sul a partir de Marabá

1.4 OBJETIVOS

As discussões e questões levantadas na seção 1.2 foram a base para definir os objetivos do presente trabalho.

O objetivo geral é caracterizar as rochas de alto grau metamórfico da área de Cruzeiro do Sul, definir suas idades e as trajetórias de Pressão-Temperatura-tempo. Pretende-se com base nesses dados atrelados a conceitos modernos de evolução de orógenos Arqueanos/Paleoproterozoicos, elaborar um modelo de evolução crustal deste segmento do domínio Bacajá e avaliar, por extensão, as implicações desse modelo na evolução Arqueana/Paleoproterozoica da porção sul do Domínio Bacajá. Para atingir o objetivo geral, foram determinados os seguintes objetivos específicos:

1) Integrar e aperfeiçoar dos mapas geológicos produzidos anteriormente na área;
2) Caracterizar petrograficamente os diferentes tipos de rochas, com a determinação de paragêneses e reações metamórficas;
3) Determinar as idades de cristalização dos protólitos ígneos, fonte detríticas e de metamorfismo;
4) Determinar as trajetórias *P-T* e suas implicações geodinâmicas;
5) Discutir modelos tectônicos e definição da evolução Arqueana/Paleoproterozoica de Cruzeiro do Sul-Descoberta e comparar com a evolução com outros terrenos granulíticos do Cráton Amazônico e de outros Crátons do mundo.

1.5 MATERIAIS E MÉTODOS

1.5.1 Pesquisa Bibliográfica

Foi realizado levantamento bibliográfico referente à geologia do domínio Bacajá, principalmente no que concerne a processos metamórficos, com ênfase em geocronologia e termobarometria. Adicionalmente, foram consultados artigos que versam sobre geocronologia e metamorfismo de rochas granulíticas paraderivadas e qual a relação delas com processos geotectônicos globais.

1.5.2 Trabalho de Campo e Mapa Geológico Integrado

Aproveitaram-se todos os dados adquiridos durante o mapeamento geológico realizando em duas campanhas entre 2013 e 2014 por professores e estudantes de geologia da Universidade Sul e Sudeste do Pará (Unifesspa). Adicionalmente, foi feito uma campanha de campo com a participação do autor para coleta de amostras para estudos geocronológicos e geoquímicos em julho de 2019, com a participação de colaboradores da Unifesspa.

O mapa geológico foi construído com base em mapas anteriores resultantes de mapeamentos e de trabalhos de conclusão de curso combinados com imagens de satélite, radar e cartas aerorradiométricas (canais do potássio, tório, urânio e contagem total) que serviram de apoio para individualizar os domínios das diferentes unidades geológicas. As informações de campo foram confrontadas com as obtidas na petrografia e geocronologia, de modo a refinar as interpretações preliminares. Os mapas foram elaborados utilizando os softwares *ArcGis 10.3* e CorelDraw X8.

1.5.3 Petrografia

O estudo petrográfico foi iniciado com a descrição mesoscópica de todas as amostras coletadas no campo, representativas dos diferentes tipos de rochas ocorrentes na área de Cruzeiro do Sul-Descoberta. A descrição mesoscópica envolveu os principais aspectos das rochas visíveis a olho nu, tais como cor, forma, textura e estrutura. Esta etapa foi realizada com o intuito de selecionar amostras representativas dos diferentes grupos de rochas para estudos microscópicos.

Foram confeccionadas cerca de 20 lâminas delgadas e polidas para descrição microscópica. Foi utilizado o microscópio óptico de luz polarizada modelo Zeiss Axio Imager.A2M do Laboratório de Microscopia de Pós-Graduação (M-Pós) da UnB. Utilizou-se a nomenclatura e definição de granulito sugerida pela *Subcommission on the Systematics of*

Metamorphic Rocks (SSMR). A abreviação dos nomes de minerais seguiu o modelo proposto por Whitney e Evans (2010).

1.5.4 Geoquímica de Rocha Total

As análises químicas em rocha foram realizadas no laboratório comercial ALS para determinar elementos maiores (SiO_2, Al_2O_3, Fe_2O3t, MgO, CaO, Na_2O, TiO_2, Cr_2O_3, P_2O_5, PF) via Fluorescência de Raio-X (para mais detalhes ver alsglobal.com).

1.5.5 Química Mineral

Foram selecionadas lâminas representativas de cada unidade para estudo de química mineral. A análise da composição química dos minerais foi realizada no Laboratório de Microssonda (LABSON) da UnB utilizando aparelho modelo JEOL JXA-8230, condições analíticas de voltagem de aceleração 15 kV e corrente do feixe 10nA em pontos de diâmetro de 5 μm para feldspatos 1 μm para os demais minerais durante 10 segundos no pico e secundários. Os efeitos de matriz foram corrigidos pelo método ZAF. Os padrões usados foram minerais naturais: andradita (SiO_2 e CaO), albita (Na_2O), forsterita (MgO), topázio (F), coríndon (Al_2O_3), microclínio (K_2O), vanadinita (Cl e V_2O_3), pirofanita (TiO_2 e MnO) e hematita (Fe_2O_3). A redução dos dados foi feita utilizando o pacote de *software* da microssonda eletrônica.

1.5.6 Modelamento Metamórfico

O modelamento metamórfico foi feito pelo programa Theriak-Domino (De Capitani and Petrakakis, 2010) utilizando a base de dados internamente consistentes de Powell and Holland (1998). Esse método é descrito em detalhe nos capítulos 2 e 3.

1.5.7 Geocronologia U-Pb em Zircão

Os concentrados de zircão foram extraídos a partir de cerca de 10 kg de amostra, que foram trituradas, moídas, os minerais pesados foram separados com auxílio de bateia e posteriormente passados no separador magnético isodinâminco Frantz, tipo barreira magnética. Os minerais foram separados manualmente em lupa binocular.

As análises U-Pb por LA-MC-ICP-MS (*laser ablation multi-collector inductively coupled plasma mass spectrometry*) foram realizadas usando o equipamento Thermo Finnigan Neptune multi-colletor no Laboratório de Estudos Geodinâmicos Geocronológico e Ambientais (LEGGA) da UnB. O método U-Pb LA-MC-ICP-MS em zircão consiste inicialmente na confecção de montagens dos grãos de zircão em epoxy. Após a secagem do epoxy, é feito o polimento da montagem com lixa e pasta de diamante (3 μm) até que o mineral fique exposto e a superfície esteja límpida. Esse procedimento é seguido pela obtenção de imagens por elétrons retroespalhados (BSE) no microscópio eletrônico de varredura (MEV), realizada no LEGGA utilizando o MEV modelo QUANTA 450 – FEI. Após essa etapa, as montagens são banhadas em ultrassom com 3% HNO3 e após lavadas com água destilada. A montagem é colocada junto com os padrões no equipamento e os grãos de zircão analisados conforme rotina do laboratório (Bühn et al., 2009). O método U-Pb por LA-MC-ICP-MS se baseia em análises por espectrômetro de massa multi-coletor com ionização por plasma acoplada e ablação a laser e utiliza feixe de laser de diâmetro de ~25 micrômetros para ionização da superfície de amostra. Padrões são analisados em paralelo para controle e a precisão analítica fica entre 1,9 e 3,7% (2σ desvio padrão) com uma exatidão de 0,6 a 3,8% (2σ de desvio padrão). A interferência de chumbo comum (204Pb) foi corrigida pelo monitoramento das massas de ^{202}Hg e ^{204}Pb (^{204}Hg+^{204}Pb) durante as análises. O padrão primário é o GJ-1 e secundário 19950 para zircão. A redução dos dados foi feita com os *softwares* Iolite v4.0 (Paton et al., 2011) e VisualAge (Petrus and Kamber, 2012). Os diagramas de concordia, probabilidade relativa, histogramas e *weighted average* foram construídos com o Ispolot/Ex (Ludwig, 2003).

1.6 CONTEXTO GEOLÓGICO REGIONAL

Os primeiros estudos no domínio Bacajá sugiram em meados da década de 80, a partir de dados de Rb-Sr e K-Ar, Cordani et al., (1984) observaram que as rochas ao norte da serra dos Carajás, entre os rios Bacajá e Itacaiúnas, se diferenciavam das rochas Arqueanas a sul por terem sido afetadas pelo, então chamado Ciclo Transamazônico na definição de Almeida et al., (1981). Posteriormente, dados de Rb-Sr obtidos em rochas da região entre os rio Xingu e Iriri sugeriram que além de retrabalhamento de crosta Arqueana, houve também formação de crosta durante o Transamazônico (Santos et al., 1988). Posteriormente, Ricci et al., (2003) observaram contrastes litológicos, metamórficos, estruturais e geofísicos entre os domínios Bacajá e Carajás. Destaca-se o predomínio de rochas de alto grau no domínio Bacajá, uma menor proporção de rochas supracrustais e uma notável tectônica transcorrente, marcada por extensas zonas de cisalhamento NW-SE e WNW-ESE, paralelas e contínuas.

O Domínio Bacajá (Fig. 1.2) está localizado na porção oriental do Cráton Amazônico, no contexto geológico da Província Maroní-Itacaiúnas (Tassinari e Macambira, 2004). O Domínio Bacajá é recoberto por rochas sedimentares Fanerozoicas da Bacia do Amazonas e Sub-Bacia de Cametá a norte. A sul o limite proposto do domínio Bacajá com o domínio Carajás é marcado por zonas de cisalhamento E-W do Lineamento Cinzento. A oeste, as rochas vulcânicas e os granitos do Domínio Iriri-Xingu recobrem e cortam as rochas do Domínio Bacajá. No entanto, a presença de janelas de embasamento no Domínio Iriri-Xingu, e a continuidade para oeste da assinatura aeromagnetométrica do domínio Bacajá, sugerem sua extensão neste sentido. A leste os cavalgamentos do Cinturão Araguaia marcam o limite tectônico entre os domínios adjacentes (Vasquez e Rosa-Costa, 2008).

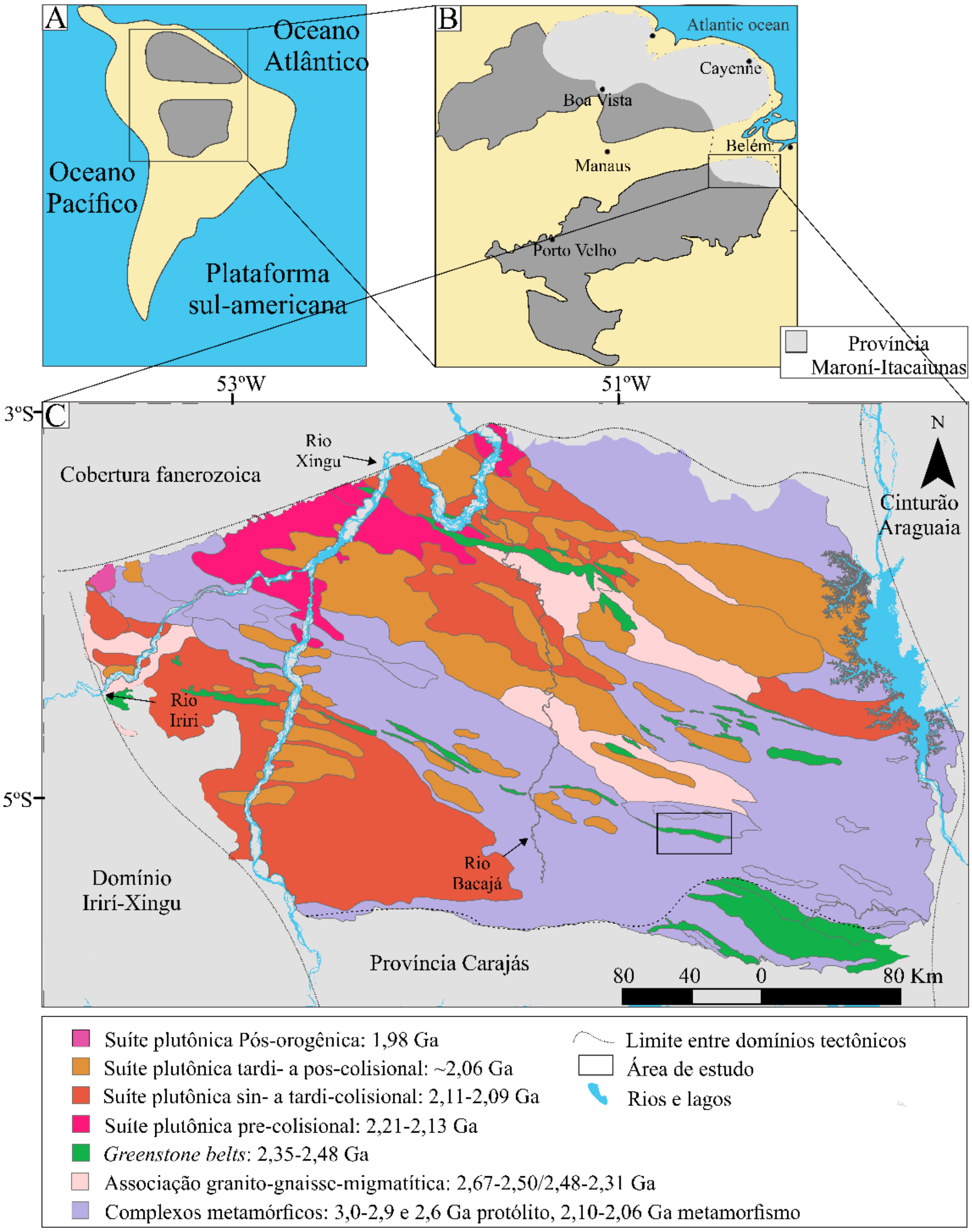

Figura 1.2 (A) localização do Cráton Amazônico na plataforma sulAmericana, (B) localização da Província Maroní-Itacaiúnas (Tassinari e Macambira, 2004), (C) Mapa regional do Domínio Bacajá (Vasques e Rosa-Costa, 2008).

No projeto do mapa geológico e recursos naturais do estado do Pará (Vasquez e Rosa-Costa, 2008 e referências contidas nele) as unidades e complexos que compõe o domínio Bacajá foram agrupados em diferentes associações tectônicas que serão apresentadas a seguir:

1. Rochas gabroicas toleíticas Mesozoicas: enxames de diques máficos de orientação NE-SW e N-S ocorrem na porção oriental do domínio Bacajá. São corpos de diabásio, provavelmente relacionados ao magmatismo toleítico jurássico (diabásios Penatecaua e Cururu) ocorrido durante a reativação Mesozoica da Bacia do Amazonas.
2. Suítes plutônicas pós-colisionais: o granodiorito Sant'Ana (~1,9 Ga), cristalizou cerca de 80 Ma após outros granitoides englobados no magmatismo tardi a pós-colisional.
3. Suítes plutônicas tardi- a pós-colisionais: compreende aos granitoides cristalizados após a colisão continental em 2,1 Ga, representados pelas suítes intrusivas Arapari (~2,08 Ga) e São Jorge (~2,06 Ga), compostas por charnockitos e granitos fortemente controlados pelas zonas de cisalhamento transcorrente de direção NWSE e WNW-ESE.
4. Suítes plutônicas sin- a tardi-colisionais: essa associação reúne os charnockitos do Complexo Bacajaí, o Granodiorito Babaquara e Granito Canaã, os quais, embora não apresentem uma composição típica dos granitoides sin-colisionais, suas idades de formação em torno de 2,1 Ga coincidem com as idades relacionadas ao clímax da colisão continental.
5. Suítes plutônicas pré-colisionais: representadas pelo Tonalito Brasil Novo, os granodioritos Oca e Belo Monte, o Monzogranito Piranhaquara e o Metatonalito Tapiranga. Segundo Vasquez (2006), essas unidades têm evolução relacionada a arcos magmáticos Riacianos instalados nas bordas de um continente consolidado no Sideriano.
6. *Greenstone belts* Arqueano/Paleoproterozoicos: agrupam as sequências metavulcano-sedimentares, destaca-se a Sequência Três Palmeiras (2,35 Ga), com rochas metamáficas, com características geoquímicas transicionais entre toleitos de arco de ilha e de fundo oceânico. As demais sequências metavulcano-sedimentares, o Grupo Vila União e a Sequência de Rochas Supracrustais 1, contam com pouca ou nenhuma informação, foram individualizadas com base em produtos geofísicos. A Sequência de Rochas Supracrustais 1 na região de Cruzeiro do Sul é composta por micaxistos e quartzitos variavelmente milonitizados.
7. Associação Granito/Gnáissico/Migmatítica Arqueana/Paleoproterozoica: reúne os ortognaisses Pacajá, Uruará e Metatonalito Rio Bacajá que foram metamorfisados em fácies anfibolito e possuem graus variados de migmatização. Os protólitos magmáticos destas unidades forneceram idades entre 2,6 e 2,3 Ga e uma idade de 2,1 Ga obtida no Ortognaisse Pacajá, interpretada como a idade de um evento de migmatização.

8. Associação granulítica Arqueana/Paleoproterozoica: reúnem as rochas do Metatonalito Rio Bacajá (-2,3 Ga) Granulito Novolândia (metamorfismo ~2,06 Ga), Paragnaisse Ipiaçava (fontes detríticas Mesoarqueanas a Siderianas e metamorfismo em 2,1 e 2,07 Ga, Quartzo-monzodiorito Vila Belmonte (~2,4 Ga), Ortogranulito Máfico Rio Preto (cristalização em 2,63 Ga e metamorfismo em 2,07 Ga),ortognaisses Pacajá (cristalização em ~2,6 Ga e metamorfismo em ~2,19 Ga) e Uruará(~2,5 Ga) e Complexos Aruanã (2,67 Ga) e Cajazeiras (cristalização em ~3,0 a 2,9 Ga e metamorfismo em ~2,07 Ga).

Quanto à evolução tectônica do Domínio Bacajá existem algumas vertentes. Uma mais antiga e levantada por diversos autores (e.x., Barros et al., 2007; Faraco et al., 2006; Macambira et al., 2007; Vasquez e Rosa-Costa, 2008), tem com base principalmente em estudos geocronológicos e isotópicos, bem como estruturais e geofísicos. Aqueles autores sugerem que durante a Orogenia Transamazônica ocorreu a colisão entre os blocos Carajás e Bacajá, sendo esse evento responsável por retrabalhar fragmentos de crostas Meso- a Neoarqueanas e Siderianas, que representariam o embasamento e/ou arcos magmáticos que foram amalgamados a crosta Arqueana de Carajás durante esta Orogenia. Durante os estágios colisionais também ocorreu intensa atividade magmática entre o Orisiriano e Riaciano.

Por outro lado, Motta et al., (2019) trouxeram duas novas propostas para a evolução do domínio Bacajá, com base em dados geofísicos atrelados a dados geocronológicos e isotópicos. A primeira delas afirma que a crosta Arqueana dos blocos Carajás e do sul de Bacajá formariam um único segmento crustal que teria colidido com o domínio Rio Maria no Mesoarqueano, nesse contexto a Zona de Cisalhamento Cinzento seria uma estrutura pré-existente que foi (re-)ativada durante a Orogenia Transamazônica. A segunda hipótese levantada afirma que os domínios Carajás e Bacajá compartilham uma história Arqueana até o momento não totalmente compreendida, ocorrida entre a colisão Carajás-Rio Maria e a Orogenia Transamazônica. Nessa hipótese, a crosta de Carajás seria formada pela justaposição entres os proto-domínios Carajás e Bacajá e o processo de cratonização ocorreria ao longo da Zona de Cisalhamento Cinzento em algum momento antes da Orogenia Transamazônica. Motta et al (2019) especulam que a separação entre Carajás e o proto-Bacajá poderia ter ocorrido devido a formação do rifte intracontinental durante o Neoarqueano (~2,75 Ga)

Os dados geocronológicos ratificam que grande parte do Domínio Bacajá, principalmente a porção a norte/nordeste e oeste/sudoeste, tiveram sua evolução relacionada a Orogenia Transamazônica com rochas com idade de cristalização que variam entre 2,3 a 2,07 Ga (ex., Barros et al., 2007; Vasquez et al., 2008), de modo mais restrito, a porção sul/sudeste, que carece ainda mais de estudos, registra a presença de crosta Arqueana cristalizada em 3,0~2,9 Ga, 2,6 Ga e 2,5 Ga (Macambira et al., 2009, 2006; Vasquez e Rosa-Costa, 2008) e retrabalhada/metamorfisada no Paleoproterozoico ~2,06 Ga (Macambira et al., 2006).

As idades de metamorfismo em obtidas a oeste do Domínio Bacajá fornecem idades de 2,1 Ga que foram relacionadas ao metamorfismo de alto grau durante o pico da colisão, em contrapartida, as idades ~2,07 Ga estão relacionadas ao metamorfismo granulítico de baixa pressão devido ao relaxamento e extensão crustal pós-colisional (Vasquez, 2006). Por outro lado, na porção sudeste foi encontrada idade de metamorfismo mais antiga ~2,19 registrada a partir de zircões de ortognaisses, além de idades entre 2,09 Ga e 2,06 Ga, que são semelhantes às da porção oeste (Macambira et al., 2006).

REFERÊNCIAS

Almeida, F.F.M., Hasui, Y., De Brito Neves, B.B., Fuck, R.A., 1981. Brazilian structural provinces: an introduction. Earth-Science Rev. 17, 1–29.

Almeida, J.A.C., Feio, G.R.L., Félix-Silva, A.D., Junior, M.F., 2016. Caracterização Geológica Do Complexo Cajazeiras , Vila Cruzeiro do Sil, Domínio Bacajá, Cráton Amazônico, in: 48º Congresso Brasileiro de Geolgia. Sociedade Brasileira de Geologia, Porto Alegre.

Barbosa, C.H.T., Almeida, J.A.C., Feio, G.R.L., 2016. Petrografia das rochas do Complexo Cajazeiras, vila Cruzeiro do Sul, Domínio Bacajá, Cráton Amazônico, in: 48º Congresso Brasileiro de Geolgia. Sociedade Brasileira de Geologia, Porto Alegre.

Barros, C.E. de M., Macambira, M.J.B., Santos, M.C. da C., Silva, D.C.C., Palmeira, L.C.M., Sousa, M.M., 2007. Estruturas sinmagmáticas e idade de zircão de granitos (evaporação de Pb) paleoproterozóicos da parte leste do domínio Bacajá, Província Maroni-Itacaiúnas. Rev. Bras. Geociências 37, 293–304. https://doi.org/10.25249/0375-7536.2007373293304

Brown, M., 2009. Metamorphic patterns in orogenic systems and the geological record. Geol. Soc. Spec. Publ. 318, 37–74. https://doi.org/10.1144/SP318.2

Brown, M., 2007. Metamorphic conditions in orogenic belts: A record of secular change. Int. Geol. Rev. 49, 193–234. https://doi.org/10.2747/0020-6814.49.3.193

Brown, M., Johnson, T., 2018. Secular change in metamorphism and the onset of global plate tectonics. Am. Mineral. 103, 181–196. https://doi.org/10.2138/am-2018-6166

Bühn, B., Pimentel, M.M., Matteini, M., Dantas, E.L., 2009. High spatial resolution analysis of Pb and U isotopes for geochronology by laser ablation multi-collector inductively coupled plasma mass spectrometry (LA-MC-ICP-MS). An. Acad. Bras. Cienc. 81, 99–114.

https://doi.org/10.1590/s0001-37652009000100011

Cordani, U., Tassinari, C.C.G., Kawashita, K., 1984. A Serra dos Carajás como região limitrofe entre províncias tectônicas. Ciências da Terra 9, 6–11.

De Capitani, C., Petrakakis, K., 2010. The computation of equilibrium assemblage diagrams with Theriak/Domino software. Am. Mineral. 95, 1006–1016. https://doi.org/10.2138/am.2010.3354

Faraco, M.T.L., Vale, A.G., Santos, J.O.S., Luzardo, R., Ferreira, A. l., Oliveira, M.A., Marinho, P.A.C., 2006. Levantamento geológico da região ao norte da Província Carajás in: Souza, in: Souza, Valmir; Horbe, A.C. (Ed.), Contribuições a Geologia Da Amazônia. Sociedade Brasileira de Geologia, Belém, pp. 32–44.

Feio, G.R.L., Sousa, J.T., Almeida, J.A.C., 2016. Geotermobarometria de granulitos do Complexo Novolândia, porção sul do Domínio Bacajá, Província Tranzamazonas, in: 48º Congresso Brasileiro de Geolgia. Sociedade Brasileira de Geologia, Porto Alegre.

Félix-Silva, A.D., Almeida, J.A.C., Feio, G.R.L., 2016. Mapa e banco de dados geológico da vila Cruzeiro do Sul, porção sul do Domínio Bacajá, in: 48º Congresso Brasileiro de Geolgia. Sociedade Brasileira de Geologia, Porto Alegre.

Harley, S.L., 2016. A matter of time: The importance of the duration of UHT metamorphism. J. Mineral. Petrol. Sci. 111, 50–72. https://doi.org/10.2465/jmps.160128

Harley, S.L., 1998. On the occurrence and characterization of ultrahigh-temperature crustal metamorphism. Geol. Soc. Spec. Publ. 138, 81–107. https://doi.org/10.1144/GSL.SP.1996.138.01.06

Holland, T.J.B., Powell, R., 1998. An internally consistent thermodynamic data set for phases of petrological interest. J. Metamorph. Geol. 16, 309–344.

Jiao, S., Guo, J., 2020. Paleoproterozoic UHT metamorphism with isobaric cooling (IBC) followed by decompression–heating in the Khondalite Belt (North China Craton): New evidence from two sapphirine formation processes. J. Metamorph. Geol. 38, 357–378. https://doi.org/10.1111/jmg.12525

Liu, T., Wei, C., 2020. Metamorphic P–T paths and Zircon U–Pb ages of Archean ultra-high temperature paragneisses from the Qian'an gneiss dome, East Hebei terrane, North China Craton. J. Metamorph. Geol. 38, 329–356. https://doi.org/10.1111/jmg.12524

Ludwig, K.R., 2003. isoplot Excell version 3.0. A geochronological toolkit for Microsoft Excel,.

Macambira, M.J.B., Armstrong, R.A., Silva, D.C.C., Camelo, J.F., 2006. The Archean-

Paleoproterozoic boundary in Amazonian craton: New isotope evidence for crustal growth, in: Geochimica et Cosmochimica Acta. p. A380. https://doi.org/10.1016/j.gca.2006.06.768

Macambira, M.J.B., Pinheiro, V.L., Armstrong, R.A., 2007. A fronteira Arqueano-Paleoproterozoico no SE do Cráton Amazônico: abrupta no tempo, suave na tectônica?, in: X Simpósio de Geologia Da Amazônia. pp. 97–100.

Macambira, M.J.B., Vasquez, M.L., Silva, D.C.C., Galarza, M.A., Barros, C.E.M., Camelo, J.F., 2009. Crustal growth of the central-eastern Paleoproterozoic domain, SW Amazonian craton: Juvenile accretion vs. reworking. J. South Am. Earth Sci. 27, 235–246. https://doi.org/10.1016/j.jsames.2009.02.001

Motta, J.G., Souza Filho, C.R. d., Carranza, E.J.M., Braitenberg, C., 2019. Archean crust and metallogenic zones in the Amazonian Craton sensed by satellite gravity data. Sci. Rep. 9. https://doi.org/10.1038/s41598-019-39171-9

O’Brien, P.J., Rötzler, J., 2003. High-pressure granulites: Formation, recovery of peak conditions and implications for tectonics. J. Metamorph. Geol. 21, 3–20. https://doi.org/10.1046/j.1525-1314.2003.00420.x

Paton, C., Hellstrom, J., Paul, B., Woodhead, J., Hergt, J., 2011. Iolite: Freeware for the visualisation and processing of mass spectrometric data. J. Anal. At. Spectrom. 26, 2508–2518. https://doi.org/10.1039/c1ja10172b

Petrus, J.A., Kamber, B.S., 2012. VizualAge: A Novel Approach to Laser Ablation ICP-MS U-Pb Geochronology Data Reduction. Geostand. Geoanalytical Res. 36, 247–270. https://doi.org/10.1111/j.1751-908X.2012.00158.x

Ricci, P.S.F., Costa, E.J.S., Oliveira, J.., 2003. The reanalyzed Carajás block is interposed between the Bacajá (the crustal reworking “lost link” now being predicted) and Rio Maria Archean terranes – Guaporé Craton, in: VIII Simpósio de Geologia de Amazônia. Sociedade Brasileira de Geologia, Manaus.

Santos, M.V.., Souza, E.E.F., Tassinari, C.C.G., Teixeira, W., Ribeiro, A.C.O., Payolla, B.L., Vasconi, A.., 1988. Litoestratigrafia das rochas pré- cambrianas na bacia do médio Rio Xingu – Altamira-PA, in: 7 Congresso Lationo-Americano de Geologia. Sociedade Brasileira de Geologia, Belém, pp. 363–377.

Sizova, E., Gerya, T., Brown, M., 2014. Contrasting styles of Phanerozoic and Precambrian continental collision. Gondwana Res. 25, 522–545. https://doi.org/10.1016/j.gr.2012.12.011

Stüwe, K., 2007. Geodynamics of the Lithosphere: Quantitative Description of Geological Problems, Eos Trans. AGU.

Tam, P.Y., Zhao, G., Zhou, X., Sun, M., Guo, J., Li, S., Yin, C., Wu, M., He, Y., 2012. Metamorphic P-T path and implications of high-pressure pelitic granulites from the Jiaobei massif in the Jiao-Liao-Ji Belt, North China Craton. Gondwana Res. 22, 104–117. https://doi.org/10.1016/j.gr.2011.09.006

Tassinari, C.C.G., Macambira, M.J.., 2004. A evolução tectônica do Craton Amazônico, in: Mantesso-Neto, V., Bartorelli, A., Carneiro, C.D.R., Brito Neves, B.B. (Eds.), Geologia Do Continente Sul Americano: Evoluc¸ Ão Da Obra de Fernando Flávio Marques Almeida. São Paulo, pp. 471–486.

Tavares, F.M., Silva, C.M.G., 2012. Carta Geológica SB.22-X-C-VI FOLHA SERRA PELADA 1:10000, CPRM. CPRM, Pará, Brazil.

Vasquez, M.L.., Rosa-Costa, L.T.., 2008. Geologia e Recursos Minerais do Estado do Pará : Sistema de Informações Geográficas – SIG : texto explicativo dos mapas Geológico e Tectônico e de Recursos Minerais do Estado do Pará, 1st ed. Brazilian Geological Service, CPRM, Belém.

Vasquez, M.L., 2006. Geocronologia em zircão, monazita e granada e isótopos de Nd das associações litológicas da porção oeste do Domínio Bacajá: evolução crustal da porção meridional da Província Maroni-Itacaiúnas – Sudeste Do Cráton Amazônico. Universidade Federal do Pará.

Vasquez, M.L., Macambira, M.J.B., Armstrong, R.A., 2008. Zircon geochronology of granitoids from the western Bacajá domain, southeastern Amazonian craton, Brazil: Neoarchean to Orosirian evolution. Precambrian Res. 161, 279–302. https://doi.org/10.1016/j.precamres.2007.09.001

Whitney, D.L., Evans, B.W., 2010. Abbreviations for names of rock-forming minerals. Am. Mineral. 95, 185–187. https://doi.org/10.2138/am.2010.3371

Wu, J., Zhang, Huafeng, Zhai, M., Guo, J., Li, R., Wang, H., Zhao, L., Jia, X., Wang, L., Hu, B., Zhang, Haidong, 2017. Paleoproterozoic high-pressure-high-temperature pelitic granulites from Datong in the North China Craton and their geological implications: Constraints from petrology and phase equilibrium modeling. Precambrian Res. 303, 727–748. https://doi.org/10.1016/j.precamres.2017.09.011

Zhao, G., Cawood, P.A., Wilde, S.A., Sun, M., 2002. Review of global 2.1-1.8 Ga orogens: Implications for a pre-Rodinia supercontinent. Earth-Science Rev. 59, 125–162.

CAPÍTULO 2 - ARTIGO 1

FIRST REPORT OF PALEOPROTEROZOIC ULTRA-HIGH TEMPERATURE METAMORPHISM IN THE SE AMAZONIAN CRATON, BRAZIL*

ABSTRACT: UHT granulite facies represents the most thermally extreme type of metamorphism and is widely distributed worldwide, recording secular changes in the geodynamics of orogenic systems. Here we present the first report of Paleoproterozoic UHT rocks in the SE Amazonian Craton recorded in a granulite-gneiss belt, located in the Bacajá domain. The Novolândia granulite belt is composed of felsic, aluminous and mafic granulite facies rocks that are variably migmatic. We identified four mineral assemblages in the aluminous granulite residue corresponding to different metamorphic stages, which define a clockwise *P*-*T* path of the metamorphic events. The peak (M2) mineral assemblage of $Grt_{(mantle)}$+Pl+Kfs+Qz+Ilm±Opx±Sil±Rt+L with 8-9 kbar/1050-1070ºC and ~7.7–8.8 kbar/970-995ºC. The decompression-cooling (M3) is characterized by: $Grt_{(rim)}$+Crd +Pl+Kfs+Qz+Ilm±Opx±Sil+L in a range of 6-7 kbar/875-925 ºC and 6-7 kbar/700-800 ºC. The subsequent post-peak isobaric cooling stage (M4) is characterized by $Grt_{(rim)}$+Bt+Crd+Pl+Kfs+Qz+Ilm±Sil ranging from 6-6.5 kbar/840-850 ºC to 4-7.5 kbar/650-730 ºC. LA-ICP-MS U–Pb analysis of zircon grains in aluminous granulites residue provided dominantly Archean detrital sources ranging from ca. 3.3 to 2.6 Ga. In felsic granulites a minimum crystallization age of 2744±21 Ma was obtained. Mafic granulites and amphibolites

---

*Research article to be submitted

Arthur Santos da Silva [a, b, c#], Elton Luiz Dantas [a, b, d], Eliza Inez Nunes Peixoto [a], Reinhart Adolf Fuck [b], Gilmara Regina Lima Feio [c, e], José de Arimatéia Costa de Almeida [c, e], Guilherme de Oliveira Gonçalves [a, d] , Roberto Ventura Santos [a, d]

[a] Programa de Pós-graduação em Geologia, Instituto de Geociências (IG), Universidade de Brasília (UnB), Brazil

[b] Grupo de Tectônica e Fluxo de Fluídos, IG-UnB, Brasília, DF, CEP 70910-900, Brazil

[c] Grupo de Mineralogia e Petrologia, Instituto de Geociências e Engenharias (IGE), Universidade Federal do Sul e Sudeste do Pará (Unifesspa), Marabá, PA, CEP 68505080, Brazil

[d] Laboratório de Estudos Geocronológicos, Geodinâmicos e Ambientais, IG-UnB, Brasília, DF, CEP 70910-900, Brazil

[e] Laboratório Multiusuário de Microanálise em Materiais, IGE, Unifesspa, Marabá, PA

Corresponding author: santosarthursilvaa@gmail.com

were crystallized at 2082±7 Ma and 2035±14 Ma, respectively. Metamorphic cooling ages to the solidus were obtained in all the studied lithotypes, yielding the following results: 2106±5 Ma (felsic granulite) and 2076±11 Ma (aluminous granulite residue), a younger age of 1921±16 Ma (mafic granulite). We suggest that the protoliths UHT aluminous migmatites were formed in a long-lived large hot collisional orogen and UHT conditions were probably enhanced by intense orogenic magmatism and that this belt constitutes a part of several Paleoproterozoic granulite belts in the Amazonian Craton, similar to other granulite belts of the same age in Africa, India, and China and could be used as piercing point of supercontinent assembly reconstructions models.

KEY-WORDS: Pelitic granulite, ultra-high temperature, phase equilibria modeling, hot orogen, Amazonian Craton

1 INTRODUCTION

Paleoproterozoic gneiss-granulite belts record valuable information of lower continental crust, tectonic settings, and processes operating in the formation and evolution of ancient orogenic belts (e.g., Bozhko, 2018; Brown, 2007; Brown and Johnson, 2018). Specifically, the presence of high to ultra-high temperature (UHT) granulite metamorphism is worthwhile information once it provides the pressure-temperature-time (*P*-*T*-*t*) paths of the crust and hence direct insights into the behavior and evolution of the crust's deeper levels, allowing the reconstruction of the configuration of continental masses (e.g., Brown, 2009, 2007; Kelsey and Hand, 2015). Specifically, the study of this register is useful because many final events of supercontinent amalgamation correspond to episodes of (U)HT metamorphism (Touret et al., 2016), and also because it occurs in various tectonic settings, such as continental collisional and accretionary orogenic systems (Brown, 2009, 2007), as well as post-collisional extension, intracontinental rifting and mantle plume(Santosh et al., 2012).

On the other hand, the exhumation of granulites has occurred through several processes, including the overthrusting of nappes in a collisional orogen (Biswal and Sinha, 2003), and oblique shearing along multiple retrograde shear zones in a transpressional setting (Sandiford and Powell, 1986). These factors hamper unveiling the tectonic, metamorphic, and exhumation history of these high-grade rocks. Nonetheless, once unraveled, they can give a batch of unique insights into the evolution of granulite-gneiss belts.

UHT rocks record the most thermally extreme type of regional crustal metamorphism, defined by Harley (1998) as non-igneous crustal temperatures above 900ºC at a pressure of 7-

13 kbar thermal gradients that exceed 75 ºC $kbar^{-1}$, or approximately 20 ºC km^{-1} (Brown, 2007; Stüwe, 2007). In their revision, Kelsey and Hand (2015) report evidence of fifty-eight UHT localities. Between these only seven occurred during the Paleoproterozoic, in the North China Craton (e.g., Santosh et al., 2012), Lewisian Complex, Scotland (e.g., Zirkler et al., 2012), São Francisco Craton, Brazil (e.g., Leite et al., 2009), Gawler Craton, Australia (Cutts et al., 2013), Ouzzal terrane, Algeria (e.g., Ouzegane et al., 2003), Central India Tectonic Zone (Bhowmik et al., 2014), and Lapland Granulite belt, Russia (e.g., Lebedeva et al., 2010). Other two UHT occurrences are present in the Suriname, Guiana Shield of the Amazonian Craton (Roever et al., 2003; Klaver et al., 2015; Nanne et al., 2020) and in the West Africa Craton (Triboulet and Feybesse, 1998). UHT rocks developed in the Paleoproterozoic are rather restricted in Brazil, there is evidence of these rocks only in the Itabuna-Salvador-Curaça belt, São Franscico Cráton (e.g., Barbosa et al., 2017; Rodrigues et al., 2020)

UHT metamorphism has been suggested to be coeval with supercontinent assembly (e.g., Bozhko, 2018; Brown, 2007; Brown and Johnson, 2018). During the Paleoproterozoic, a worldwide set of orogenies took place to build up a supercontinent called Columbia (see Meert and Santosh, 2017, and references therein). During the assembly, several UHT granulites with similar ages were identified on a global scale (e.g., Khondalite belt, China, Jiao, and Guo, 2020), which can be used as a piercing point in supercontinent assembly reconstruction models (Touret et al., 2016).

In this paper, we have studied a set of granulite rocks in the south Bacajá domain, southeast Amazonian Craton, Brazil, known as the Novolândia granulite belt. Our study, based on field and petrographic data, along with U-Pb geochronology and pseudosection modeling, allows us to report the first ultra-high temperature (UHT) metamorphism identified in the Bacajá domain. These rocks provided a significant amount of information to clear up the evolution of this domain and its correlation to other UHT granulite terrains worldwide and within the Amazonian Craton formed during the build-up of a Paleoproterozoic supercontinent. We envisage a long-lived large hot collisional orogen for the evolution of the Bacajá domain and the heat source for UHT conditions, supported by the proposed long-lasting metamorphism, the maintenance of HT suprasolidus conditions for more than 30 million years, and the *P*-*T* path with decompression-cooling, followed by isobaric cooling is similar to typical hot orogens.

2 GEOLOGICAL SETTING

The Maroní-Itacaiúnas Province is the main province established during the Paleoproterozoic in the Amazonian Craton (Santos et al., 2006; Tassinari and Macambira,

2004) and include several granulite-gneiss belts (Fig. 2.1b) formed during the regional Transamazonian Orogeny (Almeida et al., 1981; Brito Neves, 2011; Hurley et al., 1967). They are distributed within the two compartments of the Amazonian Craton: the Guiana shield and the Central Brazil shield (Fig. 2.1b). In the Guiana shied five granulite belts were distinguished (Fig. 2.1b). Two of them are reworked Archean belts, the Amapá block (Milhomem Neto and Lafon, 2019; Rosa-Costa et al., 2003) and the Imataca Block (Tassinari et al., 2004). There are also Paleoproterozoic Belts, such as the Bakhuis (Roever et al., 2003), Caurane-Curuni (Fraga et al., 2008), and Carecuru-Paru domains (Rosa-Costa et al., 2006; Rosa-Costa et al., 2003). In the Central Brazil shield, in another hand, only one granulite-gneiss belt occurs, known a Bacajá domain (Fig. 2.1b, c), the metamorphic evolution of which is the focus of this work.

The Bacajá domain (Fig. 2.1b) is the counterpart of the Maroní-Itacaíunas Province in the Brazil Central Shield. This domain is composed of Archean and Siderian fragments reworked during the Transamazonian Orogeny between ca. 2.26 an 1.99 Ga, (Cordani et al., 2000; Hurley et al., 1967), and Rhyacian to Orosirian granitoids related to orogenic magmatism (Vasquez and Rosa-Costa, 2008; Vasquez, 2006; Vasquez et al., 2008). The Bacajá basement is represented by two lithotectonic associations: (i) Archean metamorphic complexes composed of orthogranulite and orthogneiss with Mesoarchean protoliths (3000±2 Ma and 2943±4 Ma, Macambira et al., 2007; Vasquez and Rosa-Costa, 2008), and with Neoarchean protoliths (2671±3 Ma, Vasquez and Rosa-Costa, 2008); and (ii) a late Neoarchean orthoderived granite-gneiss-migmatite association crystallized at 2503±10 Ma (Macambira et al., 2004, 2003). In the first association, occurring as small lenses or enclaves within the Archean orthoderived rocks, some restricted aluminous granulites and paragneiss occur but are still not well understood. They have detrital sources ranging from the Mesoarchean to the Paleoproterozoic (3.14-2.47 Ga, Macambira et al., 2007; Vasquez, 2006). Associated to the basement, Siderian juvenile greenstone belts and related rocks crop out, with acid volcanic rocks crystallized at 2452±3 Ma to 2359±3 Ma (Macambira et al., 2009, 2003; Vasquez, 2006)

Paleoproterozoic orogenic magmatism records several events as proposed by Vasquez and Rosa-Costa (2008) and references therein: (i) pre-collisional magmatism dated from 2215±2 Ma to 2133±10 Ma; (ii) the syn- to late-collisional magmatism dated from 2114±3 Ma to 2102±3 Ma; (iii) late- to post-collisional magmatism dated from 2086±5 Ma to 2069±6 Ma; and (iv) the post-collisional magmatism dated at 1986±5 Ma.

The metamorphic events in Bacajá are closely related to the magmatic evolution and were recorded in all exposed belts. In the eastern sector, two events were identified, based on monazite U-Pb ages, whereas an older event (2109±9 Ma) representing the collisional peak between the Carajás and Bacajá domains; the second and younger event took place at 2071±3 Ma, related to low-pressure granulitic metamorphism due to the orogenic collapse (Vasquez, 2006). In the western sector, similar ages were obtained on zircon from orthogneiss (Tavares and Silva, 2012) and an older event at ca. 2195±3 Ma (Macambira et al., 2004).

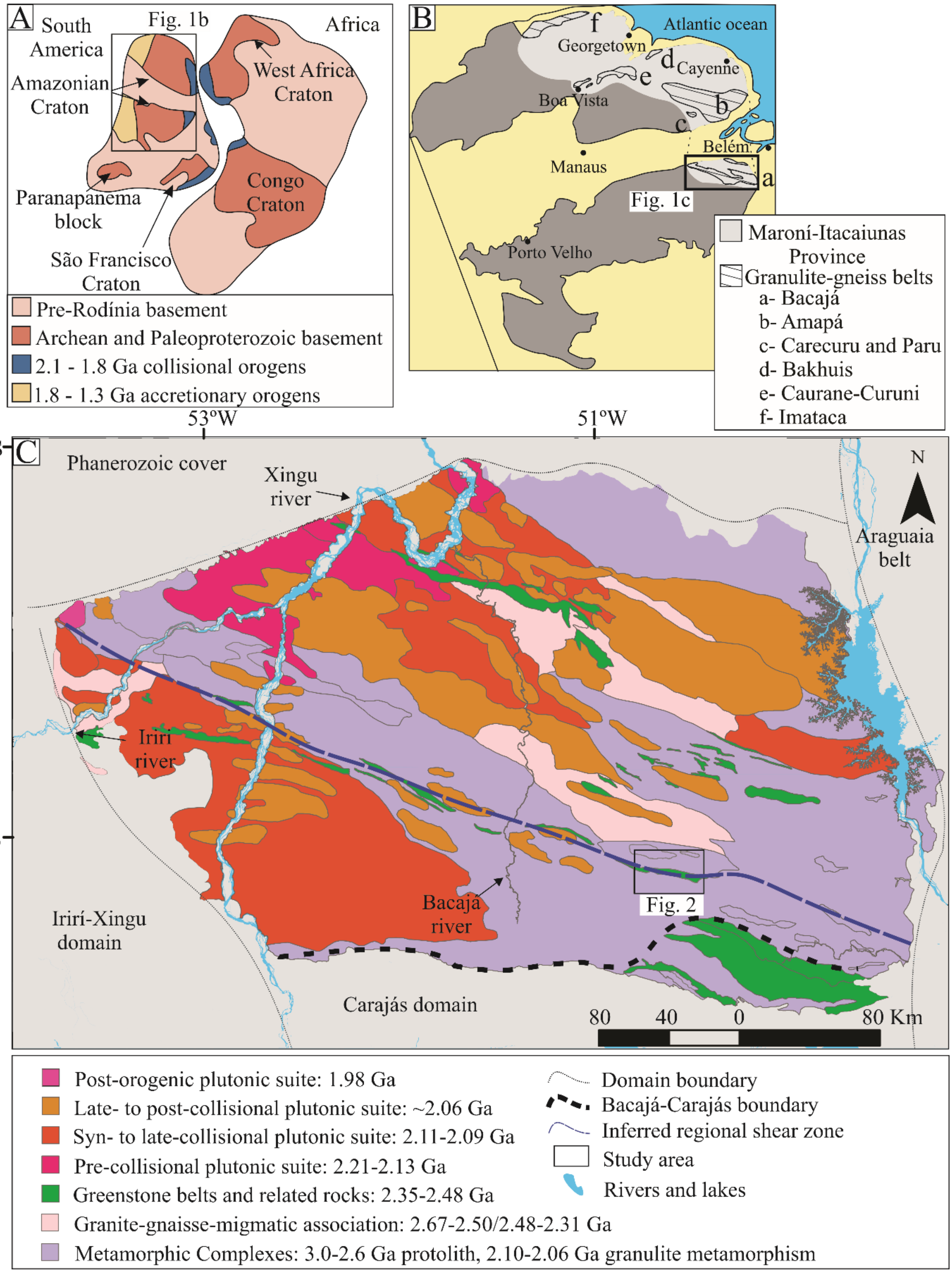

Figure 2.1(A) Location of the Amazonian-West Africa craton in the Columbia supercontinent (Zhao et al. 2002); (B) the granulite-gneiss belts in the Maroní-Itacaiúnas Province; (C) map showing the lithoteconic

compartmentation of Bacajá domain, and location of the study area (Vasquez et al. 2008 and references therein, Macambira et al. 2009).

3 ANALYTICAL METHODS

3.1 FIELD WORK

Fieldwork in the Cruzeiro do Sul-Descoberta area covered an area of 1050 Km^2 in a scale 1:100.00. The work was carried out during 2019 to investigate the structural pattern and stratigraphic relations between the distinct lithological associations that outcrop in that area. Geological mapping was supported by geochronology, geophysical, and petrographic surveys.

3.2 PETROGRAPHY AND MINERAL CHEMISTRY

Petrography was performed using the microscope Zeiss Axio Imager.A2M with transmitted and reflected light. Mineral abbreviations follow Whitney and Evans (2010).

Representative samples were selected for mineral chemistry. The analyzed minerals were garnet, orthopyroxene, cordierite, plagioclase, biotite, K-feldspar and spinel. Polished thin sections of the selected samples were submitted to wavelength dispersive spectroscopy (WDS) quantitative analyses at the Laboratório de Microssonda (LABSON) from Universidade de Brasília (UnB), using a JEOL JXA-8230 electron microprobe analyzer. Analyses were performed under the following operating conditions: a column accelerating voltage of 15 kV, a current of 10 nA, an analysis time of 10 s. The standards used for instrument calibration were andradite (Ca and Fe), microcline (Si, Al, and K), olivine (Mg), albite (Na), pyrophanite (Ti and Mn), vanadinite (V and Cl), nickel oxide (Ni), chromium trioxide (Cr), and Celestine (Sr). All thin sections selected for electron microprobe analyses were previously carbon coated. The data was treated using the software AX (Holland; http://www.esc.cam.ac.uk/astaff/holland/ax.html)

3.3 U-PB GEOCHRONOLOGY

Zircon were separated using standard rock crushing and heavy mineral separation techniques. Grains were individually selected, picked, and mounted in epoxy resin. Grain mounts were polished to expose the grain centers. Backscatter electron images for zircon were performed with a QUANTA 450 – FEI scanning electron microscope (SEM) at the Laboratório de Estudos Geodinâmicos, Geocronológicos e Ambientais (LEGGA) from UnB. The analysis follows the laboratory's standard procedures (Bühn et al., 2009). The U-Pb analysis in zircon and monazite was carried out using the Neptune Series High-Resolution Multicollector ICP-MS coupled with laser ablation system Nd-YAG 213nm NewWave. Instrument set up parameters were 3,81-3,85 and 2,67-2,70 J/cm2 laser fluence for zircon and monazite respectively, 10 Hz, ~25 μm spot size. U-Pb zircon data were standardized using GJ-1 (reference 609 Ma, Jackson et al., 2004) as a primary standard and tested using the zircon 91500 (reference 1065 Ma, Wiedenbeck et al., 1995) as a secondary standard. External errors were calculated with the error propagation of individual measurements of GJ-1 and each spot's measurements. Data reduction was made using the software Iolite v4.0 (Paton et al., 2011), and VisualAge (Petrus and Kamber, 2012), concordia diagrams, and density plots were done using Ispolot/Ex (Ludwig, 2003).

4 GEOLOGICAL AND STRUCTURAL ASPECTS

The study area is in north Brazil, southeast Pará State, near the Cruzeiro do Sul and Descoberta villages (Fig. 2.2). It is situated in the Maroní-Itacaiunas Province (Tassinari and Macambira, 2004), close to the Bacajá and Carajás domains boundary (Faraco et al., 2006).

The Novolândia granulite belt is located in the north portion of the study area. It has approximately 80 km long in the NW-SE direction and no more than 15 km wide. This belt is limited in the south by a sequence of low-grade supracrustal rocks and by Archean tonalitic gneiss in the north, that might represent a TGG series or magmatic rocks derived from an island-arc setting (2.67 Ga, Macambira et al., 2009).

The Novolândia belt in the study area (Fig. 2.2) comprise paraderived aluminous (Fig. 2.3), orthoderived felsic and mafic rocks (Fig. 2.4) metamorphosed under granulite facies with variable degrees of migmatization. The contacts between distinct lithologies are variable. Mafic granulites and amphibolites usually occur as flattened (Fig.2. 4a), sub-angular (Fig. 2.4b), or rounded (Fig. 2.4c) enclaves/schollen in felsic granulites and aluminous migmatites. Felsic granulites present abrupt contact relationships with granitic leucosome (Fig. 2.4f).

The aluminous rocks were classified according to Sawyer (2008) as stromatic metatexite, exhibiting granulite residue, leucosome and reaction selvedge. Residues are essentially composed of garnet, cordierite, orthopyroxene and feldspars, silimanite occur in some portions, but not together with orthopyroxene (Fig 2.4g, h). Leucosome layers are rich in garnet, quartz, feldspars and silimanite (Fig. 2.3a, b, c). Selvedge reaction rims are essentially composed of biotite and garnet (Fig. 2.3a).

Felsic granulites are the most abundant lithology (Fig. 2.4a, d-f). Most of them are mylonitic, with a pervasive and ubiquitous foliation characterized mainly by recrystallized and oriented quartz and feldspar crystals, locally pyroxene, and retrogressed biotite (Fig. 2.4e). Banding is marked by the alternation of mafic and leucocratic layers (Fig. 2.4f)

Mafic granulites and amphibolites are the least common rock type. They show no significant deformation (Fig. 2.4g), locally with a slight local orientation of crystals (Fig. 2.4k, l). However, when occurring as schollen in felsic granulites and aluminous migmatites, they show the same deformation orientation as host rocks, with a penetrative foliation (Fig. 2.4a, k). Amphibolite occurs only as restricted fragments/schollen in and as enclaves felsic granulites and aluminous migmatites (Fig. 2.4b, c).

On the map scale, the foliation trajectory and shear zones that affect the granulitic rocks trend mainly WNW-ESE, with anastomosing arrays. The structures present in the metamorphic rocks are well-developed foliations (Fig. 2.4e), flattened mafic enclaves (Fig. 2.4a), local banding (Fig. 2.4d), and mineral stretching lineation (Fig. 2.4j). Shear sense indicators such as porphyroblasts (Fig. 2.4k) and S-C structures (Fig. 2.4l) with sinistral shear sense are common. All features trend E-W to WNW-ESE with moderate (50º to 65º) and subvertical (70º to 85º) dips towards S and N, and sub-horizontal mineral stretching lineation (0 to 20º). In addition to these structural data, a restricted structural pattern is also identified, defined by a uniform NNW-SSE trending foliation with steep dips towards the W and E (78º to 84º), with sub-vertical mineral stretching lineation trending to E with high plunges (70º), and subordinate vertical foliation.

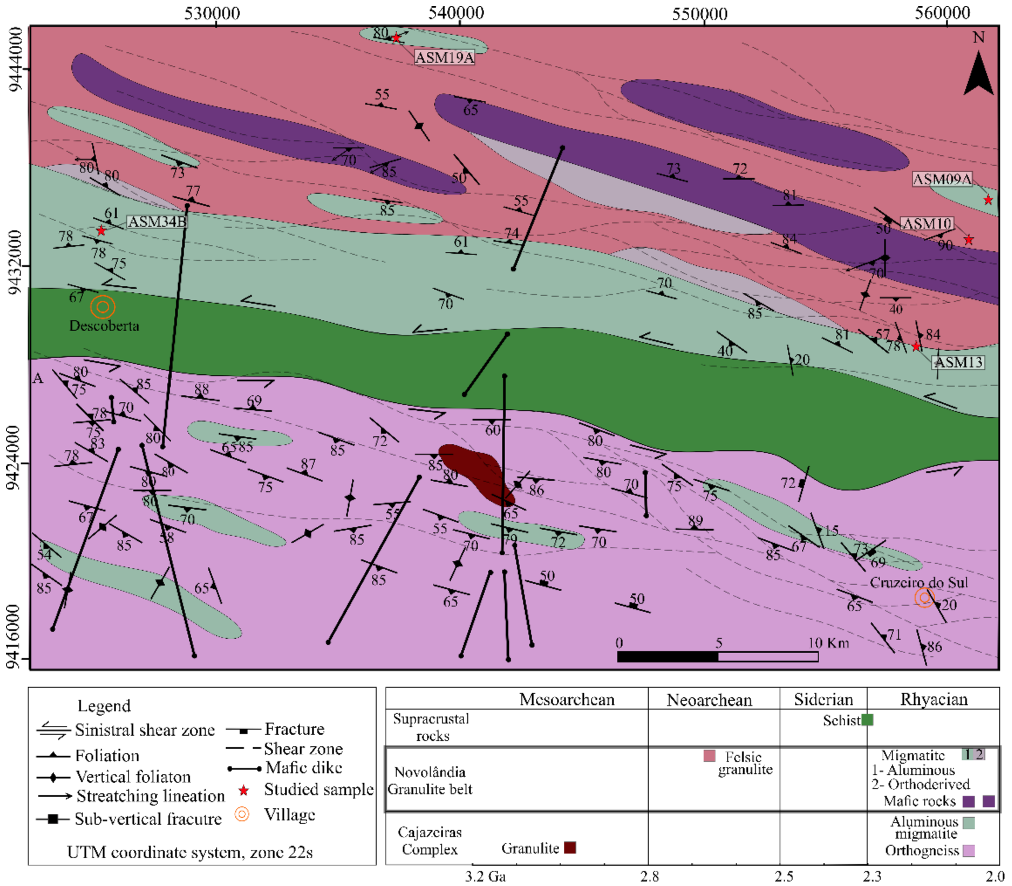

Figure 2.2 Geological map of the Cruzeiro do Sul-Descoberta area (modified from Félix-Silva, 2016). Chronostratigraphic correlations are base in field observations and geochronological obtained in this work (section 8) and data from Macambira et al. (2009) and Vasquez and Rosa-Costa (2008).

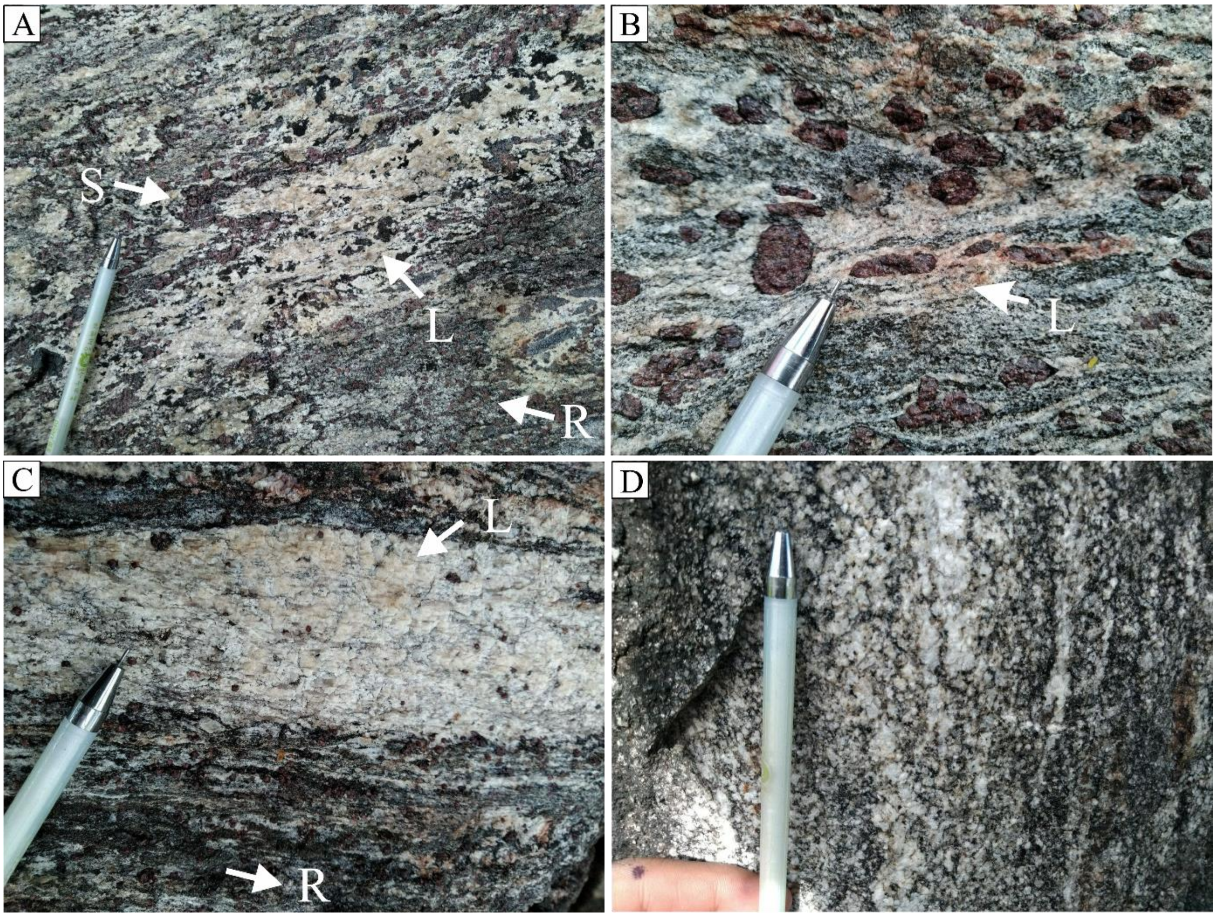

Figure 2.3 Geological and structural aspects of the aluminous rocks from the Novolândia granulite belt. (A) aluminous fold-structured metatexite with leucosome (L), biotite-garnet rich selvedge (S), and residue (R) (dated sample ASM9A); (B) aluminous metatexite with deformed peritectic garnet porphyroblasts; (C) stromatic aluminous metatexite; (D) stromatic aluminous metatexite.

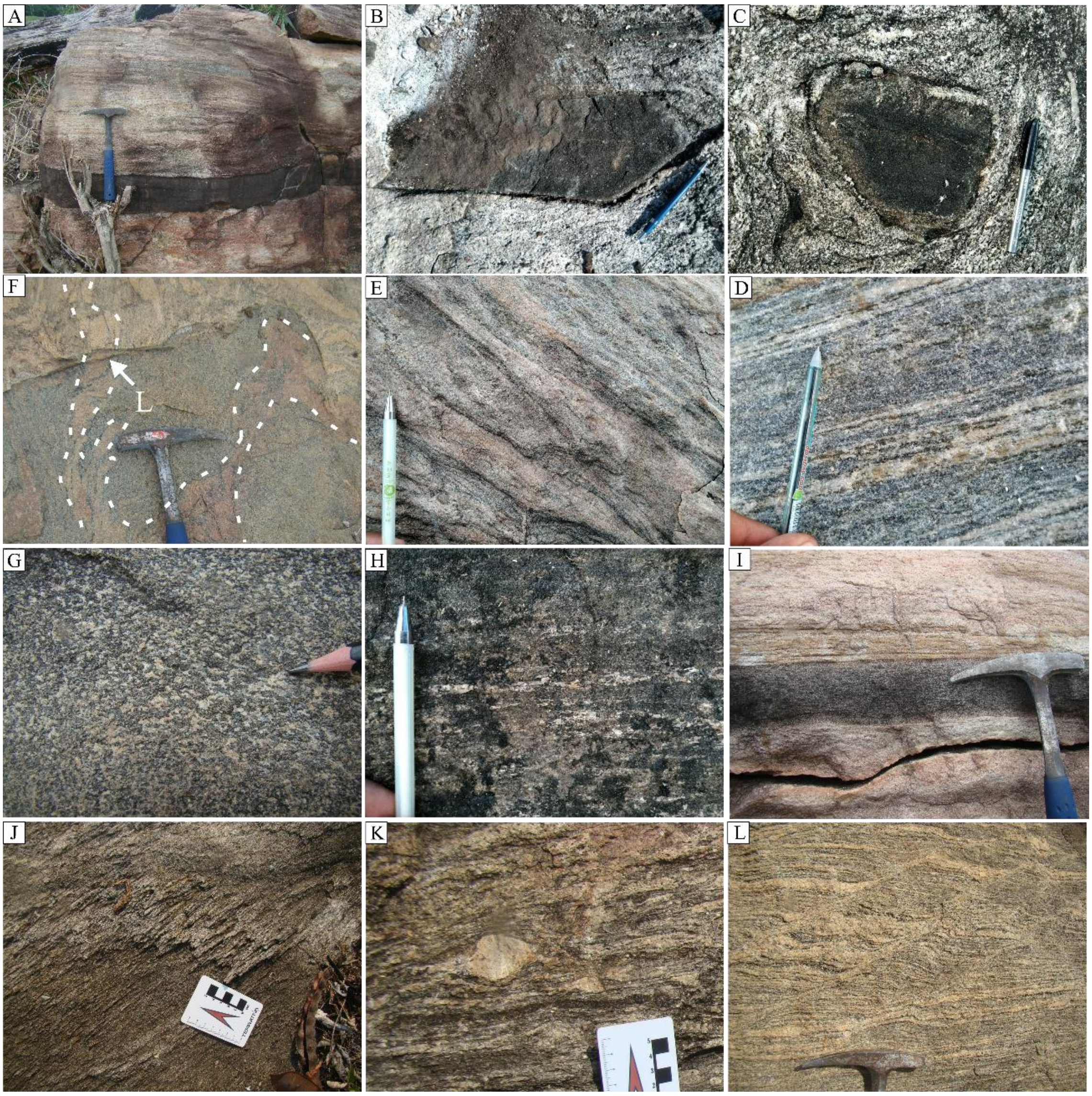

Figure 2.4 Geological and structural aspects of orthoderived rocks from the Novolândia Granulite. (A) flattened (highly deformed) mafic granulite schollen in felsic granulite; (B) sub-angular amphibolite fragment hosted in aluminous migmatite (ASM34B, dated sample) ; (C) rounded amphibolite fragment in aluminous migmatites (D) abrupt contact between felsic granulite (residue) and a granitic leucosome; (E) deformed felsic granulite showing a typical mylonitic foliation (ASM10, dated sample); (F) banded felsic granulite, marked by an alternation of mafic-rich and quartz-feldspar-rich layers; (G) typical undeformed mafic granulite, showing granoblastic texture; (H) orientated quartz ribbons in mafic granulite, characterizing a slight deformation; (I) deformed mafic granulite layer hosted in felsic granulite, showing pervasive foliation; (J) mineral stretching lineation in felsic granulite; (K) rotated feldspar porphyroblast in felsic granulite; (L) S-C structure in migmatic felsic granulite.

5 PETROGRAPHY

In this section, we describe the main petrographic features of the main lithotypes present in the study area, i.e. aluminous migmatite, felsic granulite, mafic granulite and amphibolite schollen.

5.1 ALUMINOUS MIGMATITES

Aluminous migmatites consist of alternating granulite residue and leucosome layers that range in size from a few millimeters to several centimeters (Fig. 2.3, 2.5). Two distinct facies of the residue are recognizable: (i) Opx-Grt granulite (Fig. 2.5a, b, c, d, e – sample ASM09A) and (ii) Sil-Grt granulite (Fig. 2.5f, g, h – sample ASM19A). Residue bands exhibit granonematoblastic texture and are mainly composed of quartz (20-35%), plagioclase (40-55%), alkali-feldspar (5-15%), garnet (10-20%), cordierite (8-16%), biotite (2-16%) and orthopyroxene (<1-7%). rutile, ilmenite, sulfides, zircon, monazite and spinel are accessory minerals.

5.1.1 Opx-Grt granulite resiude (sample ASM09A)

The garnet grains occur generally as coarse porphyroblastic grains up to 7 mm and commonly contains inclusions of quartz, biotite, K-feldspar, plagioclase and rutile (Figs. 4e, 5), except for some peritectic grains (~0.4 mm) which lack inclusions (Fig. 4d) or have small spinel inclusions. Garnet shows five different textural associations: (i) a garnet core with inclusions of quartz, K-feldspar, biotite and rutile; (ii) a clear garnet mantle with rarely developed inclusions of orthopyroxene, quartz and plagioclase (Fig. 5a, b); (iii) relatively thin garnet rim, which also carries mineral inclusions of quartz and K-feldspar (Figs. 4e, g, 5a, b); (iv) small peritetic grains (Figs. 4d, 5a); (iv) embayed porphyroblastic garnet rim in contact with symplectitic minerals like cordierite, plagioclase, quartz, K-feldspar and later biotite (Figs. 4c, e, 5a, b).

Biotite shows three distinct forms: (i) small inclusions in garnet core (Fig. 2.5a); (ii) in embayed porphyroblastic garnet rim accompanied with plagioclase, cordierite and quartz (M4); and (iii) small laths in the matrix (Fig. 4h).

Cordierite is medium-grained and always occur replacing porphyroblastic garnet rims and orthopyroxene and is often associated with biotite flakes forming coronas around garnet (Fig. 2.5c, e, g).

Orthopyroxene occur in two distinct forms: (i) as small inclusions in garnet rim, or (ii) as nematoblastic medium-grained grains in rock matrix. Both types are highly fractured and replaced by cordierite and later biotite (Fig. 2.5a, c, e).

Quartz occurs as inclusions in the garnet core, mantle, rim and also as anhedral or elongated crystals in the matrix. Plagioclase occur in four distinct forms: (i) as inclusion ins garnet mantle (Fig. 2.5e), as antiphertitic plagioclase with exsolved K-feldspar lamellae (Fig. 2.5e, (iii) anhedral medium-grained aggregates in rock matrix with K-feldspar; and (iv) replacing porphyroblastic garnet rims with cordierite. K-feldspar is rare and very fine-grained, occur as isolated grains in rock matrix or as lamellae in antiphertitic plagioclase.

Accessory minerals include rutile, zircon, monazite and sulfides (Figs. 4–5). The rutile grains occur both within garnet and in the matrix. It is partly replaced by ilmenite during retrograde metamorphism (Figs. 4k, 5).

5.1.2 Sil-Grt granulite residue (sample ASM19A)

The garnet grains occur generally as coarse porphyroblastic grains up to 6 mm and commonly contains inclusions of quartz, biotite, silimanite, K-feldspar and plagioclase (Figs. 4e, 5), except for some peritectic grains (~0.5 mm) with lobate quartz inclusions (Fig. 4d). Garnet shows five different textural associations: (i) a garnet core with inclusions of quartz, K-feldspar and biotite; (ii) a garnet mantle with rarely developed inclusions of silimanite and plagioclase (Fig. 5a, b); (iii) relatively thin garnet rim, which also carries mineral inclusions of quartz and sillimanite (Figs. 4e, g, 5a, b); (iv) peritectic garnet with typical (Figs. 4d, 5a), (v) embayed porphyroblastic garnet rim in contact with symplectites minerals like cordierite, plagioclase, silimanite, quartz, K-feldspar and later biotite (Figs. 4c, e, 5a, b),

Sillimanite shows two distinct morphologies: (i) needle-like inclusion in garnet mantle-rim (Fig. 2.5f); or (ii) as delicate intergrowths with biotite, plagioclase, cordierite and quartz around garnet rims (Fig. 2.5g).

Cordierite is medium-grained and always occur replacing porphyroblastic garnet rims and is often associated with biotite flakes forming coronas around garnet (Fig. 2.5c, e, g).

Biotite shows three distinct forms: (i) small inclusions in garnet core (M1) (Fig. 5a); (2) accompanied with sillimanite, plagioclase, cordierite and quartz in the embayed porphyroblastic garnet rim (M4); and (3) small laths in the matrix (after M4) (Fig. 4h).

Quartz occurs as inclusions in the garnet core, mantle, rim and also as anhedral or elongated crystals in the matrix (Fig. 2.5f, g, h, i). Plagioclase occur in as two distinct forms: anhedral medium-grained aggregates in rock matrix with K-feldspar (Fig. 2.5e); and (iv) replacing porphyroblastic garnet rims with cordierite. K-feldspar is rare and very fine-grained, occur as isolated grains in rock matrix (Fig. 2.5h).

Melt is assumed to be widely distributed in both samples based on the following textures: (i) the presence of elongated or rounded quartz in garnet suggest the involvement of melt in the growth of garnet (Figs. 2.5e;Groppo et al., 2012); (ii) peritectic garnet in the matrix (Fig. 2.5c; Sawyer, 1999); (iii) the textures of symplectite corona of sillimanite, plagioclase and biotite around garnet rim during the M4 stage (Fig. 2.5)

Based on the textural observations and reaction relationships four metamorphic stages can de distinguished for the two samples: the prograde metamorphic stage represented by Pl + Kfs + Qz + $Grt_{(core)}$ + Bt + Rt (ASM09A) and Kfs + Pl + Qz + $Grt_{(core)}$ + Bt + Sil + Ilm (ASM19A), which were included in the core of the porphyroblastic garnet (M1); the peak metamorphic stage (M2) characterized by Kfs + Pl + Qz + $Grt_{(mantle)}$ + Opx + Rt + Ilm + L (ASM09A) and Kfs + Pl + Qz + $Grt_{(mantle)}$ + Sil + Ilm + L (ASM19A) as inclusions in the mantle of porphyroblastic garnet and developed in the rock matrix; the third stage (M3) comprising recrystallized small symplectite assemblage of Pl + Kfs + Qz + $Grt_{(rim)}$ + Opx + Crd + Ilm + L (ASM09A) and Kfs + Pl + Qz + $Grt_{(rim)}$ + Crd + Sil + Ilm + L (ASM19A); fourth metamorphic (M4) stage is represented by Pl + Kfs + Qz + $Grt_{(rim)}$ + Bt + Crd + Ilm (ASM09A) and Pl + Kfs + Qz + $Grt_{(rim)}$ + Bt + Crd + Sil + Ilm (ASM19A)

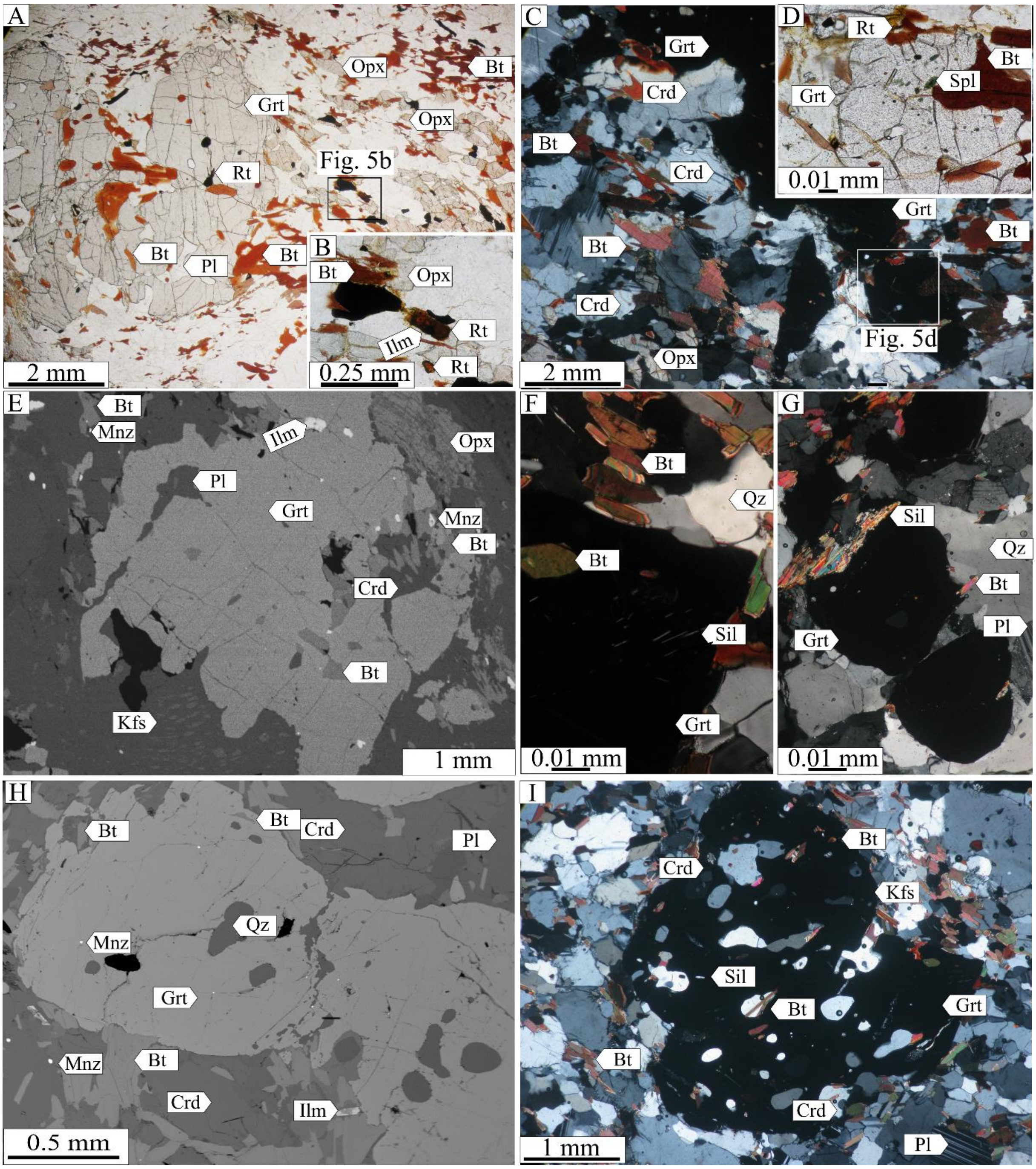

Figure 2.5 Petrographic aspects of aluminous rocks from the Novolândia Granulite. PPL = parallel-polarized light and CPL = cross-polarized light. Opx-Grt granulite – sample ASM09A(A-D); (A) garnet porphyroblasts with biotite and rutile as inclusions, biotite surrounding garnet rims and orthopyroxene grains with biotite coronas (PPL); (B) detail of rutile with ilmenite corona and biotite replacing orthopyroxene (PPL); (C) Opx-Grt granulite, showing significant cordierite replacement of garnet rims, with later biotite formation(CPL); (D) detail of garnet grain showing spinel inclusion in its core and rutile formation with garnet rim without ilmenite corona(PPL); (E) BSE image showing a garnet porphyroblast with biotite and plagioclase inclusions and in contact with orthopyroxene, and the cordierite + biotite replacement of garnet, and antiphertite plagioclase with K-feldspar lamellae. Sil-Grt granulite - sample ASM19A(E-G), (F) with garnet porphyroblasts displaying sillimanite and biotite inclusion in its mantle; (G) Sil-Grt granulite showing sillimanite replacing garnet rim; (H) BSE image of the Sill-Grt with a garnet aggregate with quartz and monazite inclusions and surrounded and replaced by cordierite and later biotite; (I) decomposed garnet porphyroblast with small inclusions of biotite in core and outer rim, garnet rim replaced by cordierite and later biotite.

5.2 FELSIC GRANULITES

Most felsic granulites (Fig. 2.4a, d, e, f and 2.6a, b, c) exhibit granoblastic texture (Fig. 2.6a). In contrast, some samples show alternating dark green, fine-grained bands with pyroxene and biotite alternated with quartz-feldspar layers (Fig. 2.6b, c). They are composed of quartz (20-35%), plagioclase (40-55%), alkali-feldspar (5-15%), biotite (2-16%), orthopyroxene (<1-7%), clinopyroxene (<1%), with ilmenite, pyrite, zircon and monazite as accessory minerals. Plagioclase, quartz and K-feldspar are equidimensional in granoblastic samples. In mylonitic rocks, K-feldspar porphyroblasts are up to 6 mm and quartz ribbons are commons (Fig. 2.6b, c). Some ternary feldspars are present as antiphertitic plagioclase. Orthopyroxene is medium-grained, usually highly fractured, and surrounded by biotite coronae (Fig. 2.6a, b, c). In deformed samples, orthopyroxene defines the foliation together with biotite (Fig. 2.6b, c). Clinopyroxene is rare and very fine-grained. Accessory phases are tiny apatite, ilmenite and zircon grains, with minor pyrite and chalcopyrite.

5.3 MAFIC GRANULITES

Mafic granulites (Fig. 2.4a, c, g, i and 2.6d, e) exhibit granoblastic texture, and are composed of plagioclase (20-40%), quartz (7-15%), orthopyroxene (20-40%), clinopyroxene (10-23%), amphibole (<1-8%), biotite (<1-10%), magnetite, ilmenite, zircon and sulfides are accessories. Anhedral matrix ortho- and clinopyroxene, plagioclase and minor quartz grains are equidimensional (Fig. 3.6d). Amphiboles occur as tiny inclusions in pyroxene and, more often, as coronae around pyroxenes (Fig. 2.6d). Biotite always occurs surrounding pyroxenes grains. Accessory phases are fine-grained.

5.4 AMPHIBOLITE SCHOLLEN (SAMPLE ASM34B)

There are various types of enclaves with different field aspects and host rocks. The mafic schollen hosted in an aluminous migmatite. The amphibolite (Fig. 2.4b, 2.6f) exhibits nematoblastic texture, and is composed of amphibole (~50%), plagioclase (~35%), quartz (~10%), clinopyroxene (~5%), orthopyroxene (<1%) and biotite (<1%); zircon, ilmenite, magnetite, apatite and sulfides are accessory minerals. The matrix is composed of equidimensional amphibole, plagioclase and quartz. Clino- and orthopyroxene occur as fine-grained, xenoblastic grains (Fig 2.6f). Biotite flakes commonly replace amphibole and uralitized pyroxenes.

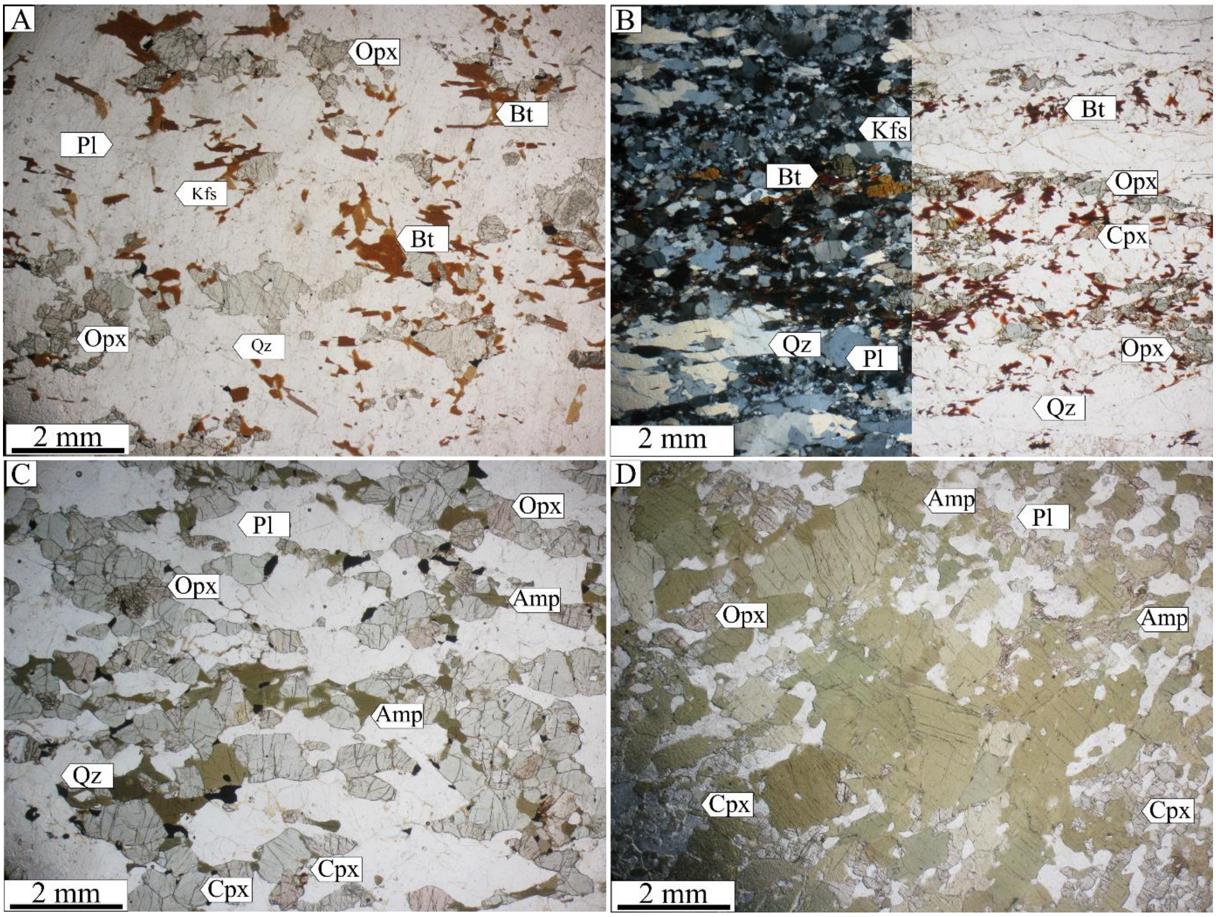

Figure 2.6 Petrographic aspects of orthoderived rocks from the Novolândia Granulite. (A) granoblastic felsic granulite showing granoblastic orthopyroxene grains surrounded by biotite; (B) mylonitic felsic granulite with alternated layers of nematoblastic orthopyroxene associated with biotite and layers of quartz-feldspar composition; (C) typical two granoblastic pyroxenes mafic granulite, with associated amphibole; (D) typical amphibolite with amp + pl association and minor clinopyroxene, possibly representing fully retrogressed mafic granulite.

6 MINERAL CHEMISTRY

We have focused on the mineral chemistry and the upcoming thermobarometry section on the residue of two aluminous migmatic rocks (Opx-Grt aluminous granulite residue – sample ASM09A; Sill-Grt aluminous granulite residue – sample ASM19A) because they have the best mineral assemblages to constrain *P-T* conditions. Representative mineral compositions of the studied samples are shown in supplementary tables 1 and 2.

6.1 GARNET

Two different textural types of garnet were identified: (i) inclusion rich garnet porphyroblasts (up to 8 mm) (Fig. 2.5a, c, e, f), and (ii) inclusions free or poor small (~0.5 mm) garnet grains classified as peritectic grains (Fig. 2.5d). Garnet does not show wide compositional variation in both samples (Fig. 2.7). In sample ASM09A the general formula for type I is $Alm_{57-67}Prp_{28-39}Grs_{2.6-3.4}Sps_{1.4-2}$ and $Alm_{70-77}Prp_{18-24}Grs_{2.7-3.3}Sps_{1.5-2.1}$ in sample

ASM19A. The chemical profile shares some similarities in both samples; however, it is more flattened in sample ASM9A garnet while sample ASM19A garnet records a more conspicuous chemical zoning. Garnets show a relatively Prp enriched core with rim ward decreasing and an opposite almandine pattern. From core to rim, the contents in sample ASM19A garnet show a rim-ward increase of spessartine and rim-ward decrease of grossular, whereas grossular increases from the mantle to the rim in sample ASM09A garnet.

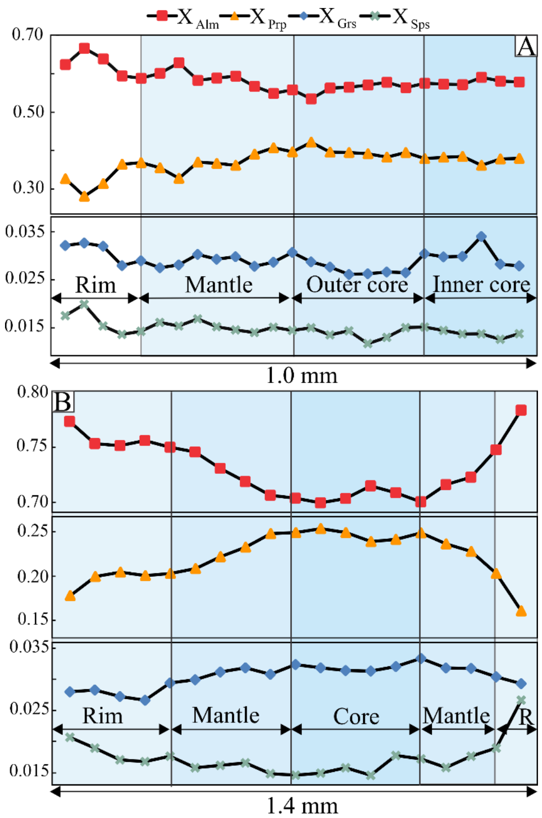

Figure 2.7 Representative EPMA garnet (i) profiles used to construct isopleths in pseudosection. (A) type I garnet sample ASM9A, (B) type I garnet in sample ASM19A.

6.2 BIOTITE

Biotite shows a wide compositional variation in Fe/Mg ratio and Ti content in different samples and different textural modes in the same rock (Fig. 2.8a). In sample ASM09A, biotite associated with cordierite shows the highest TiO_2 (6.24-6.41 wt%) and X_{Mg} (0.59-0.61), inclusions in garnet show TiO_2 around 5.06-5.50 wt% and X_{Mg} (0.61-0.64). The biotite crystals formed around orthopyroxene and garnet show lower Ti content, with TiO_2 4.52-5.32 wt% and 4.94-5.16 wt%, and higher X_{Mg} values – 0.61. In the sample ASM19A, Biotite included in garnet shows higher TiO_2 (3.50-5.65 wt%) and X_{Mg} of 0.59-0.57. Biotite around garnet has TiO_2 of 3.72- 5.42 wt% and X_{Mg} of 0.48, in the rock matrix it shows the lowest TiO_2 contents of 4.00- 4.49 wt% and X_{Mg} of 0.48.

6.3 CORDIERITE

Cordierite occurs usually with biotite around garnet crystals. It does not show substantial compositional variations in terms of Fe-Mg distribution in both samples, with X_{Mg} of 0.79-0.81 in sample ASM9A and of 0.82-0.84 in sample ASM19A. Oxide sum in its composition usually is around 99wt%, suggesting a possible presence of volatiles in its structure.

6.4 ORTHOPYROXENE

Orthopyroxene is found only in sample ASM09A. It shows a compositional variation in terms of Fe–Mg distribution and Al content according to their textural occurrence in the samples. Orthopyroxene inside garnet porphyroblasts shows alumina zoning varying from 5.47 wt% (rim) to 6.96 wt% (core) and $X_{Al(M1)}$ ranging from 0.18 (core) to 0.13 (rim). Orthopyroxene in contact with garnet shows a narrower alumina variation, with contents between 5.46-6.48 wt%, and the lowest values close to the garnet-pyroxene boundary. $X_{Al(M1)}$ varies in these crystals ranges between 0.11 (core) and 0.16 (rim) (Fig. 2.8b). The rock matrix pyroxene phases without biotite coronae have higher alumina contents.

6.5 PLAGIOCLASE

Plagioclase does not show compositional variation in different textural modes. In the sample ASM09A plagioclase inside garnet shows core anorthite contents of X_{An} (0.29-0.31) and rims with X_{An} (0.29). In the rock matrix, the anorthite contents are X_{An} (0.28) and rim X_{An} (0.30) (Fig. 2.8c). In the sample ASM19A, plagioclase in the rock matrix shares a similar pattern, the core has X_{An} (0.29) and rim (X_{An} 0.26).

6.6 SPINEL

Spinel is found only as inclusions in garnet in sample ASM09A. It is a compositionally solid solution of hercynite and spinel with a variable amount of gahnite component. Ferric iron is absent. Ulvöspinel, chromite, galaxite, and trevorite components are insignificant.

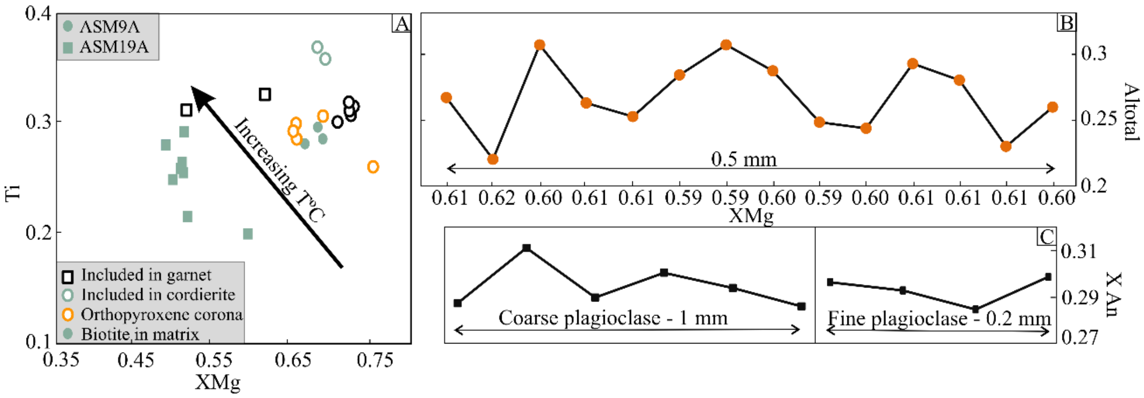

Figure 2.8 (A) XMg vs. Ti diagram showing the compositions of biotite in samples ASM09A and ASM19A; (B) XMg vs. Al total profile in orthopyroxene; (C) X_{An} profiles of plagioclases in sample ASM09A. X_{Mg} = Mg / (Mg + Fe2++ Mn2+), Altotal = Al^{vi} + Al^{iv}, X_{An} = Ca / (Ca + Na + K).

7 PRESSURE-TEMPERATURE CONDITIONS

7.1 PSEUDOSECTION MODELING

For the pseudosection modeling the whole-rock chemical compositions from two representative aluminous migmatite residue of pelitic composition (samples ASM09 and ASM19A) (Tab. 2.1) were determined by X-Ray Fluorescence spectrometry at the ALS laboratory, Belo Horizonte, Brazil. The minor P_2O_5 and MnO contents were ignored due to its low concentration and no significant effects in high-grade metamorphic rocks (White et al., 2007)

Phase equilibria were modeled with Theriak-Domino (De Capitani and Petrakakis, 2010), using the MnNCKFMASHTO (MnO-Na_2O–CaO–K_2O–FeO–MgO–Al_2O3–SiO_2–H_2O–TiO_2–Fe_2O_3) system, which provides realistic estimates for metapelites (White et al., 2007). We used the internally consistent thermodynamic dataset of Holland and Powell (1998) with the re-parameterized a-x models: garnet and biotite (White et al., 2005), cordierite (Holland and Powell, 1998), plagioclase and K-feldspar (Holland and Powell, 2003), white mica (Coggon and Holland, 2002), orthopyroxene and spinel (White et al., 2002), ilmenite (White et al., 2000), silicate melt (White et al., 2007). Pure phases included water (H_2O), sillimanite, kyanite, andalusite, rutile, sapphirine and quartz.

Field and microstructural evidence indicate that some samples underwent partial melting (Fig. 2.3a, b, c, 2.5d, e). Therefore, we defined the H_2O contents with the T-$M_{(H2O)}$ diagram to ensure that water content is enough to saturate the final stage assemblage (e.g., Korhonen et al., 2012). Furthermore, the existence of sulfides, ilmenite and absence of magnetite indicates a low oxygen fugacity. Thus, we chose the minimum X_{Fe2O3} (0.01) for calculation.

Melt loss is an essential part of preserving granulite facies mineral assemblages (e.g., White and Powell, 2002; Zhang et al., 2017). Some melt batches may have been lost before granulite facies rocks reached their peak temperature metamorphic conditions owing to the preservation of granulitic assemblages (Kelsey et al., 2003; White and Powell, 2002)no. Also, there is no significant change of the mineral phases and compositions above solidus fields comparing *P-T* pseudosections made with measured bulk composition and the ones using melt re-integrated techniques (Groppo et al., 2010; Indares et al., 2008). Therefore, a melt re-integration approach is not applied here. Consequently, we will only discuss peak to post-peak conditions.

7.1.1 Opx-Grt granulite residue (sample ASM09A)

The *P–T* pseudosection for sample ASM09A (Opx-Grt granulite residue) is calculated with quartz, ilmenite, and plagioclase in excess. The *P–T* window ranges between 5 and 10 kbar and between 700 and 1150°C (Fig. 2.9) using the normalized bulk-rock mole composition in Tab. 1. The fluid-absent solidus occurs at temperatures above 800°C. Rutile is stable above 5.5 kbar. Biotite is modeled to occur below ~820 ºC. Orthopyroxene is stable at up to ~7 kbar in temperatures up to ~1000 ºC or in all the covered pressure fields at temperatures higher than ~1000 ºC. Cordierite occur in low-pressure fields, occurring only below ~7 kbar, above solidus.

The inferred peak assemblage (Grt + Pl + Kfs + Opx + Ilm + Rt + Qz + L) occupies a field with P–T conditions of 6-9 kbar/1000-1060 °C. The maximum X_{Grs} (0.027– 0.29) in the core depicts a peak pressure of ~9kbar, while the average X_{An} of 0.29 yields a peak temperature of ~1050ºC.

The inferred post-peak assemblage (Grt + Pl + Kfs + Opx + Crd + Ilm + Qz + L) occupies a large field with *P-T* conditions of 6-7 kbar and 900-950 ºC. The little outward decrease of X_{Grs} (0.026–0.028) in the mantle of garnet, the maximum of $X_{Al(M1)}$ in orthopyroxene core (0.17-0.20), the outwards increasing X_{An} (0.25–0.28), from the core to mantle in plagioclase match a cooling and decompression process from the peak to the post-peak conditions.

The inferred final assemblage featured by later growth of biotite around garnet and orthopyroxene together with garnet K-feldspar, plagioclase (+ Qz + Ilm) is predicted to be stable within a P–T range of 6–7 kbar/700–800 °C, consistent with X_{Grs} (0.031-0.033) increasing from mantle do rim.

Table 2.1 Bulk-rock composition of the studied samples

X-ray fluorescence whole-rock composition (wt%)

Sample	SiO_2	TiO_2	Al_2O_3	FeO^T	MnO	MgO	CaO	Na_2O	K_2O	P_2O5	LOI	Total
ASM09A	54.05	0.93	19.35	10.99	0.18	6.36	2.00	2.23	1.67	0.04	0.53	98.32
ASM19A	65.74	0.75	15.96	5.48	0.07	2.1	1.56	2.46	3.52	0.09	0.54	98.8
Normalized molar proportions used for phase equilibria modeling (mol%)												
Sample	SiO_2	TiO_2	Al_2O_3	FeO	Fe_2O_3	MnO	MgO	CaO	Na_2O	K_2O	H_2O	-
ASM09A	50.83	0.66	21.45	8.65	0.01	0.14	8.92	2.02	4.07	2.0	1.25	-
ASM19A	62.67	0.54	17.94	4.31	0.01	0.06	2.98	1.59	4.55	4.28	1.08	-

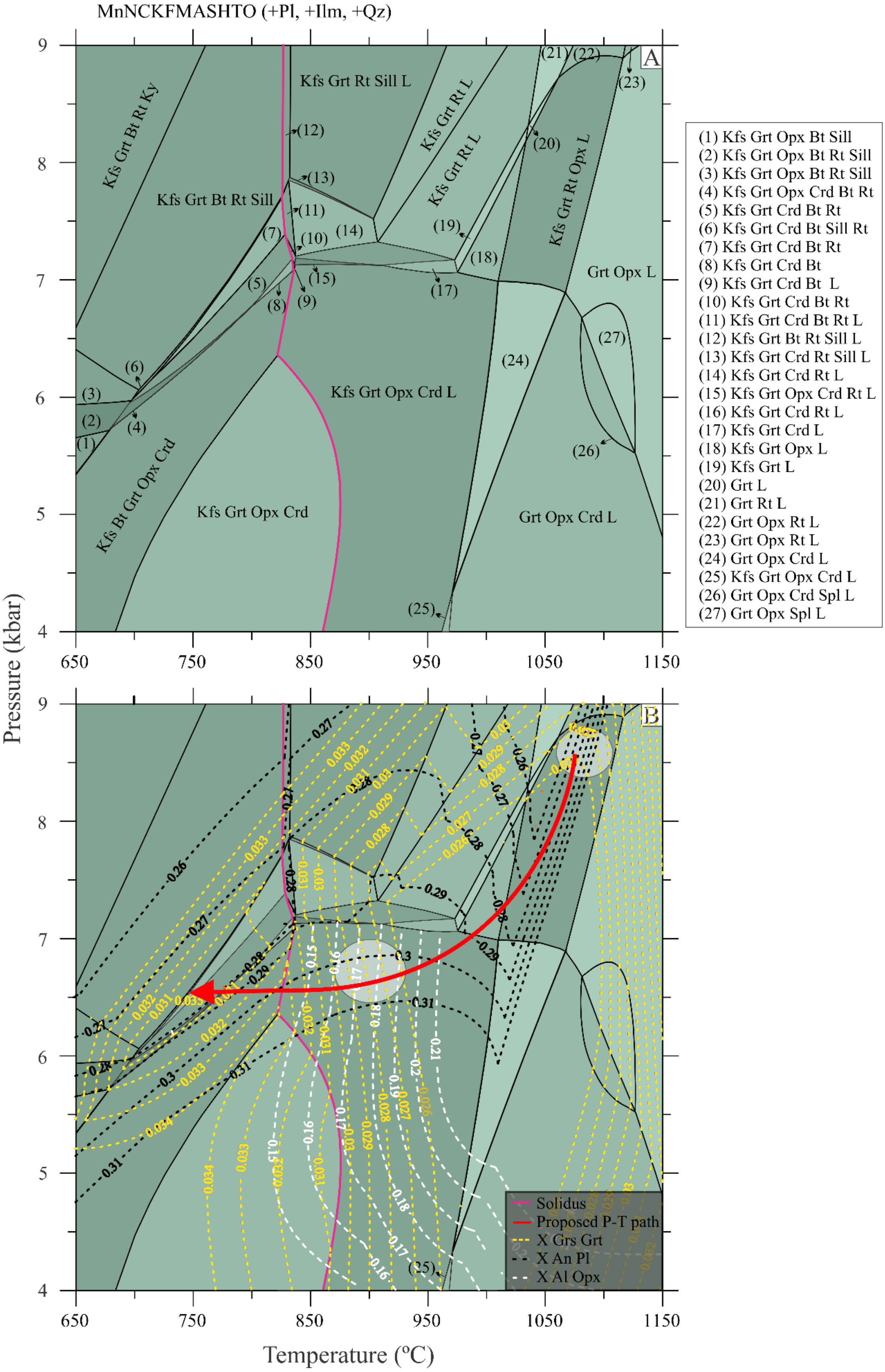

Figure 2.9 (A) P–T pseudosection calculated from the measured bulk composition of sample ASM9A (Opx-Grt aluminous granulite residue); (B) Inferred P-T path based on stability fields and isopleths of X_{Grs} in garnet, X_{An} in plagioclase, and $X_{Al(M1)}$ in orthopyroxene. White circles indicate the inferred stable P-T intervals.

7.1.2 Sil-Grt granulite residue (sample ASM19A)

The P–T pseudosection calculated for sample ASM19A is drawn with quartz, ilmenite, and plagioclase in excess in the *P–T* window of 3.5–10 kbar and 650–1100°C (Fig. 2.10) using the normalized bulk-rock mole composition in Tab. 1. The fluid-absent solidus occurs at temperatures of ~ 700 °C. Rutile is stable above ~6.8 kbar. Biotite is modeled to occur below ~750 ºC. Orthopyroxene is stable below ~5.5 kbar at temperatures lower than 950 ºC, and at higher temperatures, it is stable up to 7 kbar.

The inferred peak assemblage (Pl + Kfs + Grt + Sil + Ilm + Qz + L) occupies a field with P–T conditions of 6-9 kbar/1000-1060 °C. The maximum X_{Grs} in the garnet core (0.031–0.33) depicts a peak pressure of ~ 8 kbar, while the average X_{An} of 0.28 in plagioclase yields a peak temperature of 950 ºC.

The inferred post-peak assemblage (Pl + Kfs + Grt + Crd + Sil + Ilm + Qz + L), which shows the appearance of cordierite surrounding garnet crystals, occupies a restricted field with *P-T* conditions of 6-6.5 kbar and 840-850 ºC. The outwards decreasing X_{Grs} (0.029-0.27) in the garnet mantle matches a cooling and decompression process from the peak to the post-peak conditions.

The inferred final assemblage featured by later growth of biotite (Pl + Kfs + Grt + Crd + Bt + Sil + Ilm + Qz), usually surrounding crystals of garnet and cordierite crystals, is predicted to be stable within a P–T range of 5–7.5 kbar/650–730 °C, bounded by the fluid-absent solidus and biotite-out curve on the temperature limits.

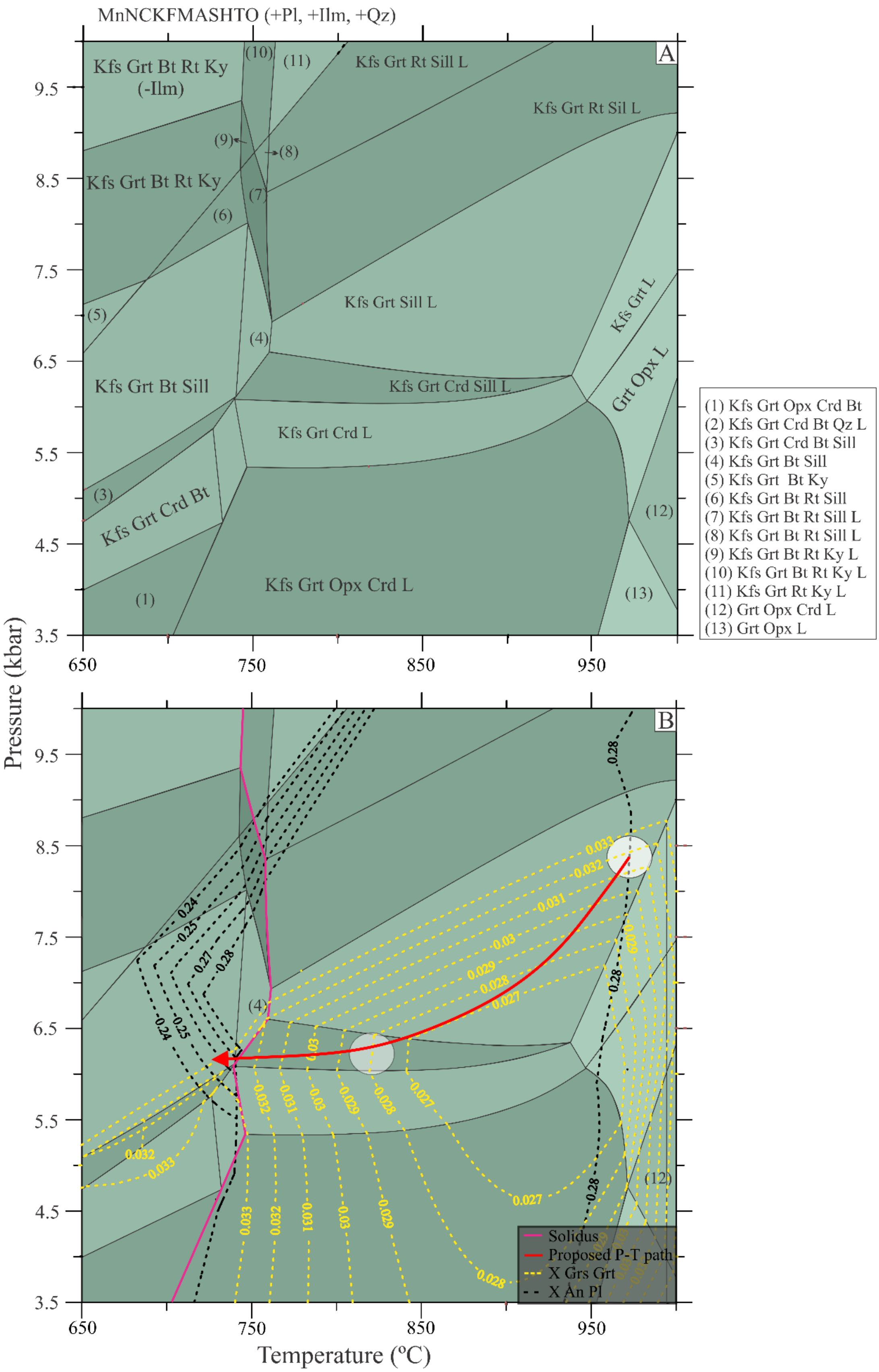

Figure 2.10 (A) P–T pseudosection calculated from the measured bulk composition of sample ASM19A (Sil-Grt aluminous granulite residue); (B) Inferred P-T path based on stability fields and isopleths of X_{Grs} in garnet, X_{An} in plagioclase. White circles indicate the inferred stable P-T intervals.

7.2 CONVENTIONAL THERMOBAROMETRY

We used compositions of coexisting garnet and orthopyroxene (sample ASM09A) to estimate the pressure-temperature conditions of peak metamorphism using Al-solubility-based thermobarometry, corrected for late Fe-Mg exchange (Pattison et al., 2003). The *P-T* estimation was made assuming that the Tschermaks exchange vector controls Al content in orthopyroxene and that Al diffusion is negligible (Kelsey and Hand, 2015). Peak metamorphic conditions are calculated using garnet and orthopyroxene core compositions resulting in an interval of 1017-1037 ºC and 8.59-9.52 kbar (quite similar to the P-T conditions obtained in the pseudosection).

The Ti-in-garnet thermometer is also useful to constrain temperature conditions in UHT granulites (Kawasaki and Motoyoshi, 2016). Using the maximum pressure obtained in both pseudosections and the maximum Ti in garnet from both samples, we obtained the temperature of ~1050°C at 9 kbar (Ti_{max} = 0.007/NTi = 0.014) in the sample ASM09A, and ~900ºC at 8.5 kbar in sample ASM19A (Ti_{max}= ~0.005/NTi = 0.01), which are coherent with the previously cited results.

8 U-PB GEOCHRONOLOGY

Due to the lithological diversity of the studied Novolândia granulite belt, one representative sample of each variety was selected for dating, summing four samples (Fig. 2.11 and 2.12, Tab. 2). U-Pb data are available in Supplementary Material 2.

To retrieve the protolith ages from orthoderived high-grade metamorphic rocks, when possible, we used an approach similar to the one used by Whitehouse and Kemp (2010), summarized below:

1) An investigation of the internal structure of zircon through backscattering (BSE) imaging to identify the core, successive rim generations, and single grains showing specific BSE -responses (Fig. 2.11).

2) U-Pb zircon core ages of one sample are assumed to represent a single magmatic event. The oldest grains in this data cluster are thus considered to represent the minimum crystallization age while the younger dates are attributed to either Pb loss or resetting during metamorphism. These processes are especially relevant for rocks that were strongly affected by partial melting (Gerdes and Zeh, 2009; Rubatto, 2017).

3) Evaluation of the Th/U ratios to infer metamorphic or igneous origin (Rubatto, 2017; Yakymchuk et al., 2018).

8.1 ALUMINOUS GRANULITE RESIDUE

A representative sample from migmatic aluminous granulite residue was selected to investigate the ages of detrital sources and the age and duration of the UHT event. Two distinct zircon texture types were identified. In the first (Group I), zircon grains are prismatic with rounded edges and show blurred oscillatory and sector zoning, with homogenous rims. In the second group (Group II), the grains show typical patterns of high-grade metamorphic rocks (Corfu et al., 2003; Taylor et al., 2016), mostly in soccer ball form. Subordinately, they are prismatic (Fig. 2.11), homogeneous, and sector zoning is rare.

The sample ASM09A (Opx-Grt granulite residue) is representative of aluminous granulite residue (Fig. 2.12a). 100 analyses were performed, 34 U–Pb isotopic analyses were considered on Group I, yielding a spectrum with apparent ^{207}Pb/^{206}Pb ages (10% of discordance) from 3320±31 Ma (2s) to 2608±18 Ma (2s, Fig. 2.11c) with peaks at c. 3.32-3.18 Ga and 2.98–2.86 Ga, and showing Th/U ratios of 2.27–0.01 (Fig. 2.12b).

Eleven analyses on the rims of group I grains and group II grains (Fig. 2.12a) provided a discordia with an upper intercept of 2075±13 Ma (2s, MSWD = 1.6), whereas four grains (with discordance lower than 5%) yielded an upper intercept of 2070±9 Ma (2s, MSWD = 2.3). All the analyzed grains show Th/U ratios of 0.05-0.94.

8.2 FELSIC GRANULITE

A representative sample from felsic granulites was selected to investigate the ages of magmatic protoliths and the ages of high-grade metamorphism imprinted in these rocks. Sample ASM10 is a felsic granulite. Zircons are brownish to yellowish, with elongation ratios of 2 to 4. They vary in size from 20 µm to 270 µm. All grains are anhedral, short to long prismatic, with rounded edges. Two textural types are distinguished: (i) zircon grains with cores showing blurred oscillatory zoning associated with local resorption and unzoned homogenous rims (Fig. 2.11) with rare xenoticrystic cores; (ii) completely homogeneous zircons grains (Fig. 2.11).

82 analyses were performed on zircons grains from sample ASM10 (Fig. 2.12b). Core analyses provided two distinct sets of ages, discriminated in populations 1a and 1b. Core analyses from population 1a provided a discordia with an upper intercept age of 2744±21 Ma (2s, MSWD = 2.4) defined by 12 discordant spot analyses with Th/U ranging from 4.17 to 0.46. In contrast, the core analyses of population 1b provided a distinct discordia with an upper intercept of 2567±22 Ma (2s, MSWD=2.7) defined by 14 discordant spot analyses with Th/U ratios between 3.58 and 0.12. The rims and homogeneous grains (population 2) provided an upper intercept of 2094±9 Ma (2s, MSWD = 1.19) defined by 7 spot analysis with Th/U of

1.42-0.15. A single xenocrystic core provided a Paleoarchean $^{207}Pb/^{206}Pb$ apparent age of 3461±5 Ma.

8.3 MAFIC GRANULITE

The sample ASM13 is a mafic granulite. Zircon grains are brown and 20 to 250 µm in length. Two distinct textural aspects were identified. the first (i) is formed by prismatic grains, which display a blurred core-rim zonation or a parallel pattern (Corfu et al., 2003). The second (ii) is stubby with rounded edges and homogenous prismatic (Fig. 2.11).

80 analyses were performed in zircons grains for sample ASM13 (Fig. 2.12c), these analyses provided two distinct sets of ages. Population 1 provided an upper intercept of 2090±7 Ma (2s, MSWD = 1.14), defined by 34 grains, whereas 5 concordant grains (± 5% of discordance) yield a concordia age of 2082±7 Ma (2s, MSWD = 0.23). Th/U ratios range from 0.15 to 1.07. The population 2 analysis provided an upper intercept of 1921±16 (2s, MSWD = 0.88), with Th/U of 0.16-0.65.

8.4 AMPHIBOLITE SCHOLLEN

The sample ASM3AB is a cpx-amphibolite (Fig. 2.12e). Zircon grains are brown, with elongation ratios of 2 to 4 and lengths of 50 to 200 µm. They are long prismatic to stubby, with rounded edges (Fig. 2.11). Most grains are homogeneous, with multiple BSE responses, sometimes resembling a large core-rim zonation.

30 analyses of twenty-eight grains were performed for sample ASM34B (Fig. 2.12e). Core and rim analyses provided only one population (M population) with an upper intercept of 2035±14 Ma (2s, MSWD = 2.9) defined by twenty-four discordant spot analysis with Th/U of 0.22-7.38.

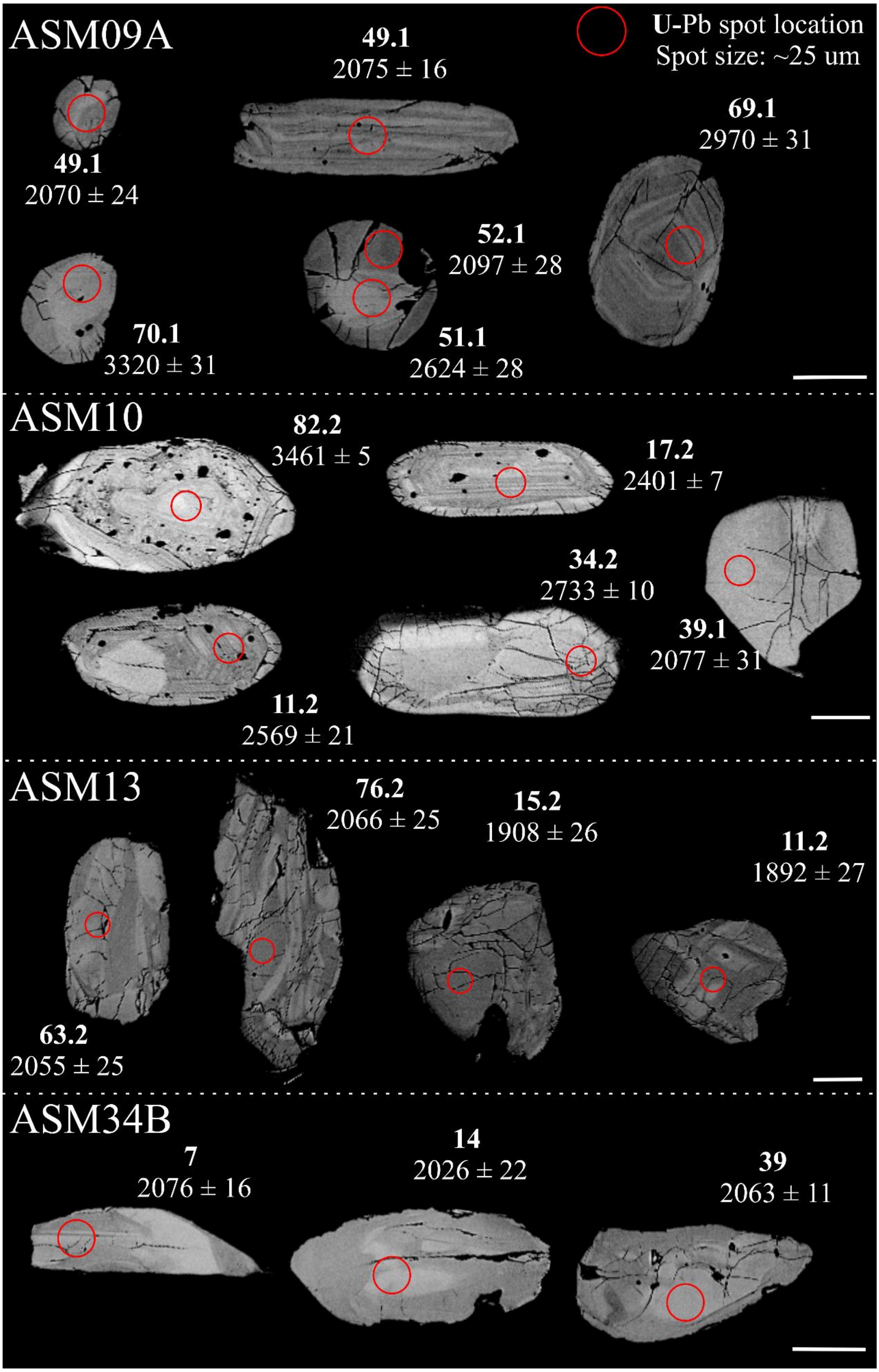

Figure 2.11 Representative BSE images of analyzed zircons grains. Ages represent apparent $^{207}Pb/^{206}Pb$ ages and uncertainties are at 2s. Scale bar ~50 µm.

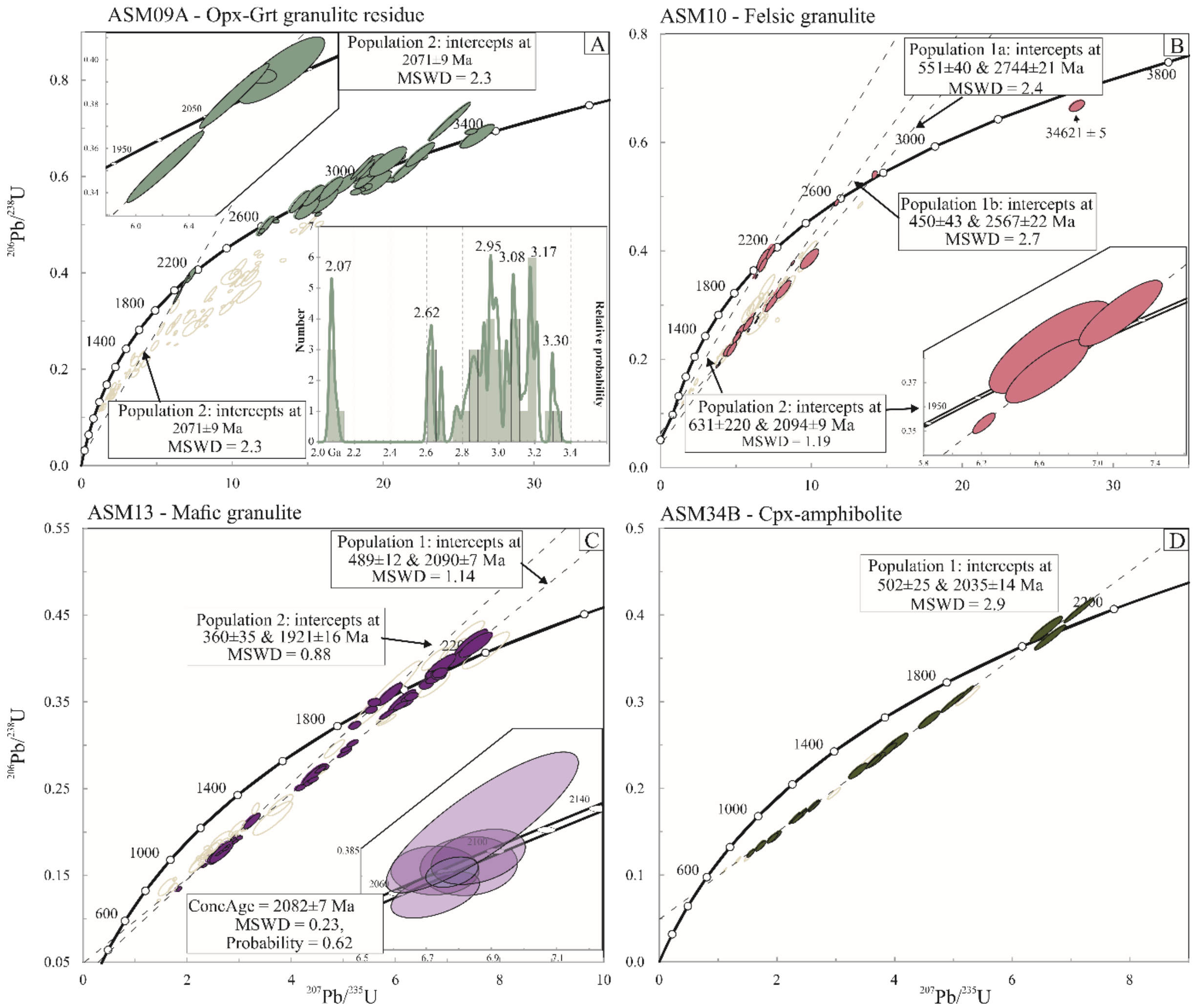

Figure 2.12 Concordia diagrams of analyzed samples, the color pattern follows the color in the map of Fig. 2 for each variety, light gay ellipses were discarded for age calculations. (A) sample ASM09A Opx-Grt granuliteresidue; (B) sample ASM10 Opx felsic granulite; (C) sample ASM13 mafic granulite; (D) sample ASM34B clinopyroxene amphibolite.

Table 2.1 Summary of field and structural aspects, geochronological data, metamorphic assemblages and *P-T* conditions (from pseudosection) of the Novolândia Granulite

Lithology	Field and structural aspects	Ages (Ga)	Mineral assemblages	*P-T* conditions (P - kbar, T - ºC)				
				Sample	Pre-peak	Peak	Post-peak 1	Post-peak 2
Aluminous migmatite	(1) stromatic and local fold-structured metatexite; (2) WNW-ESE sub-horizontal foliation; (3) ESE sub-horizontal mineral lineation; (4) NE trending leucosome	ca. 3.3 to 2.6 detrital sources ca. 2.07 metamorphism	Pre-peak: $Grt_{(core)}$ + Bt + Sil ± Spl ± Rt (Pl + Qz + Ilm) Peak: $Grt_{(mantle)}$ ± Opx ± Sil ± Rt + L (+ Kfs + Pl + Qz + Ilm) Post-peak 1: $Grt_{(rim)}$ + Crd ± Opx ± Sil + L (+ Kfs Pl + Qz + Ilm) Post-peak 2: $Grt_{(rim)}$ + Bt + Crd ± Sil (Pl + Kfs + Qz + Ilm)	ASM09 A	n.d	P: ~8-9 T: 1050-1070	P: 6.5-7 T: 875-925	P: 6-7 T: 700-800
				ASM19 A	n.d	P: ~7.7–8.8 T: 970-995	P: 6-6.5 T: 840-850	P: 4-7.5 T: 650-730
Felsic granulites	(1) EW to NW-SE banding; (2) mylonites; (3) moderate to sub-vertical E-W to WNW-ESE foliations; (3) sub-horizontal mineral stretching lineation; (4) sinistral S-C structures and porphyroblasts; (5) isoclinal folds with NE-SW trending axes	ca. 2.74 crystallization ca. 2.5 Pb lost or metamorphism ca. 2.09 metamorphism	Pre-peak: Bt ± $Grt_{(core)}$ (Pl + Qz + Ilm) Peak: Opx + L ± Cpx ± $Grt_{(mantle)}$ (Pl + Kfs + Qz + Ilm) Post-Peak: Bt ± $Grt_{(rim)}$ (Pl + Qz + Ilm)	[1]Peak: 5-13 kbar 701- ºC Post-peak: <700ºC				
Mafic granulite	(1) Isotropic to slight EW-mineral	Ca. 2.08 Crystallization	Peak: Opx+ Cpx + L (Pl + Qz + Ilm + Mt) Pos-peak: Bt ± Amp (Pl+ Qz + Ilm + Mt)	[1]Peak: 5-13 kbar				

	orientation; (2) flattened, boudin shape schollen in felsic granulites	ca. 1.92 metamorphism		658-816ºC Post-peak: <700ºC
Amphibolite	(1) angular and rounded schollen in felsic granulites and aluminous migmatite	ca. 2.03 Crystallization	Peak: Amp + Cpx ± Opx (Pl + Qz + Ilm + Mt) Post-peak: Bt (Qz + Pl + Ilm + Mt)	n.d

n.d – not determined, [1](Feio et al., 2016) using conventional thermobarometry.

9 DISCUSSION

9.1 METAMORPHIC EVOLUTION

Based on the petrographic data, phase equilibria modeling and conventional thermobarometry from two samples (ASM09A and ASM19A) of the granulite residue from the aluminous migmatites of the Novolândia granulite belt, we recognized a clockwise *P–T* path with peak UHT conditions followed by decompression-cooling and later near-isobaric cooling (Fig. 2.13).

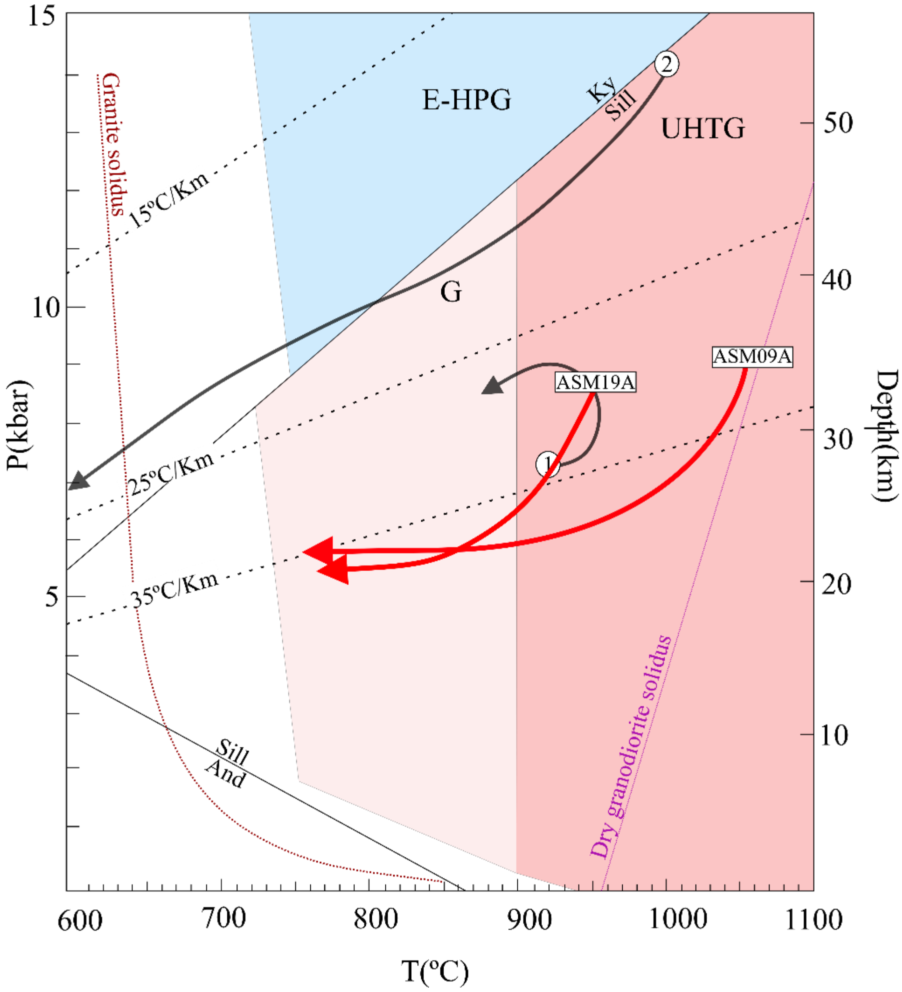

Figure 2.13 Summary P-T path of UHT granulites from the Transamazonian-Birimian orogens. (1) Sapphirine-bearing migmatic granulite from the Bakhuis Belt, Amazonian Craton (Rover et al. 2003), (2) HP-UHT mafic granulite from KénémaMan block, West Africa Craton (Triboulet and Feybesse, 1998). The granite solidus is the H2O-saturated solidus in the system Qz-Ab-Or-H_2O (Schulze et al., 1996). Dry solidus of granodiorite (Robertson and Wyllie, 1971). Theriak-Domino calculates the reactions of Al2SiO5. Abbreviations: G – 'normal' granulite facies; UHTG – ultrahigh-temperature granulite facies; E-HPG – eclogite-high-pressure granulite facies (Brown, 2007).

9.1.1 Peak UHT conditions

The peak condition estimated by pseudosection modeling for sample ASM09A (Opx-Grt granulite residue) is based on the inferred peak assemblage (Pl + Kfs + Grt + Rt + Ilm + Qz + L) and the plots of maximum X_{Grs} (0.027–0.029) in the core of garnet, together with the average X_{An} of 0.28 in plagioclase core-mantle. These results constrain a *P-T* range of 8-9 kbar/1050-1070 °C based on the stability of the inferred peak assemblage. The UHT conditions are also constrained conventional thermobarometers such as Grt-Opx thermometry raging values of 1017-1043 ºC and the Ti-in-garnet thermobarometry suggesting a ~1050 ºC at 9 kbar.

In this sample, spinel is included in garnet (Fig. 2.4d) and it is absent in the rock matrix. It is valid to point out that, when modeled, spinel occurs only in a very restricted field. We suggest three possible reasons for this configuration. (i) The garnet crystals with spinel inclusions have distinct petrographic features like smaller size, rounded forms, and lobate quartz inclusions (Fig. 2.5d), which are typical characteristics of grains formed due to peritectic reactions (e.g., Dunkley et al., 2008). However, as they occur in negligible amounts in these smaller grains, they were not fully encompassed by the modeling. (ii) Another possibility is that spinel inclusions represent local micro compositional domains not encompassed in the bulk-rock composition pseudosection. The last supposition (iii) is that the stability fields of spinel would change and perhaps enlarge with the addition of ZnO and Cr_2O_3 in the system (Nichols et al., 1992).

The peak condition for the Sil-Grt granulite residue, represented by sample ASM19A, is based on the peak stability inferred containing Pl + Kfs + Grt + Sil + Ilm + Qz + L assemblage, and the plots of maximum X_{Grs} (0.029–0.033) in the core of garnet, together with the average X_{An} of 0.28 in plagioclase core-mantle. These data provide a *P-T* condition of ~7.7–8.8 kbar and ~950-970 °C. The UHT conditions are also constrained conventional thermometer such as Ti-in-garnet thermobarometry suggesting a ~900 ºC at 9 kbar.

The *P–T* conditions in both samples are consistent with the recognized peak assemblages' stability field, mineral isopleths, the Ti-in-garnet thermometer, and Al-in-orthopyroxene geothermometer (sections 6.1 and 6.2). The sum of results suggests that the studied granulite residues have undergone an evolution under UHT peak conditions of ~950-1050 °C, although there is no evidence of the diagnostic mineral indicators summarized in Harley (2008). However, it is not unusual to find rocks that record UHT conditions that do not show diagnostic assemblages because the typical minerals reported by Harley (2008) develop only in Mg-Al rich rocks, which are relatively rare on the Earth (Kelsey and Hand, 2015). So far, there are some reports of UHT rocks lacking diagnostic mineral assemblages in the North China Craton (e.g., Liu et al., 2019; Liu and Wei, 2020) and in the Socorro-Guaxupé Nappe, Brazil (e.g., Motta et al., 2021; Rocha et al., 2018; Tedeschi et al., 2018).

9.1.2 Post-peak decompression-cooling

For sample ASM09A, this stage occupies a broad field, above 4 kbar/≤7 kbar and ~820-1010 ºC based on the stability field of the inferred decompression-cooling assemblage (Pl + Kfs + Grt + Opx + Crd + Ilm + Qz + L), which is marked by the decrease of X_{Grs} in garnet from core to mantle (0.026-0.028), together with $X_{Al(M1)}$ in orthopyroxene (0.18), and the increase from the core to the mantle of X_{An} in plagioclase (0.29-0.31). All these features match a typical decompression-cooling stage (e.g., Liu 2020).

For the sample ASM19A, this field occupies a restricted area of ~6.1-6.6 kbar, and ~740-940 ºC, based on the stability field of the post-peak assemblage (Pl + Kfs + Grt + Crd + Sil + Ilm + Qz + L), which is consistent with the decrease of X_{Grs} in garnet from core to mantle (0.027-0.028).

These results are supported by petrographic textures and mineral chemistry zoning. The post-peak decompression-cooling process is featured by the extensive growth of cordierite around the peak assemblage, usually replacing garnet rims (Fig. 2.3), a typical feature of a retrogressive path in UHT rocks (Kelsey and Hand, 2015). Finally, the cooling of the system can also be inferred by orthopyroxene crystals zoning with Al-rich cores and rim ward decreasing content (Kelsey and Hand, 2015; Pattison et al., 2003).

9.1.3 Post-peak isobaric cooling

For the sample ASM09A, the final assemblage yields cooling conditions of 6–7 kbar/700–780 °C, based on the stability field of Pl + Kfs + Grt + Crd + Bt + Rt + Qz, consistent with the increase of X_{Grs} in garnet from the mantle to the rim (0.032). For the sample ASM19A, the cooling condition is confirmed to be 5.1–7.8 kbar / 650–740 °C based on the stability of the final assemblage (Kfs + Pl + Grt + Bt + Ilm + Qz), the slight increase of X_{Grs} in garnet from the mantle to the rim (0.032) and average X_{An} (0.26) in the plagioclase rim.

The final-stage cooling process is not fully constrained in both samples but is revealed from the final assemblage's stability marked by the later growth of biotite. In this stage, biotite seems to grow from peak minerals as orthopyroxene and garnet (Fig. 2.5a, c, g), and from post-peak decompression-cooling phases, such as cordierite (Fig. 2.5c, e). Garnet zoning also suggests that this mineral were consumed during the retrograde path because it displays typical retrogressive zoning with Mn increase towards rims (Fig. 2.7) and the late Fe-Mg exchange with surrounding minerals (Florence and Spear, 1991; Xiang et al., 2014).

9.2 SIGNIFICANCE OF U-PB AGES OF GRANULITE ROCKS FROM SOUTH BACAJÁ

9.2.1 Detrital ages

The detrital age spectra for aluminous granulite residue yield apparent $^{207}Pb/^{206}Pb$ ages ranging from 3320±31 Ma to 2608±18 Ma, with maximum depositional age at c. 2.60 Ga (Fig. 2.12). The spectra of detrital ages are exclusively Archean, although the Bacajá domain and surrounding areas are well known by Archean to Proterozoic sedimentation ages (Salgado et al., 2019; Vasquez, 2006). The absence of Paleoproterozoic detrital grains may reflect the small number of concordant analyzed grains and because age spectra might not represent all detrital sources (Andersen, 2005).

We only have the data from one sample, although premature it is likely that the potential sources may be inferred based on our detrital ages. Potential sources for the Archaean zircons grains are prevalent in the basement of Bacajá and near the Carajás domain and the Amapá block. The oldest Mesoarchean peak of ~3.3-3.1 Ga might represent old crust in the studied area also indicated by the Paleoarchean inheritance in felsic granulites (section 7), ancient sedimentary sequences or the Paleo-Mesoarchean (3.5 to 3.1 Ga) crust from the Archean Amapá Block (see Fig. 1b) (Milhomem Neto and Lafon, 2019). The major Mesoarchean peak ranging from 3.0 to 2.8 Ga are consistent with the Archean basement of Bacajá and Carajás domains (see Fig. 2.1c, 2.14) (e.g., Feio et al., 2013; Vasquez and Rosa-Costa, 2008). The youngest peak of ~2.6 Ga can be related to the Rio Preto Magmatic Arc (Vasquez and Rosa-Costa, 2008) and the tectonothermal event/magmatism in Carajás (e.g., Melo et al., 2017; Teixeira et al., 2015).

9.2.2 Protoliths of felsic and mafic granulites

The U-Pb age record for the felsic granulite (ASM10) displays an intricate pattern, showing at least three zircon populations (Fig. 2.12b). Spot analyses on zircon from population 1a yielded an upper intercept age of 2744 ± 21 Ma; on the order hand, population 1b (Fig. 2.12b, supplementary table 4) yielded a discordant age of 2567 ± 22 Ma. Assuming the model proposed by Whitehouse and Kemp (2010), we considered the older age (~2.74 Ga) as the minimum crystallization age of the felsic granulite protolith, while the younger age (~2.56 Ga) represents either a metamorphic event or Pb lost. A single xenocrystic core in zircon grain #81.2 (Fig. 2.11) spotted a Paleoarchean 3461 ± 5 $^{207}Pb/^{206}Pb$ apparent age, interpreted here as an inheritance.

The ~2.74 Ga age has never been reported in the Bacajá domain (see Fig. 2.14), implying that some previously unknown Neoarchean components may be present in this domain. The ~2.5 Ga age is not yet related to any metamorphic event described until now in the studied area. Still, it is associated with local magmatism in the northern sector of the Bacajá and as a magmatic inheritance in orogenic granitoids (Fig. 2.14, Besser and Barros, 2015; Vasquez and Rosa-Costa, 2008). Also, the age of 2.5 Ga represents restricted magmatism and amphibolite metamorphism in the north Carajás Domain (Machado et al., 1991; Salgado et al., 2019), which is rather close to the study area (Fig. 2.1c). Therefore, this age in our samples is still an open question, but likely result of Pb lost event.

The spatial relation between Novolândia mafic and felsic granulites indicates that their respective protoliths were affected simultaneously by granulite-facies metamorphism. However, while zircon grains from felsic granulites display clear preserved magmatic cores and metamorphic rims, two possibilities arise when evaluating the geochronological data of mafic granulite and amphibolite (samples ASM13, ASM34B). The first hypothesis, favored for our dated samples, is that mafic granulite and amphibolite protoliths were crystallized at ~2.08 Ga and ~2.03 Ga, respectively, with a short period between the igneous and metamorphic processes, which is common in granulite belts (e.g., Klaver et al., 2016, 2015). Another possibility is that the mafic rocks had their magmatic data entirely overprinted during metamorphism, which is not unusual for mafic rocks that underwent granulite metamorphism due to the small size of zircon that facilitates the diffusional resetting (Moser et al., 2017). However, given the size of zircon grains, their prismatic shapes, and some portions that resemble parallel zoning, typical of mafic rocks (Fig. 2.11, Corfu et al 2003) we consider that the ~2.08 Ga and 2.03 Ga as protolith crystallizations ages.

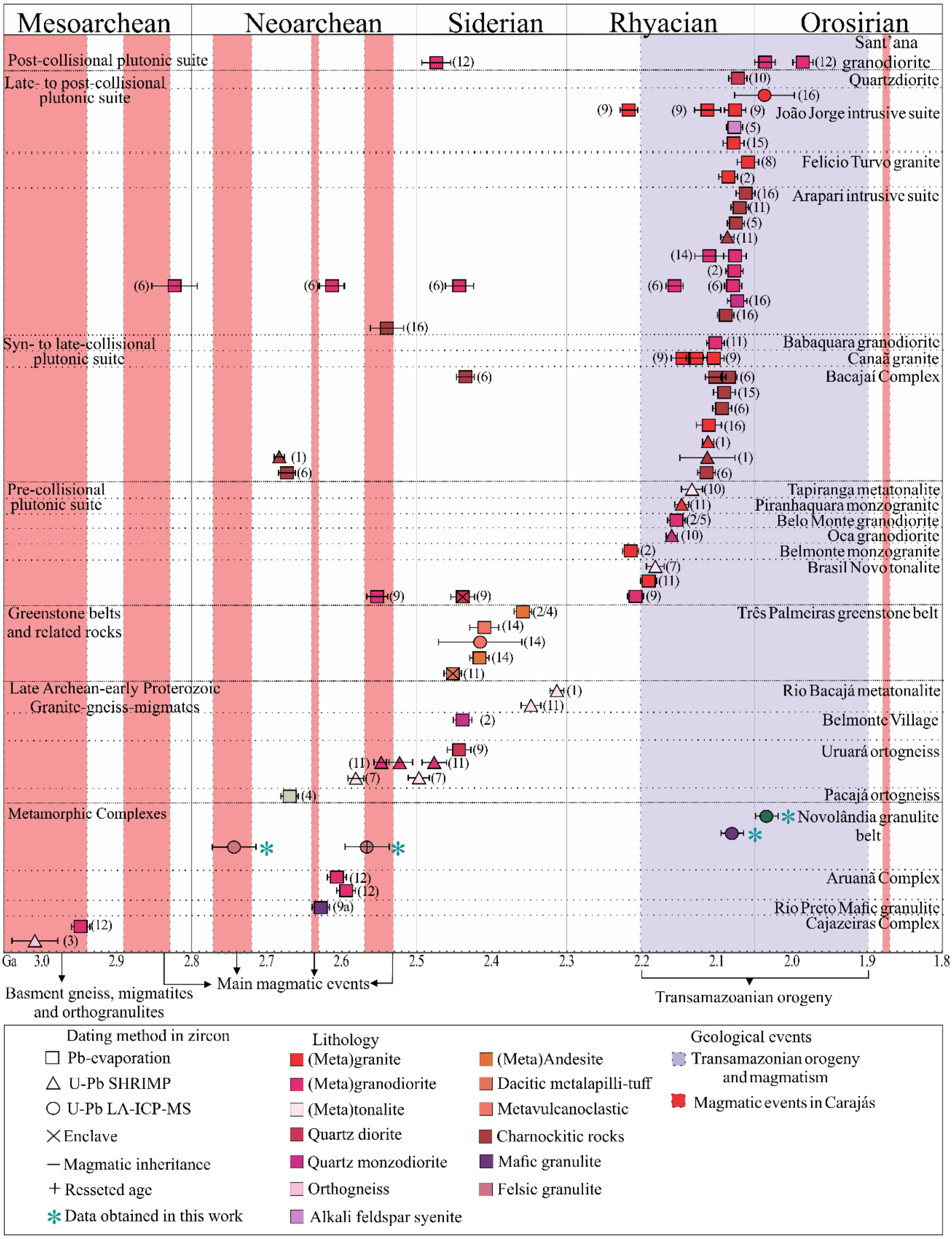

Figure 2.14 Summary all crystallization ages from Bacajá domain. Data is sourced from: 1 - Faraco et al., (2006), 2- Macambira et al., (2009), 3 - Macambira et al., (2007), 4 - Macambira et al., (2004), 5 - Macambira et al., (2003), 6 - Monteiro, (2006), 7 - Santos, (2003), 8 – Souza et al., (2003), 9 - Vasquez et al., (2005), 10- Vasquez (2006), 11 - Vasquez et al., (2008), 12 - Vasquez and Rosa-Costa (2008), 13- Barros et al., (2007), 14 - Cristo (2018), 15 - Macambira and Ricci (2015), 16 - Besser and Barros (2015). For detailed data see supplementary material 5.

9.2.3 Timing and duration of UHT metamorphism

Determining the age and duration of high to ultra-high temperature metamorphism is a challenging task, owing to the numerous mechanisms that may lead to the formation and later modification of zircon throughout metamorphic and partial melting processes (e.g., Harley et al., 2007; Taylor et al., 2016). Thus, to use and interpret age data, it is crucial to understand the process that controls these mineral's behavior in (U)HT settings. By doing so, it is possible to determine what events they may record in their ages.

The metamorphic zircon from the Novolândia belt yielded ages of 2106 ± 5 Ma (felsic granulite) and 2076 ± 11 Ma (aluminous granulite). These ages are interpreted to represent the time of the final cooling to the solidus. This interpretation is supported by the following evidence: (i) neoblastic grains and overgrowths display typical pattern of zircon grown in melt-bearing assemblages (Corfu et al., 2003; Taylor et al., 2016), (ii) phase equilibria modeling in the ZrO_2-bearing system suggests that newly grown zircon in anatectic rocks generally records the age of melt crystallization during cooling (e.g., Taylor et al., 2016 and references therein). The age of 1921 ± 16 Ma in the mafic granulite is interpreted probably as a later metamorphic event in the area, or even as a same event with long-duration.

The metamorphic ages available in the Bacajá domain occur in a relative restrict time interval of ca. 2.15-2.03 Ga (Fig. 2.15, Macambira et al., 2007, 2006; Monteiro, 2006; Vasquez and Rosa-Costa, 2008), with only local outliers (ca. 2.2 Ga, Vasquez, 2006, ca. 1.92 Ga, this work). Assuming that zircon in UHT rocks can register complex set of ages at or near peak conditions and also in post-peak stages (Harley, 2016; Harley et al., 2007; Kelsey and Hand, 2015; Taylor et al., 2016), it seems that at least some portions of the Bacajá domain experienced long-lived metamorphism. In the east sector of the Bacajá domain, Corrêa (2020) based on EPMA dating suggested a protracted monazite growth lasting more than 200 Ma, which supports a long-lived history for the Bacajá. The long-lasting metamorphism is also supported by a broad span of apparent $^{207}Pb/^{206}Pb$ metamorphic ages obtained in our samples from 2111 to 2049 Ma (Supplementary material 4).

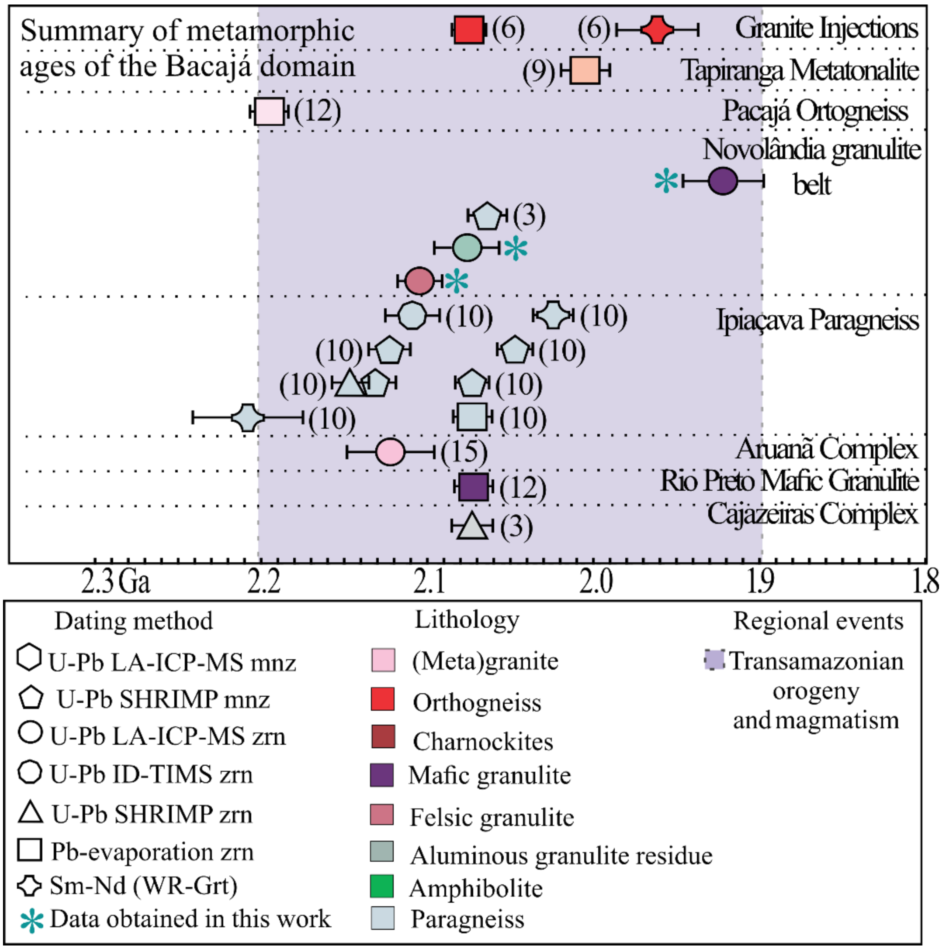

Figure 2.15 Summary of metamorphic ages in the Bacajá domain (references same as Fig. 15, supplementary material 5).

9.3 WHAT DROVE THE UHT METAMORPHISM?

UHT metamorphism has been suggested to be coeval with supercontinent assembly (e.g., Bozhko, 2018; Brown, 2007; Brown and Johnson, 2018). There are several tectonic and magmatic-driven models proposed for the generation of UHT metamorphism, which include: long-lived large hot collisional orogens (Harley, 2016; Jamieson and Beaumont, 2011), accretionary ultra-hot orogens (Chardon et al., 2009; Perchuk et al., 2018), conductive heating of over thickened orogens (Clark et al., 2011; Kelsey and Hand, 2015), heat advection from the sub-lithospheric mantle in thin lithospheres, such as delamination and asthenosphere upwelling (Gorczyk et al., 2015; Perchuk et al., 2018; Ueda et al., 2012), and by inversion and thickening of hot back-arc setting after slab break-off (Brown, 2007; Sizova et al., 2014; Thompson et al., 2001).

In the Bacajá domain, there is not yet a consistent model for (U)HT metamorphism. Several authors consider this domain as a collisional orogen (e.g., Barros et al., 2007; Macambira et al., 2009; Tavares et al., 2018; Rosa-Costa, 2008), although recent work suggests that the southern part of Bacajá represents an exhumed crust of the Archean Carajás domain (Motta et al., 2019).

We envisage a long-lived large hot collisional orogen for the evolution of the Bacajá domain and the heat source for UHT conditions, supported by the following pieces of evidence: (i) long-lasting metamorphism suggested for the Bacajá domain based on our data and on previous studies (see section 9.2.3 and Fig. 2.15); (ii) the maintenance of suprasolidus conditions above at least ~700 ºC for more than 30 million years that is common in such settings (e.g., Turlin et al., 2018); and (iii) the clockwise *P-T* path determined in our work with decompression-cooling, followed by isobaric cooling are similar with typical hot orogens (e.g., Harley, 2016, his figure 13). Also, the extensive orogenic juvenile magmatism widespread in the Bacajá domain (e.g., Macambira et al., 2009) and the possible short magmatic and granulite metamorphism history in mafic granulites in the study area could have enhanced UHT conditions (Guo et al., 2012; Klaver et al., 2016).

A large hot orogen setting for the Bacajá domain, if correct, suggests a complex evolution. In this scenario, the deep crust formed from considerably older continental materials (see section 7) and was left trapped for long periods under an orogenic plateau, undergoing prolonged heating (Clark et al., 2011). The cooling followed the cessation of orogeny, which age is consistent with the cooling ages of ca. 2.0-1.9 Ga obtained in the Bacajá domain (Perico et al., 2017; Tavares, 2015).

9.4 UHT GRANULITES BELTS WITHIN PALEOPROTEROZOIC TRANSAMAZONIAN-BIRIMIAN OROGENS AND TECTONIC IMPLICATIONS FOR COLUMBIA ASSEMBLY

Most of the paleogeographic reconstructions place the ca. 2.20–2.05 Ga crust in the Maroní-Itacaiunas Province as the southern continuation of the Birimian crust in the West Africa Craton (e.g., D’Agrella-Filho et al., 2016). This fit is also supported by largely overlapping geological history between the two regions, where the sinistral shear zones in the Amazonian Craton are inferred to be related to sinistral shear zones in the Birimian Orogen of the south West Africa Craton (Kroonenberg et al., 2016). Thus, we will compare the previously reported UHT localities within these orogens to our new recent discovery.

In the Bakhuis Granulite Belt (Fig. 2.1b), in Suriname, Klaver et al. (2015, and references therein) reported two separate UHT metamorphism events driven by different mechanisms. According to these authors, at 2.05-2.07 Ga, asthenospheric upwelling due to the development of a slab tear in the subducted West Africa slab (Amapá-West Africa assembly) provides the heat necessary for UHT metamorphism. In contrast, at ~1.99 Ga, UHT charnockites were driven by voluminous hot mafic magma intruded into the lower crust in a subduction environment developed during a late Paleoproterozoic orogeny phase (Klaver et al., 2015).

In the Birimian Orogen, West Africa Craton (Fig 2.1b), granulite-facies rocks are restricted to the Archean KénémaMan block (Grenholm et al., 2019, and references therein). The transition from peak to retrograde conditions occurred at 2.03-2.05 Ga (Cocherie et al., 1998; Kouamelan et al., 1997). The (U)HT-HP conditions developed due to crustal thickening through tectonic stacking (Triboulet and Feybesse, 1998).

All UHT localities in the Transamazonian-Birimian orogens share similar Rhyacian ages, but different driving mechanisms are proposed for the Bakhuis belt, Birimian orogen and the one presented here. However, all localities' evolution is closely related to the Amazonian-West Africa cratons assembly during Columbia amalgamation (Meert and Santosh, 2017; Zhao et al., 2002). Up to this point, there are only three localities that report UHT conditions in the Transamazonian-Birimian orogens in Bakhuis Belt (e.g., Klaver et al., 2015), KénémaMan block (Triboulet and Feybesse, 1998) and in South Bacajá Domain (this work). The significant absence of these metamorphic conditions, if compared with other belts developed during the Columbia assembly, like the Khondalite Belt in the North China Craton (e.g., Santosh et al., 2012) and Salvador-Itabuna-Curaça belt, São Franscico Craton (e.g., Barbosa et al., 2017), could be due to the lack of studies of metamorphic conditions within these belts, or that peak assemblages were obliterated during retrogression. Alternatively, according to the compilation presented by Kelsey and Hand (2015), only a minor part of reported peaks of UHT conditions were attained during the Paleoproterozoic because the thermal gradients of high dT/dP metamorphism rose to a maximum during the Mesoproterozoic due to the insulation of the mantle beneath Columbia (Brown and Johnson, 2018).

In different Maroní-Itacaiúnas Province regions, distinct driving mechanisms were proposed to triggering metamorphism, but an orogenic setting, either collisional or accretionary, is typical of every proposal. The data presented here and the other studies in the Maroní-Itacaiúnas Province suggest a complex and coeval evolution for the granulite belts during the late Rhyacian to early Orosirian, with multiple HT events (Tassinari et al., 2004) and local UHT conditions (Klaver et al., 2015; Nanne et al., 2020; Roever et al., 2003), driven by different mechanisms during the assembly of the West Africa and Amazonian Cratons.

The metamorphic ages between ca. 2.10-2.07 Ga obtained in this work also suggest a coeval metamorphic evolution in all granulite-gneiss belts within the Maroní-Itacaiúnas Province. Owing that all late Rhyacian granulite-belts in that province (Fig. 2.1b) record similar metamorphic ages that overlap within errors, at 2.05 to 1.98 Ga in the Imataca Block (Tassinari et al., 2004), 2.07 to 2.05 Ga in the Bakhuis belt (Klaver et al., 2015; Roever et al., 2003), 2.09 to 2.08 Ga and 2.05 Ga in the southeastern Amapá block (Rosa-Costa et al., 2008). In the western portion of Bacajá, the granulite metamorphism dates from 2.14 to 2.05 Ga (Vasquez, 2006). Also, the metamorphism in the Bacajá domain is closely related to the orogenic magmatism summarized by Vasquez and Rosa-Costa (2008), with overlapping ages, which support contemporaneous magmatism and metamorphism that is a common feature in hot orogens (e.g., Slagstad et al., 2018).

10 CONCLUSIONS

Taking into account field aspects and relationships, the metamorphic and thermobarometric constraints and the geochronological results, our data point out that in the Novolândia granulite belt, Bacajá domain, Amazonian craton:

(i) The granulite residue from aluminous migmatites records the first occurrence of UHT metamorphism in the Bacajá domain. The UHT metamorphism experienced a clockwise *P-T* path. Peak UHT conditions were followed by decompression-cooling and later isobaric cooling.

(ii) With maximum deposition age of 2.6 Ga, a sedimentary system received up to 3.3 Ga old detrital material, whose sources were probably Bacajá and Carajás basements.

(iii) Felsic granulites were crystallized at ca. 2.74 Ga and record a resetting/Pb lost event around ca. 2.56 Ga. In turn, mafic granulites and amphibolites were crystallized at ca. 2.08 and 2.03 Ga, respectively.

(iv) The metamorphic data in the whole Bacajá domain suggest that at least some areas underwent long-lived granulite metamorphism between ca. 2.15 and 2.03 Ga.

(v) A large, long-lived hot collisional orogen setting triggered UHT conditions and was probably enhanced by coeval extensive juvenile and local mafic magmatism.

(vi) The Transamazonian-Birimian orogens share similar metamorphic ages, but different mechanisms drove (U)HT conditions. However, all settings are linked to the Amazonian-West Africa Cratons assembly during the build-up of Columbia.

ACKNOWLEDGMENTS

The Research Group on Mineralogy and Petrology (Unifesspa) and students from Unifesspa (years 2009 to 2013) are acknowledged for previous work in the studied area. Thanks to F.A. Oliveira for assistance during fieldwork. J. R. Oliveira is acknowledged for support in sample preparation, LA-ICP-MS analysis and great discussions about granulites. P.V.F.S Alves and N.F. Botelho are thanked for their assistance in EPMA analyses. The original paper was greatly enhanced after fruitful discussions with R. Moraes and M.E. Schutesky. The authors acknowledge the support of the INCT Estudos Tectônicos (CAPES/CNPq- 465613/2014-4 and FAP-DF-193.001.263/2017). This study was financed in part by the Coordenação de Aperfeiçoamento de Pessoal de Nível Superior - Brasil (CAPES) - Finance Code 001 (A. S. Silva - CAPES scholarship).

REFERENCES

Almeida, F.F.M., Hasui, Y., De Brito Neves, B.B., Fuck, R.A., 1981. Brazilian structural provinces: an introduction. Earth-Science Rev. 17, 1–29.

Andersen, T., 2005. Detrital zircons as tracers of sedimentary provenance: Limiting conditions from statistics and numerical simulation. Chem. Geol. 216, 249–270. https://doi.org/10.1016/j.chemgeo.2004.11.013

Barbosa, J.S.F., Leal, A.B.D.M., Fuck, R.A., De Oliveira, J.S.D.S., Gonçalves, P., Leite, C.D.M.M., 2017. Ultrahigh-temperature metamorphism of 2.0 Ga-Old sapphirine-bearing granulite from the Itabuna-Salvador-Curaçá Block, Bahia, Brazil. Geol. USP - Ser. Cient. 17, 89–108. https://doi.org/10.11606/issn.2316-9095.v17-287

Barros, C.E. de M., Macambira, M.J.B., Santos, M.C. da C., Silva, D.C.C., Palmeira, L.C.M., Sousa, M.M., 2007. Estruturas sinmagmáticas e idade de zircão de granitos (evaporação de Pb) paleoproterozóicos da parte leste do domínio Bacajá, Província Maroni-Itacaiúnas. Rev. Bras. Geociências 37, 293–304. https://doi.org/10.25249/0375-7536.2007373293304

Besser, M.L., Barros, C.E.M., 2015. Geologia e recursos minerais da Folha Rio Bacajá - SA.22-Y-D-VI, Estado do Pará. CPRM, Belém.

Bhowmik, S.K., Alexanderwilde, S., Bhandari, A., Sarbadhikari, A.B., 2014. Zoned monazite and zircon as monitors for the thermal history of granuliteterranes: An example from the Central Indian Tectonic Zone. J. Petrol. 55, 585–621. https://doi.org/10.1093/petrology/egt078

Biswal, T.K., Sinha, S., 2003. Deformation history of the NW salient of the Eastern Ghats Mobile Belt, India. J. Asian Earth Sci. 22, 157–169. https://doi.org/10.1016/S1367-9120(02)00182-7

Bozhko, N.A., 2018. Granulite Gneiss Belts: The Geodynamic Aspect. Moscow Univ. Geol. Bull. 73, 407–415. https://doi.org/10.3103/S0145875218050046

Brito Neves, B.B., 2011. The Paleoproterozoic in the South-American continent: Diversity in the geologic time. J. South Am. Earth Sci. 32, 270–286. https://doi.org/10.1016/j.jsames.2011.02.004

Brown, M., 2009. Metamorphic patterns in orogenic systems and the geological record. Geol. Soc. Spec. Publ. 318, 37–74. https://doi.org/10.1144/SP318.2

Brown, M., 2007. Metamorphic conditions in orogenic belts: A record of secular change. Int. Geol. Rev. 49, 193–234. https://doi.org/10.2747/0020-6814.49.3.193

Brown, M., Johnson, T., 2018. Secular change in metamorphism and the onset of global plate tectonics. Am. Mineral. 103, 181–196. https://doi.org/10.2138/am-2018-6166

Bühn, B., Pimentel, M.M., Matteini, M., Dantas, E.L., 2009. High spatial resolution analysis of Pb and U isotopes for geochronology by laser ablation multi-collector inductively coupled plasma mass spectrometry (LA-MC-ICP-MS). An. Acad. Bras. Cienc. 81, 99–114. https://doi.org/10.1590/s0001-37652009000100011

Chardon, D., Gapais, D., Cagnard, F., 2009. Flow of ultra-hot orogens: A view from the Precambrian, clues for the Phanerozoic. Tectonophysics 477, 105–118. https://doi.org/10.1016/j.tecto.2009.03.008

Clark, C., Fitzsimons, I.C.W., Healy, D., Harley, S.L., 2011. How does the continental crust get really hot? Elements 7, 235–240. https://doi.org/10.2113/gselements.7.4.235

Cocherie, A., Legendre, O., Peucat, J.J., Kouamelan, A.N., 1998. Geochronology of polygenetic monazites constrained by in situ electron microprobe Th-U-total lead determination: Implications for lead behaviour in monazite. Geochim. Cosmochim. Acta 62, 2475–2497. https://doi.org/10.1016/S0016-7037(98)00171-9

Coggon, R., Holland, T.J.B., 2002. Mixing properties of phengitic micas and revised garnet-phengite thermobarometers. J. Metamorph. Geol. 20, 683–696. https://doi.org/10.1046/j.1525-1314.2002.00395.x

Cordani, U.G., Sato, K., Teixeira, W., Tassinari, C.G., Basei, M.A.S., 2000. Crustal evolution of the South American Platform. Tecton. Evol. South Am. 19–40.

Corfu, F., Hanchar, J.M., Hoskin, P.W.O., Kinny, P., 2003. Atlas of zircon textures. Rev. Mineral. Geochemistry 53. https://doi.org/10.2113/0530469

Corrêa, L.S., 2020. Petrochronology of paragneisses of Bacajá Domain, Amazon Craton. Universidade de Campinas.

Cristo, L.C.F., 2018. Estudo petrográfico e isotópico (Pb-Pb, U-Pb e Sm-Nd) de rochas metavulcânicas, mineralizações auríferas e rochas granitoides relacionadas ao greenstone belt Três Palmeiras, Volta Grande do Xingu, Domínio Bacajá. Universidade Federal do Pará.

Cutts, K.A., Kelsey, D.E., Hand, M., 2013. Evidence for late Paleoproterozoic (ca 1690-1665Ma) high- to ultrahigh-temperature metamorphism in southern Australia: Implications for Proterozoic supercontinent models. Gondwana Res. 23, 617–640. https://doi.org/10.1016/j.gr.2012.04.009

D’Agrella-Filho, M.S., Bispo-Santos, F., Trindade, R.I.F., Antonio, P.Y.J., 2016. Paleomagnetism of the Amazonian Craton and its role in paleocontinents. Brazilian J. Geol. 46, 275–299. https://doi.org/10.1590/2317-4889201620160055

da Rosa-Costa, L.T., Lafon, J.M., Delor, C., 2006. Zircon geochronology and Sm-Nd isotopic study: Further constraints for the Archean and Paleoproterozoic geodynamical evolution of the southeastern Guiana Shield, north of Amazonian Craton, Brazil. Gondwana Res. 10, 277–300. https://doi.org/10.1016/j.gr.2006.02.012

De Capitani, C., Petrakakis, K., 2010. The computation of equilibrium assemblage diagrams with Theriak/Domino software. Am. Mineral. 95, 1006–1016. https://doi.org/10.2138/am.2010.3354

Dunkley, D.J., Suzuki, K., Hokada, T., Kusiak, M.A., 2008. Contrasting ages between isotopic chronometers in granulites: monazite dating and metamorphism in the Higo Complex, Japan. Gondwana Res. 14, 624–643.

https://doi.org/10.1016/j.gr.2008.02.003

Faraco, M.T.L., Vale, A.G., Santos, J.O.S., Luzardo, R., Ferreira, A. l., Oliveira, M.A., Marinho, P.A.C., 2006. Levantamento geológico da região ao norte da Província Carajás in: Souza, in: Souza, Valmir; Horbe, A.C. (Ed.), Contribuições a Geologia Da Amazônia. Sociedade Brasileira de Geologia, Belém, pp. 32–44.

Feio, G.R.L., Dall'Agnol, R., Dantas, E.L., Macambira, M.J.B., Santos, J.O.S., Althoff, F.J., Soares, J.E.B., 2013. Archean granitoid magmatism in the Canaã dos Carajás area: Implications for crustal evolution of the Carajás province, Amazonian craton, Brazil. Precambrian Res. 227, 157–185. https://doi.org/10.1016/j.precamres.2012.04.007

Feio, G.R.L., Sousa, J.T., Almeida, J.A.C., 2016. Geotermobarometria de granulitos do Complexo Novolândia, porção sul do Domínio Bacajá, Província Tranzamazonas, in: 48º Congresso Brasileiro de Geolgia. Sociedade Brasileira de Geologia, Porto Alegre.

Florence, F.P., Spear, F.S., 1991. Effects of diffusional modification of garnet growth zoning on P-T path calculations. Contrib. to Mineral. Petrol. 107, 487–500. https://doi.org/10.1007/BF00310683

Fraga, L.M., Reis, N.J., Agnol, R.D., 2008. Cauarane - Coeroeni Belt – the Main Tectonic Feature of the Central Guyana Shield , Northern Amazonian Craton. Unknown 2–5.

Gerdes, A., Zeh, A., 2009. Zircon formation versus zircon alteration - New insights from combined U-Pb and Lu-Hf in-situ LA-ICP-MS analyses, and consequences for the interpretation of Archean zircon from the Central Zone of the Limpopo Belt. Chem. Geol. 261, 230–243. https://doi.org/10.1016/j.chemgeo.2008.03.005

Gorczyk, W., Smithies, H., Korhonen, F., Howard, H., Quentin De Gromard, R., 2015. Ultra-hot Mesoproterozoic evolution of intracontinental central Australia. Geosci. Front. 6, 23–37. https://doi.org/10.1016/j.gsf.2014.03.001

Grenholm, M., Jessell, M., Thébaud, N., 2019. A geodynamic model for the Paleoproterozoic (ca. 2.27–1.96 Ga) Birimian Orogen of the southern West African Craton – Insights into an evolving accretionary-collisional orogenic system. Earth-Science Rev. 192, 138–193. https://doi.org/10.1016/j.earscirev.2019.02.006

Groppo, C., Rolfo, F., Indares, A., 2012. Partial melting in the higher Himalayan crystallines of Eastern Nepal: The effect of decompression and implications for the "channel flow" model. J. Petrol. 53, 1057–1088. https://doi.org/10.1093/petrology/egs009

Groppo, C., Rubatto, D., Rolfo, F., Lombardo, B., 2010. Early Oligocene partial melting in the Main Central Thrust Zone (Arun valley, eastern Nepal Himalaya). Lithos 118, 287–301. https://doi.org/10.1016/j.lithos.2010.05.003

Guo, J.H., Peng, P., Chen, Y., Jiao, S.J., Windley, B.F., 2012. UHT sapphirine granulite metamorphism at 1.93-1.92Ga caused by gabbronorite intrusions: Implications for tectonic evolution of the northern margin of the North China Craton. Precambrian Res. 222–223, 124–142. https://doi.org/10.1016/j.precamres.2011.07.020

Harley, S.L., 2016. A matter of time: The importance of the duration of UHT metamorphism. J. Mineral. Petrol. Sci. 111, 50–72. https://doi.org/10.2465/jmps.160128

Harley, S.L., 2008. Refining the P-T records of UHT crustal metamorphism. J. Metamorph. Geol. 26, 125–154. https://doi.org/10.1111/j.1525-1314.2008.00765.x

Harley, S.L., 1998. On the occurrence and characterization of ultrahigh-temperature crustal metamorphism. Geol. Soc. Spec. Publ. 138, 81–107. https://doi.org/10.1144/GSL.SP.1996.138.01.06

Harley, S.L., Kelly, N.M., Möller, A., 2007. Zircon behaviour and the thermal histories of moutain chains. Elements 3, 25–30. https://doi.org/10.2113/gselements.3.1.25

Holland, T., Powell, R., 2003. Activity-compositions relations for phases in petrological calculations: An asymetric multicomponent formulation. Contrib. to Mineral. Petrol. 145, 492–501. https://doi.org/10.1007/s00410-003-0464-z

Holland, T.J.B., Powell, R., 1998. An internally consistent thermodynamic data set for phases of petrological interest. J. Metamorph. Geol. 16, 309–344.

Hurley, P.., Almeida, F.F.., Melcher, G.., Cordani, U.., Rand, J., Kawashita, K., Vandoros, P., Pinson, W.., Fairbairn, H.., 1967. Test of continental drift by means of radiometric ages. Science (80-.). 495–500.

Indares, A., White, R.W., Powell, R., 2008. Phase equilibria modelling of kyanite-bearing anatectic paragneisses from the central Grenville Province. J. Metamorph. Geol. 26, 815–836. https://doi.org/10.1111/j.1525-1314.2008.00788.x

Jackson, S.E., Pearson, N.J., Griffin, W.L., Belousova, E.A., 2004. The application of laser ablation-inductively coupled plasma-mass spectrometry to in situ U-Pb zircon geochronology. Chem. Geol. 211, 47–69. https://doi.org/10.1016/j.chemgeo.2004.06.017

Jamieson, R.A., Beaumont, C., 2011. Coeval thrusting and extension during lower crustal ductile flow - implications for exhumation of high-grade metamorphic rocks. J.

Metamorph. Geol. 29, 33–51. https://doi.org/10.1111/j.1525-1314.2010.00908.x

Jiao, S., Guo, J., 2020. Paleoproterozoic UHT metamorphism with isobaric cooling (IBC) followed by decompression–heating in the Khondalite Belt (North China Craton): New evidence from two sapphirine formation processes. J. Metamorph. Geol. 38, 357–378. https://doi.org/10.1111/jmg.12525

Kawasaki, T., Motoyoshi, Y., 2016. Ti-in-garnet thermometer for ultrahigh-temperature granulites. J. Mineral. Petrol. Sci. 111, 226–240. https://doi.org/10.2465/jmps.150709

Kelsey, D.E., Hand, M., 2015. On ultrahigh temperature crustal metamorphism: Phase equilibria, trace element thermometry, bulk composition, heat sources, timescales and tectonic settings. Geosci. Front. 6, 311–356. https://doi.org/10.1016/j.gsf.2014.09.006

Kelsey, D.E., White, R.W., Powell, R., Wilson, C.J.L., Quinn, C.D., 2003. New constraints on metamorphism in the Rauer Group, Prydz Bay, east Antarctica. J. Metamorph. Geol. 21, 739–759. https://doi.org/10.1046/j.1525-1314.2003.00476.x

Klaver, M., de Roever, E.W.F., Nanne, J.A.M., Mason, P.R.D., Davies, G.R., 2015. Charnockites and UHT metamorphism in the Bakhuis Granulite Belt, western Suriname: Evidence for two separate UHT events. Precambrian Res. 262, 1–19. https://doi.org/10.1016/j.precamres.2015.02.014

Klaver, M., de Roever, E.W.F., Thijssen, A.C.D., Bleeker, W., Söderlund, U., Chamberlain, K., Ernst, R., Berndt, J., Zeh, A., 2016. Mafic magmatism in the Bakhuis Granulite Belt (western Suriname): relationship with charnockite magmatism and UHT metamorphism. Gff 138, 203–218. https://doi.org/10.1080/11035897.2015.1061591

Korhonen, F.J., Powell, R., Stout, J.H., 2012. Stability of sapphirine + quartz in the oxidized rocks of the Wilson Lake terrane, Labrador: Calculated equilibria in NCKFMASHTO. J. Metamorph. Geol. 30, 21–36. https://doi.org/10.1111/j.1525-1314.2011.00954.x

Kouamelan, A.N., Delor, C., Peucat, J.J., 1997. Geochronological evidence for reworking of Archean terrains during the Early Proterozoic (2.1 Ga) in the western Côte d’Ivoire (Man Rise - West African Craton). Precambrian Res. 86, 177–199. https://doi.org/10.1016/s0301-9268(97)00043-0

Kroonenberg, S.B., De Roever, E.W.F., Fraga, L.M., Reis, N.J., Faraco, T., Lafon, J.M., Cordani, U., Wong, T.E., 2016. Paleoproterozoic evolution of the Guiana Shield in

Suriname: A revised model. Geol. en Mijnbouw/Netherlands J. Geosci. 95, 491–522. https://doi.org/10.1017/njg.2016.10

Lebedeva, Y.M., Glebovitskii, V.A., Bushmin, S.A., Bogomolov, E.S., Savva, E. V., Lokhov, K.I., 2010. The age of high-pressure metasomatism in shear zones during collision-related metamorphism in the Lapland granulite belt: The Sm-Nd method of dating the paragenesises from sillimanite-orthopyroxene rocks of Por'ya Guba nappe. Dokl. Earth Sci. 432, 602–605. https://doi.org/10.1134/S1028334X10050119

Leite, C. de M.M., Barbosa, J.S.F., Goncalves, P., Nicollet, C., Sabaté, P., 2009. Petrological evolution of silica-undersaturated sapphirine-bearing granulite in the Paleoproterozoic Salvador-Curaçá Belt, Bahia, Brazil. Gondwana Res. 15, 49–70. https://doi.org/10.1016/j.gr.2008.06.005

Liu, H., Li, X.P., Kong, F.M., Santosh, M., Wang, H., 2019. Ultra-high temperature overprinting of high pressure pelitic granulites in the Huai'an complex, North China Craton: Evidence from thermodynamic modeling and isotope geochronology. Gondwana Res. 72, 15–33. https://doi.org/10.1016/j.gr.2019.02.003

Liu, T., Wei, C., 2020. Metamorphic P–T paths and Zircon U–Pb ages of Archean ultra-high temperature paragneisses from the Qian'an gneiss dome, East Hebei terrane, North China Craton. J. Metamorph. Geol. 38, 329–356. https://doi.org/10.1111/jmg.12524

Macambira, E.M.B., Ricci, P.S.F., 2015. Geologia e recursos minerais da Folha Tucuruí – SA.22-Z-C, Estado do Pará, 1st ed. CPRM, Belém.

Macambira, M.J.B., Armstrong, R.A., Silva, D.C.C., Camelo, J.F., 2006. The Archean-Paleoproterozoic boundary in Amazonian craton: New isotope evidence for crustal growth, in: Geochimica et Cosmochimica Acta. p. A380. https://doi.org/10.1016/j.gca.2006.06.768

Macambira, M.J.B., Pinheiro, V.L., Armstrong, R.A., 2007. A fronteira Arqueano-Paleoproterozoico no SE do Cráton Amazônico: abrupta no tempo, suave na tectônica?, in: X Simpósio de Geologia Da Amazônia. pp. 97–100.

Macambira, M.J.B., Silva, D.C.C., Barros, C.E.M., Scheller, T., 2003. New isotope evidences confirming the existence of a paleoproterozoic terrain in the region at the north of the Carajas Mineral Province, in: IV South American Symposium on Isotope Geology. Salvadaro, Brazil, pp. 205–206.

Macambira, M.J.B., Silva, D.C.C., Vasquez, M.L., Barros, C.E.M., 2004. Investigação do limite Arqueano-Paleoproterozoico ao norte da Província Carajás, Amazônia

Oriental, in: 42º Congresso Brasileiro de Geologia. Araxá.

Macambira, M.J.B., Vasquez, M.L., Silva, D.C.C., Galarza, M.A., Barros, C.E.M., Camelo, J.F., 2009. Crustal growth of the central-eastern Paleoproterozoic domain, SW Amazonian craton: Juvenile accretion vs. reworking. J. South Am. Earth Sci. 27, 235–246. https://doi.org/10.1016/j.jsames.2009.02.001

Machado, N., Lindenmayer, Z., Krogh, T.E., Lindenmayer, D., 1991. U-Pb geochronology of Archean magmatism and basement reactivation in the Carajás area, Amazon shield, Brazil. Precambrian Res. 49, 329–354. https://doi.org/10.1016/0301-9268(91)90040-H

Meert, J.G., Santosh, M., 2017. The Columbia supercontinent revisited. Gondwana Res. 50, 67–83. https://doi.org/10.1016/j.gr.2017.04.011

Melo, G.H.C., Monteiro, L.V.S., Xavier, R.P., Moreto, C.P.N., Santiago, E.S.B., Dufrane, S.A., Aires, B., Santos, A.F.F., 2017. Temporal evolution of the giant Salobo IOCG deposit, Carajás Province (Brazil): constraints from paragenesis of hydrothermal alteration and U-Pb geochronology. Miner. Depos. 52, 709–732. https://doi.org/10.1007/s00126-016-0693-5

Milhomem Neto, J.M., Lafon, J.M., 2019. Zircon U-Pb and Lu-Hf isotope constraints on Archean crustal evolution in Southeastern Guyana Shield. Geosci. Front. 10, 1477–1506. https://doi.org/10.1016/j.gsf.2018.09.012

Monteiro, P.C., 2006. Investigação do limite entre os domínios geocronológicos da região do Médio Xingu, Sudeste do Cráton Amazônico. Universidade Federal do Pará.

Moser, D.E., Corfu, F., Darling, J.R., Reddy, S.M., Tait, K., 2017. Microstructural Geochronology: Planetary Records Down to Atom Scale.

Motta, J.G., Souza Filho, C.R. d., Carranza, E.J.M., Braitenberg, C., 2019. Archean crust and metallogenic zones in the Amazonian Craton sensed by satellite gravity data. Sci. Rep. 9. https://doi.org/10.1038/s41598-019-39171-9

Motta, R.G., Fitzsimons, I.C.W., Moraes, R., Johnson, T.E., Schuindt, S., Benetti, B.Y., 2021. Recovering P–T–t paths from ultra-high temperature (UHT) felsic orthogneiss: An example from the Southern Brasília Orogen, Brazil. Precambrian Res. 359. https://doi.org/10.1016/j.precamres.2021.106222

Nanne, J.A.M., De Roever, E.W.F., de Groot, K., Davies, G.R., Brouwer, F.M., 2020. Regional UHT metamorphism with widespread, primary CO2-rich cordierite in the Bakhuis Granulite Belt, Surinam: A feldspar thermometry study. Precambrian Res. 350. https://doi.org/10.1016/j.precamres.2020.105894

Nichols, G.T., Berry, R.F., Green, D.H., 1992. Internally consistent gahnitic spinel-cordierite-garnet equilibria in the FMASHZn system: geothermobarometry and applications. Contrib. to Mineral. Petrol. 111, 362–377. https://doi.org/10.1007/BF00311197

Ouzegane, K., Kienast, J.R., Bendaoud, A., Drareni, A., 2003. A review of Archaean and Paleoproterozoic evolution of the In Ouzzal granulitic terrane (Western Hoggar, Algeria). J. African Earth Sci. 37, 207–227. https://doi.org/10.1016/j.jafrearsci.2003.05.002

Paton, C., Hellstrom, J., Paul, B., Woodhead, J., Hergt, J., 2011. Iolite: Freeware for the visualisation and processing of mass spectrometric data. J. Anal. At. Spectrom. 26, 2508–2518. https://doi.org/10.1039/c1ja10172b

Pattison, D.R.M., Chacko, T., Farquhar, J., McFarlane, C.R.M., 2003. Temperatures of granulite-facies metamorphism: Constraints from experimental phase equilibria and thermobarometry corrected for retrograde exchange. J. Petrol. 44, 867–900. https://doi.org/10.1093/petrology/44.5.867

Perchuk, A.L., Safonov, O.G., Smit, C.A., van Reenen, D.D., Zakharov, V.S., Gerya, T. V., 2018. Precambrian ultra-hot orogenic factory: Making and reworking of continental crust. Tectonophysics 746, 572–586. https://doi.org/10.1016/j.tecto.2016.11.041

Perico, E., De Barros, C.E.M., Mancini, F., Rostirolla, S.P., 2017. Protracted deformation during cooling of the Paleoproterozoic arc system as constrained by 40Ar/39Ar ages of muscovite from brittle faults: The Transamazonan Bacajá Terrane, Brazil. Brazilian J. Geol. 47, 427–440. https://doi.org/10.1590/2317-4889201720170033

Petrus, J.A., Kamber, B.S., 2012. VizualAge: A Novel Approach to Laser Ablation ICP-MS U-Pb Geochronology Data Reduction. Geostand. Geoanalytical Res. 36, 247–270. https://doi.org/10.1111/j.1751-908X.2012.00158.x

Robertson, J.K., Wyllie, P.J., 1971. Experimental Studies on Rocks from the Deboullie Stock, Northern Maine, including Melting Relations in the Water-Deficient Environment. J. Geol. 79, 549–571. https://doi.org/10.1086/627675

Rocha, B.C., Moraes, R., Möller, A., Cioffi, C.R., 2018. Magmatic inheritance vs. UHT metamorphism: Zircon petrochronology of granulites and petrogenesis of charnockitic leucosomes of the Socorro–Guaxupé nappe, SE Brazil. Lithos 314–315, 16–39. https://doi.org/10.1016/j.lithos.2018.05.014

Rodrigues, D.L., Oliveira, J.S. de S. de, Moraes, R. de, 2020. Geotermobarometria de safirina e granada granulito do afloramento da Praia da Paciência, Salvador, Bahia – Cinturão Salvador-Esplanada-Boquim. Geol. USP. Série Científica 20, 53–78. https://doi.org/10.11606/issn.2316-9095.v20-171026

Roever, E.W.., Lafon, J., Delor, C., Cocherie, A., Rossi, P., Guerrot, C., Portel, A., 2003. The Bakhuis ultrahigh-temperature granulite belt (Suriname): I. petrological and geochronological evidence for a counterclockwise P-T path at 2.07-2.05 Ga. Géologie la Fr. 175–205.

Rosa-Costa, L.T., Lafon, J.M., Cocherie, A., Delor, C., 2008. Electron microprobe U-Th-Pb monazite dating of the Transamazonian metamorphic overprint on Archean rocks from the Amapá Block, southeastern Guiana Shield, Northern Brazil. J. South Am. Earth Sci. 26, 445–462. https://doi.org/10.1016/j.jsames.2008.05.007

Rosa-Costa, L.T., Ricci, P., Lafon, J., Vazquez, M.L., Carvalho, J., Klein, E., Macambira, E., 2003. Geology and geochronology of Archean and Paleoproterozoic domains of southwestern Amapa and northwestern Para, Brazil, southeastern Guiana shield. Géologie la Fr. 101–120.

Rubatto, D., 2017. Zircon: The Metamorphic Mineral. Rev. Mineral. Geochemistry 83, 261–295. https://doi.org/10.2138/rmg.2017.83.09

Salgado, S.S., de Andrade Caxito, F., Figueiredo e Silva, R.C., Lana, C., 2019. Provenance of the Buritirama Formation reveals the Paleoproterozoic assembly of the Bacajá and Carajás blocks (Amazon Craton) and the chronocorrelation of Mn-deposits in the Transamazonian/Birimian system of northern Brazil/West Africa. J. South Am. Earth Sci. 96. https://doi.org/10.1016/j.jsames.2019.102364

Sandiford, M., Powell, R., 1986. Deep crustal metamorphism during continental extension: modern and ancient examples. Earth Planet. Sci. Lett. 79, 151–158. https://doi.org/10.1016/0012-821X(86)90048-8

Santos, J.O.S., 2003. Geotectônica dos Escudos das Guianas e Brasil-Central, in: Bizzi, L.A., Schobbenhaus, C., Vidotti, R.M., Gonçalves, J.H. (Eds.), Geologia, Tectônica e Recursos Minerais Do Brasil. CPRM, Brasília, pp. 169–195.

Santos, J.O.S., Hartmann, L.A., Faria, M.S., Riker, S.R., Miguel, M., Almeida, M.E., Mcnaughton, N.J., 2006. a Compartimentação Do Cráton Amazonas Em Províncias : Avanços Ocorridos No Período 2000-2006, in: IX Simpósio de Geologia Da Amazônica. Sociedade Brasileira de Geologia, Belém.

Santosh, M., Liu, S.J., Tsunogae, T., Li, J.H., 2012. Paleoproterozoic ultrahigh-temperature granulites in the North China Craton: Implications for tectonic models on extreme crustal metamorphism. Precambrian Res. 222–223, 77–106. https://doi.org/10.1016/j.precamres.2011.05.003

Sawyer, E.W., 2008. Atlas of migmatites, Special pu. ed. Canadia Mineralogist.

Sawyer, E.W., 1999. Criteria for the recognition of partial melting. Phys. Chem. Earth, Part A Solid Earth Geod. 24, 269–279. https://doi.org/10.1016/S1464-1895(99)00029-0

Sizova, E., Gerya, T., Brown, M., 2014. Contrasting styles of Phanerozoic and Precambrian continental collision. Gondwana Res. 25, 522–545. https://doi.org/10.1016/j.gr.2012.12.011

Slagstad, T., Roberts, N.M.W., Coint, N., Høy, I., Sauer, S., Kirkland, C.L., Marker, M., Røhr, T.S., Henderson, I.H.C., Stormoen, M.A., Skår, Ø., Sørensen, B.E., Bybee, G., 2018. Magma-driven, high-grade metamorphism in the Sveconorwegian Province, southwest Norway, during the terminal stages of Fennoscandian Shield evolution. Geosphere 14, 861–882. https://doi.org/10.1130/GES01565.1

Souza, V.S., Macambira, M.J.B., Kotschoubey, B., 2003. Idade de zircão do granito Felício Turvo, graimpo de ouro do Manelão, região do Bacajá (PA): implicações tectônicas, in: VIII Simpósio de Geologia Da Amazônia.

Stüwe, K., 2007. Geodynamics of the Lithosphere: Quantitative Description of Geological Problems, Eos Trans. AGU.

Tassinari, C.C.G., Macambira, M.J.., 2004. A evolução tectônica do Craton Amazônico, in: Mantesso-Neto, V., Bartorelli, A., Carneiro, C.D.R., Brito Neves, B.B. (Eds.), Geologia Do Continente Sul Americano: Evoluc¸ Ão Da Obra de Fernando Flávio Marques Almeida. São Paulo, pp. 471–486.

Tassinari, C.C.G., Munhá, J.M.U., Teixeira, W., Palácios, T., Nutman, A.P., Sosa, C.S., Santos, A.P., Calado, B.O., 2004. The Imataca Complex, NW Amazonian Craton, Venezuela: Crustal evolution and integration of geochronological and petrological cooling histories. Episodes 27, 3–12. https://doi.org/10.18814/epiiugs/2004/v27i1/002

Tavares, F.M., 2015. Evolução geotêctonica do nordeste da Província Carajás. Universidade Federal do Rio de Janeiro.

Tavares, F.M., Silva, C.M.G., 2012. Carta Geológica SB.22-X-C-VI FOLHA SERRA PELADA 1:10000, CPRM. CPRM, Pará, Brazil.

Taylor, R.J.M., Kirkland, C.L., Clark, C., 2016. Accessories after the facts: Constraining the timing, duration and conditions of high-temperature metamorphic processes.

Lithos 264, 239–257. https://doi.org/10.1016/j.lithos.2016.09.004

Tedeschi, M., Pedrosa-Soares, A., Dussin, I., Lanari, P., Novo, T., Pinheiro, M.A.P., Lana, C., Peters, D., 2018. Protracted zircon geochronological record of UHT garnet-free granulites in the Southern Brasília orogen (SE Brazil): Petrochronological constraints on magmatism and metamorphism. Precambrian Res. 316, 103–126. https://doi.org/10.1016/j.precamres.2018.07.023

Teixeira, A.S., Ferreira Filho, C.F., Giustina, M.E.S. Della, Araújo, S.M., da Silva, H.H.A.B., 2015. Geology, petrology and geochronology of the Lago Grande layered complex: Evidence for a PGE-mineralized magmatic suite in the Carajás Mineral Province, Brazil. J. South Am. Earth Sci. 64, 116–138. https://doi.org/10.1016/j.jsames.2015.09.006

Thompson, A.B., Schulmann, K., Jezek, J., Tolar, V., 2001. Thermally softened continental extensional zones (arcs and rifts)as precursors to thickened orogenic belts. Tectonophysics 332, 115–141. https://doi.org/10.1016/S0040-1951(00)00252-3

Touret, J.L.R., Santosh, M., Huizenga, J.M., 2016. High-temperature granulites and supercontinents. Geosci. Front. 7, 101–113. https://doi.org/10.1016/j.gsf.2015.09.001

Triboulet, C., Feybesse, J., 1998. Les métabasites birimiennes et archéennes de la région de Toulepleu-lty (Côte d'Ivoire) : des roches portées à 8 kbar et 14 kbar au Paléorprotérozoïque. Académie Sci. Paris , Sci. la terre des planètes 61–66.

Turlin, F., Deruy, C., Eglinger, A., Vanderhaeghe, O., André-Mayer, A.S., Poujol, M., Moukhsil, A., Solgadi, F., 2018. A 70 Ma record of suprasolidus conditions in the large, hot, long-duration Grenville Orogen. Terra Nov. 30, 233–243. https://doi.org/10.1111/ter.12330

Ueda, K., Gerya, T. V., Burg, J.P., 2012. Delamination in collisional orogens: Thermomechanical modeling. J. Geophys. Res. Solid Earth 117. https://doi.org/10.1029/2012JB009144

Vasquez, M.L.., Rosa-Costa, L.T.., 2008. Geologia e Recursos Minerais do Estado do Pará : Sistema de Informações Geográficas – SIG : texto explicativo dos mapas Geológico e Tectônico e de Recursos Minerais do Estado do Pará, 1st ed. Brazilian Geological Service, CPRM, Belém.

Vasquez, M.L., 2006. Geocronologia em zircão, monazita e granada e isótopos de Nd das associações litológicas da porção oeste do Domínio Bacajá: evolução crustal da porção meridional da Província Maroni-Itacaiúnas – Sudeste Do Cráton Amazônico. Universidade Federal do Pará.

Vasquez, M.L., Macambira, M.J.B., Armstrong, R.A., 2008. Zircon geochronology of granitoids from the western Bacajá domain, southeastern Amazonian craton, Brazil: Neoarchean to Orosirian evolution. Precambrian Res. 161, 279–302. https://doi.org/10.1016/j.precamres.2007.09.001

Vasquez, M.L., Macambira, M.J.B., Galarza, M.A., 2005. Granitoides Transamazônicos da região Iriri-Xingu, Pará – novos dados geológicos e geocronológicos, in: Contribuições a Geologia Da Amazônia. CPRM, Belém, p. 16.

White, Powell, Holland, Worley, 2000. The effect of TiO2 and Fe2O3 on metapelitic assemblages at greenschist and amphibolite facies conditions: Mineral equilibria calculations in the system K2O-FeO-MgO-Al2O3-SiO2-H2O-TiO2-Fe2O3. J. Metamorph. Geol. 18, 497–511. https://doi.org/10.1046/j.1525-1314.2000.00269.x

White, R.W., Pomroy, N.E., Powell, R., 2005. An in situ metatexite-diatexite transition in upper amphibolite facies rocks from Broken Hill, Australia. J. Metamorph. Geol. 23, 579–602. https://doi.org/10.1111/j.1525-1314.2005.00597.x

White, R.W., Powell, R., 2002. Melt loss and the preservation of granulite facies mineral assemblages. J. Metamorph. Geol. 20, 621–632. https://doi.org/10.1046/j.1525-1314.2002.00206_20_7.x

White, R.W., Powell, R., Clarke, G.L., 2002. The interpretation of reaction textures in Fe-rich metapelitic granulites of the Musgrave Block, Central Australia: Constraints from mineral equilibria calculations in the system. J. Metamorph. Geol. 20, 41–55. https://doi.org/10.1046/j.0263-4929.2001.00349.x

White, R.W., Powell, R., Holland, T.J.B., 2007. Progress relating to calculation of partial melting equilibria for metapelites. J. Metamorph. Geol. 25, 511–527. https://doi.org/10.1111/j.1525-1314.2007.00711.x

Whitehouse, M.J., Kemp, A.I.S., 2010. On the difficulty of assigning crustal residence, magmatic protolith and metamorphic ages to Lewisian granulites: Constraints from combined in situ U-Pb and Lu-Hf isotopes. Geol. Soc. Spec. Publ. 335, 81–101. https://doi.org/10.1144/SP335.5

Wiedenbeck, M., Allé, P., Corfu, F., Griffin, E.L., Meier, M., Oberli, F., Quadt, A.V., Roddick, J.C., Spiegel, W., 1995. Three Natural Zircon Standards for U-Th-Pb, Lu-Hf, Trace Element and Ree Analyses. Geostand. Newsl. 19, 1–23. https://doi.org/10.1111/j.1751-908X.1995.tb00147.x

Xiang, H., Zhang, Z.M., Lei, H.C., Qi, M., Dong, X., Wang, W., Lin, Y.H., 2014. Paleoproterozoic ultrahigh-temperature pelitic granulites in the northern Sulu orogen: Constraints from petrology and geochronology. Precambrian Res. 254, 273–289. https://doi.org/10.1016/j.precamres.2014.09.004

Yakymchuk, C., Kirkland, C.L., Clark, C., 2018. Th/U ratios in metamorphic zircon. J. Metamorph. Geol. 36, 715–737. https://doi.org/10.1111/jmg.12307

Zhang, Z., Xiang, H., Dong, X., Li, W., Ding, H., Gou, Z., Tian, Z., 2017. Oligocene HP metamorphism and anatexis of the Higher Himalayan Crystalline Sequence in Yadong region, east-central Himalaya. Gondwana Res. 41, 173–187. https://doi.org/10.1016/j.gr.2015.03.002

Zhao, G., Cawood, P.A., Wilde, S.A., Sun, M., 2002. Review of global 2.1-1.8 Ga orogens: Implications for a pre-Rodinia supercontinent. Earth-Science Rev. 59, 125–162. https://doi.org/10.1016/S0012-8252(02)00073-9

Zirkler, A., Johnson, T.E., White, R.W., Zack, T., 2012. Polymetamorphism in the mainland Lewisian complex, NW Scotland - phase equilibria and geochronological constraints from the Cnoc an t'Sidhean suite. J. Metamorph. Geol. 30, 865–885. https://doi.org/10.1111/j.1525-1314.2012.01003.x

11 SUPPLEMENTARY MATERIAL 3 – MINERAL COMPOSITIONS

supplementary table 1 representative mineral compositions of the sample ASM09A

Mineral	Grt						Opx				Bt						Pl				Crd		Mineral	Spl	
	Min	Max	Min	Max	Min	Max	Min	Max	Min	Max	Min	Max	Min	Max	Min	Max	Min	Max	Min	Max	Min	Max		Min	Max
texture	Core		Mantle		Rim		In grt		matrix		in grt		with crd		grt/opx corona		in grt		matrix		grt corona		texture	in grt	
SiO2 (wt%)	37.81	38.13	37.68	36.35	37.80	36.06	50.86	50.69	49.36	50.05	37.54	35.45	35.71	35.33	37.54	37.42	61.03	60.75	61.29	60.71	49.96	49.69	SiO2	0.04	0.00
TiO2	0.05	0.00	0.00	0.00	0.07	0.02	0.03	0.06	0.03	0.08	5.06	5.50	6.24	6.41	5.06	5.32	0.01	0.00	0.03	0.00	0.01	0.00	TiO2	0.00	0.08
Al2O3	21.60	21.69	22.39	21.36	21.77	21.25	5.47	6.96	5.46	6.48	14.62	15.23	14.70	14.76	14.62	14.84	24.47	24.79	23.57	24.76	34.04	33.16	Al2O3	61.08	57.51
Cr2O3	0.11	0.15	0.18	0.13	0.17	0.14	0.15	0.22	0.14	0.18	0.38	0.33	0.44	0.43	0.38	0.45	0.00	0.00	0.00	0.00	0.00	0.00	FeO	2.28	3.10
Fe2O3	2.97	2.12	2.30	5.38	2.10	4.62	0.00	0.00	0.52	0.00	0.00	0.00	0.00	0.00	0.00	0.00	0.23	0.07	0.12	0.01	0.84	1.08	Fe2O3	0.00	0.00
FeO	25.91	26.65	25.41	25.26	27.18	28.66	21.96	21.14	23.49	22.96	14.71	12.98	14.26	14.82	14.71	14.31	0.00	0.00	0.00	0.00	4.20	3.87	MnO	23.13	23.91
MnO	0.65	0.62	0.64	0.72	0.72	0.85	0.16	0.11	0.18	0.15	0.08	0.04	0.03	0.00	0.08	0.00	0.00	0.00	0.00	0.00	0.06	0.06	MgO	0.01	0.04
MgO	9.71	9.17	9.98	9.00	9.01	6.80	20.74	20.04	19.80	19.49	12.89	13.72	12.53	12.20	12.89	12.79	0.00	0.00	0.00	0.01	10.83	11.21	CaO	6.96	7.11
CaO	1.05	1.20	0.92	1.03	0.97	1.10	0.11	0.26	0.07	0.06	0.00	0.00	0.00	0.00	0.00	0.00	5.94	6.39	5.84	5.99	0.00	0.00	Na2O	0.03	0.02
Na2O	0.01	0.07	0.00	0.02	0.01	0.01	0.01	0.07	0.00	0.08	0.03	0.13	0.08	0.05	0.03	0.06	7.92	7.64	7.87	7.60	0.03	0.03	K2O	0.11	0.00
K2O	0.00	0.04	0.01	0.01	0.00	0.01	0.00	0.00	0.00	0.00	9.23	9.69	9.41	9.53	9.23	9.53	0.42	0.28	0.36	0.27	0.00	0.02	Cr2O3	0.00	0.00
total	99.87	99.84	99.51	99.26	99.80	99.52	99.49	99.55	99.05	99.53	94.54	93.07	93.40	93.53	94.54	94.72	100.02	99.92	99.08	99.35	99.97	99.12	ZnO	3.65	6.97
O	12						6				11						8				18		NiO	0.23	0.16
Si	2.924	2.951	2.909	2.851	2.934	2.863	1.894	1.877	1.868	1.872	2.819	2.733	2.727	2.706	2.819	2.804	2.714	2.702	2.746	2.711	4.973	4.989	Totoal	97.52	98.90
Ti	0.003	0.000	0.000	0.000	0.004	0.001	0.001	0.002	0.001	0.002	0.286	0.322	0.358	0.369	0.286	0.300	0.000	0.000	0.001	0.000	0.001	0.000	O	4	
Al(total)	1.969	1.979	2.038	1.976	1.992	1.989	0.240	0.304	0.244	0.286	1.294	1.384	1.324	1.333	1.294	1.311	1.283	1.300	1.245	1.303	3.995	3.925	Si	0	0
Cr	0.007	0.009	0.011	0.008	0.011	0.009	0.004	0.006	0.004	0.005	0.023	0.022	0.027	0.026	0.023	0.027	0.000	0.000	0.000	0.000	0.000	0.000	Ti	0.001	0.002
Fe3+	0.173	0.123	0.134	0.318	0.123	0.276	0.000	0.000	0.015	0.000	0.000	0.000	0.000	0.000	0.000	0.000	0.008	0.002	0.004	0.000	0.063	0.081	Al	2.030	1.992
Fe2+	1.675	1.725	1.641	1.657	1.764	1.903	0.684	0.655	0.743	0.718	0.924	0.855	0.911	0.950	0.924	0.897	0.000	0.000	0.000	0.000	0.349	0.325	Cr	0.051	0.072
Mn	0.042	0.040	0.042	0.048	0.047	0.057	0.005	0.003	0.006	0.005	0.005	0.001	0.002	0.000	0.005	0.000	0.000	0.000	0.000	0.000	0.005	0.005	Fe3	0.000	0.000
Mg	1.119	1.058	1.148	1.052	1.042	0.804	1.151	1.106	1.117	1.086	1.442	1.550	1.426	1.393	1.442	1.428	0.000	0.000	0.000	0.000	1.607	1.678	Fe2	0.548	0.588
Ca	0.087	0.099	0.076	0.086	0.081	0.093	0.004	0.010	0.003	0.002	0.000	0.000	0.000	0.000	0.000	0.000	0.283	0.305	0.280	0.287	0.000	0.000	Mn	0.002	0.001
Na	0.001	0.010	0.000	0.003	0.002	0.002	0.001	0.005	0.000	0.006	0.004	0.020	0.012	0.007	0.004	0.009	0.683	0.658	0.684	0.658	0.006	0.006	Mg	0.322	0.311
K	0.000	0.004	0.001	0.001	0.000	0.001	0.000	0.000	0.000	0.000	0.884	0.934	0.917	0.931	0.884	0.911	0.024	0.016	0.020	0.015	0.000	0.002	Ca	0.002	0.001
XGrs	0.030	0.034	0.026	0.030	0.028	0.033	-	-	-	-	-	-	-	-	-	-	-	-	-	-	-	-	Na	0.005	0.000

XAl(M1)							0.13	0.18	0.11	0.16													K	0.001	0.000
XAn	-	-	-	-	-	-	-	-	-	-	-	-	-	-	-	-	0.29	0.31	0.28	0.30	-	-			
XMg	-	-	-	-	-	-	-	-	-	-	0.61	0.64	0.61	0.59	0.61	0.61	-	-	-	-	0.82	0.84	-	-	-

$X_{Grs} = Ca^{2+}/(Ca^{2+} + Mg^{2+} + Fe^{2+})$; $XAl(M1) = Al_{(total)}-(2-Si)$, $X_{Mg} = Mg^{2+}/(Fe^{2+} + Mg^{2+})$; $X_{An} = Ca^{2+}/(Ca^{2+} + Na^{+} + K^{+})$;

Min and Max are depending on the XGrs content for Grt, XAl(M1) for Opx, TiO_2 for Bt, XAn for Pl, XMg for crd.

supplementary table 2 representative mineral compositions of the sample ASM19A

Mineral	Grt						Bt						Pl		Crd	
	Min	Max	Min	Max	Min	Max	Min	Max	Min	Max	Min	Max	Min	Max	Min	Max
texture	Core		Mantle		Rim		Inclusion grt		corona		matrix		matrix		matrix	
SiO_2 (wt%)	36.53	35.19	36.32	36.64	36.60	35.89	35.75	34.54	34.95	34.92	35.04	35.15	60.73	61.69	48.42	48.73
TiO_2	0.00	0.05	0.00	0.00	0.01	0.00	3.50	5.65	3.72	5.42	4.49	4.00	0.04	0.03	0.03	0.07
Al_2O_3	20.84	20.15	20.90	20.90	21.22	20.76	18.50	17.45	17.37	17.04	17.06	16.56	23.90	24.15	34.51	33.30
Cr_2O_3	0.03	0.07	0.04	0.06	0.00	0.07	0.08	0.09	0.16	0.13	0.14	0.14	0.00	0.00	0.00	0.04
Fe_2O_3	2.39	4.24	3.27	2.71	2.89	3.76	0.00	0.00	0.00	0.00	0.00	0.00	0.12	0.04	0.00	1.30
FeO	31.19	29.40	32.06	32.54	32.90	33.04	14.55	14.46	18.43	17.98	18.60	18.74	0.00	0.00	7.25	6.28
MnO	0.63	0.71	0.75	0.68	0.72	0.88	0.02	0.00	0.11	0.03	0.02	0.07	0.00	0.00	9.86	0.03
MgO	5.84	5.85	4.87	5.11	4.89	4.27	11.64	10.94	10.11	9.38	9.70	9.66	0.00	0.00	0.03	9.06
CaO	1.07	1.09	0.98	1.02	0.90	0.94	0.00	0.00	0.00	0.00	0.00	0.00	5.50	5.89	0.01	0.02
Na_2O	0.01	0.04	0.10	0.03	0.06	0.03	0.13	0.31	0.14	0.08	0.08	0.15	8.37	7.96	0.08	0.12
K_2O	0.01	0.00	0.07	0.01	0.00	0.01	9.05	9.37	9.39	9.66	9.60	9.41	0.23	0.27	0.03	0.01
total	98.54	96.78	99.36	99.70	100.19	99.65	93.22	92.81	94.38	94.64	94.73	93.88	98.89	100.03	100.22	98.97
O	12.00						11.00						8.00		18.00	
Si	2.939	2.891	2.921	2.933	2.919	2.898	2.712	2.653	2.688	2.676	2.688	2.722	2.728	2.736	4.874	4.958
Ti	0.000	0.003	0.000	0.000	0.001	0.000	0.200	0.326	0.259	0.312	0.259	0.233	0.001	0.001	0.002	0.006
Al(total)	1.977	1.952	1.981	1.972	1.996	1.976	1.654	1.580	1.543	1.539	1.543	1.512	1.266	1.263	4.096	3.994
Cr	0.002	0.005	0.003	0.004	0.000	0.004	0.005	0.005	0.008	0.008	0.008	0.009	0.000	0.000	0.000	0.003
Fe^{3+}	0.145	0.262	0.198	0.163	0.174	0.228	0.000	0.000	0.000	0.000	0.000	0.000	0.004	0.001	0.000	0.100
Fe^{2+}	2.099	2.020	2.156	2.178	2.195	2.231	0.923	0.929	1.193	1.152	1.193	1.214	0.000	0.000	0.611	0.535

Mn	0.043	0.049	0.051	0.046	0.049	0.060	0.001	0.000	0.001	0.002	0.001	0.005	0.000	0.000	0.003	0.003
Mg	0.700	0.716	0.584	0.610	0.581	0.514	1.316	1.252	1.109	1.071	1.109	1.115	0.000	0.000	1.479	1.374
Ca	0.092	0.096	0.084	0.087	0.077	0.081	0.000	0.000	0.000	0.000	0.000	0.000	0.265	0.280	0.001	0.002
Na	0.002	0.006	0.016	0.005	0.009	0.005	0.019	0.046	0.012	0.012	0.012	0.023	0.729	0.685	0.016	0.024
K	0.001	0.000	0.007	0.001	0.000	0.001	0.876	0.918	0.940	0.944	0.940	0.930	0.013	0.015	0.003	0.002
XGrs	0.031	0.033	0.029	0.030	0.027	0.028	-	-	-	-	-	-	-	-	-	-
XAn	-	-	-	-	-	-	-	-	-	-	-	-	0.263	0.286	-	-
XMg	-	-	-	-	-	-	0.588	0.574	0.482	0.482	0.482	0.479	-	-	0.708	0.720

$X_{Grs} = Ca^{2+}/(Ca^{2+} + Mg^{2+} + Fe^{2+})$; $X_{Mg} = Mg^{2+}/(Fe^{2+} + Mg^{2+})$; $X_{An} = Ca^{2+}/(Ca^{2+} + Na^{+} + K^{+})$;

Min and Max are depending on the XGrs content for Grt, TiO_2 in Bt, XAn for Pl, XMg for crd

12 SUPPLEMENTARY MATERIAL 4 – U-PB DATA

supplementary table 3 LA-ICP-MS U-Pb data for sample ASM09A - Opx-grt aluminous granulite residue

Location - lat: 560795	Long: 9435061						Radiogenic ratios					Apparent ages						
Identifier	Spot number	^{206}Pb cps	U ppm[1]	Th/U	$^{206}Pb/^{204}Pb$	1s%	$^{207}Pb/^{235}U$	2s%	$^{206}Pb/^{238}U$	2s%	Rho	$^{207}Pb/^{206}Pb$	2s (abs)	$^{206}Pb/^{238}U$	2s (abs)	$^{207}Pb/^{235}U$	2s (abs)	% conc [2]
D	#70.1	0.077	719	2.27	238006	15.9	26.2067	3.5	0.68409	3.0	0.83	3320	31	3360	78	3354	35	101.2
D	#63.2	350518	106	1.33	10003	33.25	25.8131	1.3	0.69388	0.7	0.49	3297	15	3397	20	3339	13	103.0
D	#47.2	440096	147	0.67	11784	49.94	22.5486	1.3	0.64092	0.8	0.29	3213	15	3192	20	3208	13	99.4
D	#06.1	0.010	168	0.49	23437	48.0	21.4906	3.9	0.61582	3.7	0.93	3208	26	3093	90	3161	39	96.4
D	#41.1	0.019	365	0.49	75540	16.1	22.4081	3.5	0.64612	3.1	0.89	3186	23	3213	79	3201	34	100.8
D	#11.2	1114094	419	1.43	13599	71.01	20.3857	1.2	0.59373	0.6	0.31	3174	14	3004	16	3110	12	94.6
D	#24.1	0.008	124	0.96	5598	39.9	24.3756	4.7	0.71475	4.6	0.98	3168	27	3476	123	3283	47	109.7
D	#67.1	0.019	215	0.68	38184	12.0	19.4875	4.2	0.58820	3.4	0.81	3167	39	2982	81	3066	41	94.2
D	#84.1	0.005	64	0.75	4553	35.7	18.8190	3.3	0.59652	2.8	0.85	3131	28	3016	68	3032	32	96.3
D	#61.2	621307	201	0.95	2148	466.67	21.0785	1.3	0.64093	0.7	0.19	3105	16	3193	18	3142	13	102.8
D	#44.2	171907	62	1.60	41622	33.90	18.8997	1.3	0.57911	1.0	0.38	3088	17	2944	24	3036	13	95.4
D	#56.1	0.015	266	0.21	207761	11.1	20.4109	3.2	0.62851	3.1	0.95	3084	22	3144	76	3111	31	101.9
D	#43.2	800685	300	1.13	7580	128.93	18.4875	1.2	0.57307	0.7	0.30	3077	14	2920	16	3015	12	94.9
D	#64.2	408716	153	0.88	8883	64.65	18.1147	1.7	0.56849	0.9	0.35	3055	22	2901	22	2995	16	95.0
D	#29.2	411916	139	1.50	-8849	53.52	19.1507	1.3	0.60567	0.7	0.42	3041	15	3052	18	3049	13	100.4
D	#20.1	0.007	147	1.09	16803	24.2	18.9670	3.1	0.62047	3.1	0.97	3000	21	3112	75	3040	31	103.7

D	#47.1	0.009	154	0.57	40357	18.5	19.0339	4.2	0.62142	3.4	0.80	2984	34	3115	84	3043	41	104.4
D	#48.1	0.010	207	0.74	68639	16.3	18.6450	3.2	0.61264	3.1	0.96	2983	22	3080	76	3023	32	103.3
D	#69.1	0.010	116	1.34	42977	36.6	17.3950	3.8	0.58636	3.0	0.79	2970	37	2974	71	2956	37	100.1
D	#85.1	0.043	436	2.12	86072	92.3	20.2563	5.0	0.63212	4.0	0.79	2964	50	3157	99	3102	49	106.5
D	#35.1	0.015	311	0.31	68526	22.6	18.5240	3.4	0.61946	3.3	0.97	2958	21	3108	81	3017	33	105.1
D	#50.2	1054000	442	0.49	95932	34.15	15.6057	1.2	0.52240	0.6	0.54	2953	14	2709	14	2853	12	91.7
D	#65.2	363895	139	3.28	7883	92.49	16.0864	1.3	0.54795	0.8	0.49	2919	16	2816	19	2882	14	96.5
D	#19.1	0.016	341	0.71	25212	131.2	15.9869	4.8	0.54994	3.8	0.78	2913	34	2824	86	2876	47	97.0
D	#71.1	0.005	62	1.62	10017	26.9	15.0572	3.6	0.53839	2.9	0.80	2894	36	2777	66	2818	35	95.9
D	#39.1	0.008	164	0.49	37530	29.5	16.4383	4.1	0.57525	3.5	0.85	2872	31	2929	82	2902	39	102.0
D	#72.1	0.011	139	0.61	61209	21.7	15.1075	3.5	0.54694	2.9	0.81	2855	34	2812	65	2822	34	98.5
D	#23.1	0.012	260	0.76	34438	34.7	14.8791	4.3	0.53294	3.2	0.74	2844	33	2754	71	2807	41	96.8
D	#25.1	0.023	510	0.57	53403	31.1	15.2924	3.8	0.56096	3.1	0.83	2814	31	2871	73	2833	37	102.0
D	#12.1	0.029	694	0.01	34265	42.7	14.3799	3.8	0.54811	3.4	0.89	2767	32	2817	78	2775	37	101.8
D	#17.2	930593	409	0.04	1479084	36.41	12.8147	1.3	0.50760	0.6	0.16	2681	15	2646	14	2666	12	98.7
D	#09.2	941334	429	0.09	74795	53.20	12.0519	1.4	0.49188	0.7	0.60	2628	16	2579	15	2608	13	98.1
D	#51.1	0.022	557	0.06	188733	1.5	12.1272	3.6	0.49801	3.3	0.91	2624	28	2605	71	2614	34	99.3
D	#60.2	509166	216	0.32	7188	86.87	11.8591	1.4	0.48772	0.8	0.48	2608	18	2561	18	2593	13	98.2
M	#52.1	0.004	125	0.89	283358	0.5	7.1027	3.8	0.39540	3.1	0.82	2097	28	2148	57	2124	34	102.4
M	#26.2	328947	177	0.94	27928	26.97	6.9597	1.2	0.39271	0.7	0.08	2075	16	2135	13	2106	11	102.9
M	#49.1	0.019	683	0.14	90047	11.0	6.2167	3.9	0.35174	3.7	0.97	2070	24	1943	63	2006	34	93.9
M	#08.1	0.008	248	0.64	22961	11.2	6.7428	3.2	0.38385	3.1	0.97	2067	23	2094	56	2078	29	101.3
~~NU~~	~~#87.1~~	~~0.033~~	~~1497~~	~~0.09~~	~~10792~~	~~39.0~~	~~2.1041~~	~~7.9~~	~~0.16095~~	~~5.8~~	~~0.73~~	~~1586~~	~~103~~	~~962~~	~~52~~	~~1143~~	~~49~~	~~60.6~~
~~NU~~	~~#86.1~~	~~0.025~~	~~1110~~	~~0.10~~	~~10300~~	~~45.2~~	~~2.0975~~	~~5.8~~	~~0.15274~~	~~4.8~~	~~0.83~~	~~1555~~	~~59~~	~~916~~	~~41~~	~~1141~~	~~34~~	~~58.9~~
~~NU~~	~~#07.1~~	~~0.029~~	~~2244~~	~~0.06~~	~~14739~~	~~70.0~~	~~2.0168~~	~~3.2~~	~~0.15477~~	~~3.0~~	~~0.96~~	~~1522~~	~~25~~	~~928~~	~~26~~	~~1121~~	~~22~~	~~60.9~~
~~NU~~	~~#22.1~~	~~0.010~~	~~722~~	~~0.05~~	~~20146~~	~~116.6~~	~~1.8082~~	~~5.2~~	~~0.14454~~	~~4.2~~	~~0.81~~	~~1445~~	~~45~~	~~870~~	~~34~~	~~1047~~	~~34~~	~~60.2~~
~~NU~~	~~#40.1~~	~~0.025~~	~~2220~~	~~0.05~~	~~22323~~	~~45.7~~	~~1.7515~~	~~3.1~~	~~0.14102~~	~~3.1~~	~~0.97~~	~~1423~~	~~25~~	~~850~~	~~24~~	~~1028~~	~~20~~	~~59.8~~
~~NU~~	~~#74.1~~	~~0.026~~	~~1410~~	~~0.09~~	~~15865~~	~~63.7~~	~~1.3762~~	~~6.2~~	~~0.12296~~	~~4.9~~	~~0.78~~	~~1244~~	~~76~~	~~747~~	~~34~~	~~877~~	~~36~~	~~60.1~~
~~NU~~	~~#73.1~~	~~0.014~~	~~765~~	~~0.11~~	~~18155~~	~~75.1~~	~~1.4017~~	~~5.6~~	~~0.12008~~	~~4.6~~	~~0.81~~	~~1234~~	~~65~~	~~731~~	~~31~~	~~888~~	~~33~~	~~59.2~~
~~NU~~	~~#27.2~~	~~890644~~	~~1317~~	~~0.13~~	~~6968~~	~~14.25~~	~~1.9935~~	~~4.2~~	~~0.14716~~	~~2.6~~	~~0.97~~	~~1587~~	~~34~~	~~885~~	~~22~~	~~1110~~	~~29~~	~~55.8~~
~~NU~~	~~#88.1~~	~~0.012~~	~~539~~	~~0.08~~	~~10022~~	~~91.0~~	~~2.1183~~	~~9.2~~	~~0.14805~~	~~6.0~~	~~0.65~~	~~1527~~	~~133~~	~~890~~	~~50~~	~~1151~~	~~62~~	~~58.3~~
~~NU~~	~~#11.1~~	~~0.013~~	~~1005~~	~~0.05~~	~~13039~~	~~88.1~~	~~1.9556~~	~~9.3~~	~~0.14385~~	~~4.3~~	~~0.46~~	~~1587~~	~~83~~	~~866~~	~~35~~	~~1096~~	~~60~~	~~54.6~~
~~NU~~	~~#42.2~~	~~1069919~~	~~1173~~	~~0.14~~	~~77075~~	~~37.03~~	~~2.9149~~	~~1.4~~	~~0.19201~~	~~0.9~~	~~0.91~~	~~1794~~	~~15~~	~~1132~~	~~9~~	~~1385~~	~~11~~	~~63.1~~
~~NU~~	~~#82.1~~	~~0.019~~	~~761~~	~~0.10~~	~~89208~~	~~78.6~~	~~2.4981~~	~~3.6~~	~~0.16408~~	~~3.0~~	~~0.82~~	~~1663~~	~~38~~	~~979~~	~~27~~	~~1271~~	~~26~~	~~58.9~~
~~NU~~	~~#34.1~~	~~0.017~~	~~564~~	~~0.10~~	~~6243~~	~~102.6~~	~~6.1858~~	~~4.2~~	~~0.33050~~	~~3.5~~	~~0.84~~	~~2170~~	~~32~~	~~1841~~	~~56~~	~~2002~~	~~37~~	~~84.8~~
~~NU~~	~~#66.1~~	~~0.033~~	~~946~~	~~0.04~~	~~47299~~	~~21.7~~	~~4.2714~~	~~5.6~~	~~0.21567~~	~~4.5~~	~~0.81~~	~~2223~~	~~58~~	~~1259~~	~~52~~	~~1684~~	~~43~~	~~56.6~~
~~NU~~	~~#10.1~~	~~0.017~~	~~747~~	~~0.04~~	~~17585~~	~~83.9~~	~~4.8666~~	~~4.4~~	~~0.24872~~	~~3.5~~	~~0.81~~	~~2257~~	~~35~~	~~1432~~	~~46~~	~~1796~~	~~37~~	~~63.4~~
~~NU~~	~~#14.1~~	~~0.015~~	~~802~~	~~0.83~~	~~3850~~	~~110.0~~	~~3.7241~~	~~4.6~~	~~0.20431~~	~~3.4~~	~~0.74~~	~~2134~~	~~37~~	~~1198~~	~~37~~	~~1576~~	~~37~~	~~56.2~~
~~NU~~	~~#36.1~~	~~0.033~~	~~1493~~	~~0.08~~	~~24874~~	~~39.9~~	~~5.2655~~	~~3.9~~	~~0.28334~~	~~3.7~~	~~0.94~~	~~2164~~	~~28~~	~~1608~~	~~53~~	~~1863~~	~~34~~	~~74.3~~

NU	#27.1	0.027	1366	0.06	41784	74.3	3.4206	3.5	0.22523	3.1	0.90	1811	26	1309	37	1509	27	72.3
NU	#33.1	0.022	1340	0.07	18737	85.6	3.5296	6.0	0.21641	3.8	0.63	1935	62	1263	43	1532	48	65.3
NU	#42.1	0.006	311	0.04	14701	105.3	3.0957	4.6	0.19043	4.2	0.90	1921	35	1124	43	1431	36	58.5
NU	#55.1	0.052	1357	0.78	41181	100.5	15.0381	3.2	0.49930	3.2	0.98	2978	21	2611	69	2818	31	87.7
NU	#80.1	0.035	629	1.02	43670	31.3	11.1575	4.2	0.38959	3.6	0.84	2958	36	2121	64	2535	39	71.7
NU	#09.1	0.016	527	0.84	573	103.7	9.6229	4.0	0.32722	3.5	0.87	2937	30	1825	56	2399	37	62.1
NU	#38.1	0.039	1337	0.34	13109	25.9	10.3366	3.4	0.35006	3.2	0.95	2926	24	1935	54	2465	32	66.1
NU	#37.1	0.008	209	0.15	1484	97.5	11.2929	3.5	0.39884	3.3	0.95	2870	26	2164	61	2547	33	75.4
NU	#81.1	0.040	690	1.95	25380	114.0	11.1017	5.9	0.35986	5.2	0.87	2870	46	1980	88	2529	54	69.0
NU	#53.1	0.054	1789	0.90	3728	16.9	10.6541	3.8	0.38771	3.4	0.89	2824	28	2112	61	2493	35	74.8
NU	#65.1	0.017	286	0.48	4154	16.7	10.3771	4.7	0.40756	4.3	0.93	2773	29	2203	80	2469	44	79.5
NU	#50.1	0.012	416	0.28	20790	91.4	8.3057	4.3	0.31247	3.8	0.90	2762	31	1753	59	2264	39	63.5
NU	#28.1	0.021	596	0.28	34679	99.0	9.9338	5.5	0.39154	3.3	0.59	2688	46	2130	60	2428	51	79.2
NU	#05.1	0.008	229	0.03	13455	136.2	8.5707	4.0	0.35595	3.8	0.95	2612	26	1963	64	2293	36	75.1
NU	#79.1	0.024	573	0.90	5363	63.0	7.2813	6.3	0.28499	4.7	0.74	2609	70	1615	67	2143	54	61.9
NU	#68.1	0.015	296	1.13	1602	90.3	7.9381	4.4	0.29855	3.6	0.81	2569	43	1684	53	2223	39	65.5
NU	#13.1	0.009	288	0.12	21430	77.2	7.1596	4.6	0.30867	3.7	0.81	2549	38	1734	57	2131	41	68.0
NU	#54.1	0.005	177	10.88	5694	105.3	6.3143	4.1	0.30008	3.9	0.95	2377	27	1692	58	2020	36	71.2
NU	#26.1	0.010	394	0.03	2630	75.6	5.9115	4.3	0.28544	3.9	0.91	2350	30	1618	56	1962	37	68.9
NU	#21.1	0.012	674	0.28	7218	76.1	3.5477	6.0	0.19223	3.7	0.63	2151	53	1133	39	1537	47	52.7
NU	#83.1	0.019	1150	0.10	8495	65.4	1.2157	3.9	0.11570	3.3	0.85	1157	41	706	22	807	21	61.0
NU	#34.2	348495	146	0.61	3338	47.96	14.6901	1.3	0.49853	0.8	0.27	2928	17	2607	18	2795	12	89.0
NU	#45.2	1181671	509	0.23	20133	39.90	14.0824	1.3	0.48712	0.7	0.58	2895	14	2558	14	2755	12	88.4
NU	#48.2	398659	173	0.60	5804	105.09	15.7726	1.4	0.50132	1.0	0.63	3037	17	2619	21	2863	14	86.3
NU	#30.2	414248	198	0.36	4712	46.83	11.6551	1.5	0.44181	0.9	0.75	2753	16	2358	19	2576	13	85.7
NU	#32.2	630590	313	0.23	17188	45.42	11.8639	1.4	0.43495	0.7	0.57	2809	16	2328	14	2593	13	82.9
NU	#10.2	865672	482	1.03	6237	133.41	10.2919	1.3	0.39998	0.7	0.58	2709	15	2169	13	2461	12	80.1
NU	#66.2	737459	390	2.35	8532	45.38	11.7131	1.3	0.42026	0.8	0.60	2846	16	2262	15	2582	12	79.5
NU	#28.2	684856	371	0.35	13071	23.29	10.6405	1.3	0.39210	0.8	0.87	2800	17	2132	14	2492	12	76.1
NU	#25.2	620381	304	0.68	9214	43.58	13.3661	1.2	0.42599	0.7	0.27	3030	14	2288	13	2706	12	75.5
NU	#58.2	664399	384	2.89	5162	8.78	10.0862	1.9	0.37725	1.2	0.97	2767	16	2062	22	2438	18	74.5
NU	#62.2	1007756	661	0.05	14747	65.62	7.1497	1.4	0.31962	0.7	0.70	2471	16	1788	11	2130	12	72.3
NU	#46.2	778689	489	0.31	21377	33.22	8.5376	1.3	0.34421	0.7	0.53	2648	15	1907	12	2290	12	72.0
NU	#15.2	1021047	637	2.17	2625	5.04	9.8636	1.3	0.36226	0.7	0.66	2805	15	1993	13	2422	13	71.0
NU	#59.2	776983	534	2.73	15386	21.92	8.0563	1.2	0.32123	0.7	0.61	2669	15	1796	11	2237	11	67.3
NU	#33.2	1064286	984	0.09	7469	7.89	3.9938	3.1	0.23220	2.1	0.97	2016	23	1345	26	1627	26	66.7
NU	#49.2	820844	588	1.21	9053	15.05	7.4992	1.3	0.30985	0.7	0.33	2609	17	1740	11	2173	12	66.7
NU	#18.2	557921	364	1.21	3467	206.35	9.4190	1.3	0.33040	0.8	0.65	2876	15	1840	13	2379	12	64.0
NU	#31.2	804858	633	0.56	8257	14.66	6.2507	1.5	0.27702	0.9	0.67	2499	16	1576	13	2011	13	63.1

~~NU~~	~~#57.2~~	~~1016269~~	~~800~~	~~0.09~~	~~72481~~	~~77.46~~	~~6.2030~~	~~1.3~~	~~0.27252~~	~~0.7~~	~~0.66~~	~~2502~~	~~15~~	~~1554~~	~~9~~	~~2005~~	~~11~~	~~62.1~~
~~NU~~	~~#41.2~~	~~1165635~~	~~1428~~	~~0.11~~	~~18629~~	~~122.47~~	~~2.5103~~	~~1.3~~	~~0.17509~~	~~0.7~~	~~0.85~~	~~1692~~	~~16~~	~~1040~~	~~7~~	~~1275~~	~~10~~	~~61.5~~
~~NU~~	~~#16.2~~	~~662141~~	~~1271~~	~~0.12~~	~~14278~~	~~26.12~~	~~1.2762~~	~~1.4~~	~~0.11642~~	~~0.8~~	~~0.78~~	~~1185~~	~~19~~	~~710~~	~~5~~	~~835~~	~~8~~	~~59.9~~
~~NU~~	~~#14.2~~	~~1338367~~	~~1204~~	~~2.20~~	~~5734~~	~~8.43~~	~~5.7771~~	~~1.6~~	~~0.25335~~	~~0.9~~	~~0.85~~	~~2511~~	~~18~~	~~1456~~	~~12~~	~~1942~~	~~15~~	~~58.0~~
~~NU~~	~~#13.2~~	~~429266~~	~~333~~	~~1.29~~	~~8964~~	~~38.31~~	~~8.2574~~	~~1.3~~	~~0.28965~~	~~0.7~~	~~0.54~~	~~2878~~	~~15~~	~~1640~~	~~11~~	~~2259~~	~~12~~	~~57.0~~
~~NU~~	~~#12.2~~	~~1199904~~	~~1087~~	~~0.72~~	~~871~~	~~3.03~~	~~6.2802~~	~~1.6~~	~~0.25080~~	~~0.8~~	~~0.87~~	~~2666~~	~~19~~	~~1443~~	~~10~~	~~2015~~	~~14~~	~~54.1~~

[1] concentration uncertainty c.20%, [3] Concordance calculated as (^{206}Pb-^{238}U age/^{207}Pb-^{235}U age)*100, NU = not used for age calculations

supplementary table 4 LA-ICP-MS data for sample ASM10 charnockitic felsic granulite

Location – lat: 560011 long: 9433344							Radiogenic ratios					apparent ages						
identifier	Spot number	^{206}Pb cps	U ppm[1]	Th/U	$^{206}Pb/^{204}Pb$	1s%	$^{207}Pb/^{235}U$	2s%	$^{206}Pb/^{238}U$	2s%	Rho	$^{207}Pb/^{206}Pb$	2s (abs)	$^{206}Pb/^{238}U$	2s (abs)	$^{207}Pb/^{235}U$	2s (abs)	% conc [2]
M	#14.2	579599	396	0.30	18007	66.5	6.2108	1.0	0.35322	1.0	0.78	2048	9	1950	21	2006	11	95.2
M	#13.2	290988	187	0.22	17917	28.8	7.1631	1.1	0.40019	1.0	0.23	2090	8	2170	19	2132	9	103.8
M	#77.2	765476	567	0.30	5606	84.7	7.2394	1.3	0.40114	1.2	0.35	2109	6	2174	18	2141	9	103.1
M	#79.2	196370	150	1.42	5187	53.8	6.9631	1.4	0.38743	1.2	0.92	2101	11	2111	20	2106	10	100.5
M	#11.1	0.010	198	0.45	37867	49.3	6.6706	5.2	0.38472	4.0	0.78	2110	55	2098	72	2067	45	99.4
M	#25.1	0.007	150	0.15	18986	48.0	6.6493	3.5	0.37476	2.9	0.81	2089	37	2052	50	2065	31	98.2
M	#39.1	0.008	163	0.72	79802	8.1	7.1622	3.3	0.39871	2.8	0.85	2077	31	2163	51	2130	28	104.1
Pop. 1a	#28.2	622927	593	1.30	1501	2.3	5.6881	1.1	0.25399	1.0	0.78	2466	11	1459	17	1929	13	59.2
Pop. 1a	#29.2	738090	704	2.20	1646	1.2	6.1874	1.2	0.27038	1.1	0.86	2512	5	1543	14	2002	10	61.4
Pop. 1a	#30.2	1215572	1464	1.97	1102	1.6	4.8074	1.1	0.22716	1.1	0.66	2392	6	1320	12	1786	9	55.2
Pop. 1a	#34.2	419514	215	0.46	5639	97.8	14.0828	1.1	0.54144	1.1	0.35	2733	10	2789	27	2755	11	102.1
Pop. 1a	#43.2	892330	882	2.96	1862	1.7	6.3021	1.1	0.27607	1.0	0.87	2511	6	1571	15	2018	11	62.6
Pop. 1a	#46.2	553309	852	1.68	1248	1.7	3.3392	1.1	0.17924	1.0	0.51	2160	8	1063	10	1490	9	49.2
Pop. 1a	#47.2	729865	1070	1.14	1049	1.8	3.7740	1.1	0.19358	1.0	0.50	2243	8	1141	11	1587	9	50.8
Pop. 1a	#50.2	780063	726	4.17	1308	2.6	7.0818	1.1	0.30288	1.0	0.68	2547	12	1705	17	2121	12	66.9
Pop. 1a	#66.2	601090	934	3.71	2414	4.0	3.7161	1.5	0.19101	1.3	0.56	2243	11	1127	12	1575	10	50.2
Pop. 1a	#13.1	0.015	366	1.04	2237	58.3	7.2736	5.5	0.30663	4.9	0.90	2503	40	1723	74	2161	65	68.8
Pop. 1a	#28.1	0.038	883	0.90	2659	57.1	8.0177	5.0	0.32949	4.1	0.82	2582	49	1836	66	2232	46	71.1
Pop. 1a	#33.1	0.007	131	1.60	5311	95.7	9.7514	5.1	0.38604	3.9	0.75	2514	58	2104	70	2410	47	83.7
Pop. 1b	#11.2	895445	487	0.42	27439	45.8	11.5465	1.0	0.48973	1.0	0.53	2571	6	2569	21	2568	10	99.9
Pop. 1b	#12.2	784307	731	1.27	2543	2.5	6.0797	1.1	0.28348	1.0	0.95	2407	6	1609	18	1986	12	66.8
Pop. 1b	#17.2	508498	455	3.58	3072	9.1	5.9227	1.1	0.27527	1.0	0.31	2401	7	1567	14	1964	9	65.3
Pop. 1b	#26.2	829932	852	1.07	2974	2.1	5.0492	1.1	0.24024	1.0	0.79	2361	10	1388	14	1826	11	58.8
Pop. 1b	#57.2	496087	558	1.96	2283	3.2	5.0922	1.3	0.24409	1.1	0.60	2347	7	1408	13	1834	9	60.0
Pop. 1b	#62.2	614457	465	2.13	4128	8.9	8.6193	1.2	0.37802	1.1	0.81	2506	6	2068	19	2298	11	82.6
Pop. 1b	#74.2	569576	911	2.15	1024	2.1	3.5992	1.5	0.18783	1.1	0.35	2217	9	1110	11	1549	9	50.0
Pop. 1b	#81.2	1269589	1694	0.24	1548	2.6	4.1519	1.1	0.20887	1.0	0.80	2262	10	1223	13	1664	11	54.0
Pop. 1b	#06.1	0.008	206	0.96	1349	101.1	5.6375	4.2	0.26449	3.7	0.87	2213	37	1513	49	1920	35	68.4
Pop. 1b	#09.1	0.027	815	0.51	2397	134.3	5.1146	4.9	0.25200	4.0	0.82	2364	49	1449	52	1837	42	61.3

Pop. 1b	#19.1	0.022	795	0.68	842	41.7	4.3508	6.2	0.21691	4.1	0.67	2288	75	1265	47	1697	46	55.3
Pop. 1b	#20.1	0.020	612	0.12	2667	105.1	5.6711	4.8	0.26605	3.9	0.81	2496	49	1521	53	1925	41	60.9
Pop. 1b	#23.1	0.025	841	0.95	2584	108.3	4.9046	4.5	0.24122	3.6	0.80	2388	44	1393	45	1803	38	58.3
Pop. 1b	#26.1	0.031	1132	1.36	1636	32.3	4.5570	5.9	0.21893	4.9	0.83	2382	56	1276	57	1737	46	53.6
inheritance	#80.2	1565919	685	0.15	143335	46.1	27.5754	1.5	0.66803	1.3	0.53	3461	5	3298	26	3404	11	95.3
NU	#78.2	597562	523	0.27	6111	51.4	6.3933	1.0	0.35606	1.0	0.60	2107	13	1963	22	2031	11	93.2
NU	#22.1	0.009	168	0.40	8268	132.1	7.9314	4.1	0.40003	3.1	0.75	2111	46	2169	57	2222	37	102.7
NU	#75.2	403865	335	0.29	28660	59.0	6.7380	2.8	0.36953	1.1	0.20	2133	20	2027	23	2077	12	95.0
NU	#09.2	625288	496	1.97	3715	6.7	7.9184	1.2	0.33840	1.1	0.82	2563	14	1879	22	2221	16	73.3
NU	#32.2	1192364	959	1.82	3988	3.1	7.9103	1.1	0.33598	1.0	0.74	2568	6	1867	17	2221	10	72.7
NU	#41.2	768017	658	2.24	4039	4.2	7.3824	1.2	0.32095	1.1	0.81	2526	8	1794	18	2159	11	71.0
NU	#59.2	1122115	1144	3.00	3252	3.4	6.9309	1.1	0.29451	1.1	0.66	2567	8	1664	16	2102	10	64.8
NU	#45.2	740454	584	2.75	2708	2.8	8.2222	1.0	0.34546	1.0	0.73	2578	6	1913	18	2256	10	74.2
NU	#36.1	0.007	145	1.61	4982	101.9	8.2422	6.8	0.32978	6.1	0.90	2487	51	1836	97	2254	60	73.8
NU	#12.1	0.011	272	0.93	1320	85.4	6.8844	3.9	0.28502	3.4	0.86	2453	34	1616	48	2096	35	65.9
NU	#37.1	0.005	131	1.12	821	82.1	6.3084	8.1	0.26540	5.9	0.73	2399	93	1517	80	2014	68	63.2
NU	#27.1	0.018	351	0.79	5887	97.1	9.5752	3.9	0.37659	3.3	0.87	2557	33	2060	59	2393	35	80.5
NU	#07.1	0.017	1081	0.17	1158	82.2	1.4774	3.6	0.11959	2.9	0.79	1476	42	728	20	921	22	49.4
NU	#10.2	1079568	1061	1.14	1647	2.6	5.8500	1.1	0.26688	1.0	0.39	2447	5	1525	13	1954	9	62.3
NU	#27.2	811904	894	1.11	903	2.1	4.8640	1.2	0.23301	1.1	0.94	2358	12	1350	14	1795	13	57.3
NU	#18.2	741745	841	2.21	1818	2.7	4.8696	1.3	0.23799	1.1	0.56	2332	9	1376	14	1797	9	59.0
NU	#64.2	604929	763	2.04	1703	2.3	4.7956	1.1	0.23477	1.2	0.64	2328	10	1359	13	1784	10	58.4
NU	#65.2	647822	847	1.80	1820	2.8	4.3381	1.1	0.21932	1.0	0.57	2264	7	1278	12	1701	9	56.5
NU	#31.2	827909	841	2.43	2166	2.1	5.8599	1.3	0.26987	1.1	0.67	2437	7	1540	14	1956	10	63.2
NU	#44.2	675928	839	1.59	1375	1.3	4.3684	1.1	0.22223	1.0	0.71	2255	5	1294	12	1706	9	57.4
NU	#48.2	821417	1123	3.21	1908	1.7	4.1329	1.6	0.20470	1.4	0.70	2300	5	1200	11	1661	9	52.2
NU	#16.2	612214	574	1.79	2081	3.2	5.8748	1.1	0.26979	1.0	0.53	2426	6	1540	14	1957	9	63.5
NU	#42.1	0.005	125	0.38	1478	83.3	6.1656	5.7	0.29832	4.9	0.86	2221	50	1682	73	1998	49	75.7
NU	#10.1	0.017	443	1.23	3088	106.8	6.3566	5.9	0.30312	5.0	0.86	2451	50	1706	75	2025	52	69.6
NU	#24.1	0.028	717	0.47	3124	92.1	7.0465	6.1	0.33393	5.5	0.90	2471	45	1856	88	2114	53	75.1
NU	#08.1	0.017	900	0.17	1378	89.7	1.9502	3.8	0.14115	3.3	0.86	1659	36	851	26	1098	25	51.3
NU	#38.1	0.010	469	0.14	2074	97.0	2.3577	4.2	0.15795	3.3	0.77	1675	51	945	29	1230	30	56.4
NU	#05.1	0.023	551	1.32	3553	94.0	6.7980	4.4	0.30939	3.8	0.88	2481	35	1737	59	2085	38	70.0
NU	#21.1	0.036	1416	1.31	1840	134.2	3.9705	6.0	0.20203	5.2	0.86	2326	53	1186	57	1625	47	51.0
NU	#40.1	0.016	508	0.87	2667	91.2	4.9510	6.0	0.23095	4.8	0.80	2255	64	1339	58	1810	51	59.4
NU	#41.1	0.044	1327	1.27	2789	88.2	5.7821	5.8	0.28537	4.9	0.84	2443	52	1618	70	1942	50	66.2
NU	#14.1	0.007	171	1.30	1500	98.6	6.8080	3.9	0.27243	3.3	0.86	2449	33	1553	46	2086	34	63.4
NU	#35.1	0.015	276	0.24	7148	87.0	9.8275	4.5	0.39847	4.1	0.92	2536	30	2161	76	2416	40	85.2
NU	#73.2	643735	596	3.49	4030	5.1	7.0231	1.2	0.30607	1.1	0.74	2516	7	1721	17	2114	10	68.4
NU	#76.2	556608	1095	0.37	1018	1.4	2.1416	1.7	0.14363	1.3	0.54	1758	5	865	8	1162	7	49.2
NU	#82.2	757478	1118	1.99	2565	4.2	3.9491	1.3	0.20825	1.2	0.87	2197	10	1219	14	1623	12	55.5

~~NU~~	~~#25.2~~	~~751280~~	~~507~~	~~1.09~~	~~14798~~	~~35.8~~	~~9.2922~~	~~1.2~~	~~0.39151~~	~~1.3~~	~~0.88~~	~~2580~~	~~6~~	~~2130~~	~~22~~	~~2367~~	~~12~~	~~82.5~~
~~NU~~	~~#42.2~~	~~570418~~	~~496~~	~~1.42~~	~~2589~~	~~2.5~~	~~6.7664~~	~~1.0~~	~~0.31126~~	~~1.0~~	~~0.90~~	~~2426~~	~~8~~	~~1747~~	~~17~~	~~2080~~	~~12~~	~~72.0~~
~~NU~~	~~#63.2~~	~~720693~~	~~938~~	~~2.06~~	~~1658~~	~~1.4~~	~~4.1105~~	~~1.3~~	~~0.21524~~	~~1.1~~	~~0.94~~	~~2200~~	~~4~~	~~1257~~	~~13~~	~~1656~~	~~10~~	~~57.1~~
~~NU~~	~~#58.2~~	~~348326~~	~~268~~	~~1.21~~	~~7061~~	~~32.8~~	~~8.2781~~	~~1.3~~	~~0.34741~~	~~1.3~~	~~0.69~~	~~2568~~	~~10~~	~~1922~~	~~21~~	~~2261~~	~~11~~	~~74.8~~
~~NU~~	~~#60.2~~	~~798564~~	~~1195~~	~~3.70~~	~~983~~	~~1.8~~	~~3.6012~~	~~1.1~~	~~0.19269~~	~~1.1~~	~~0.82~~	~~2166~~	~~8~~	~~1136~~	~~12~~	~~1550~~	~~10~~	~~52.4~~
~~NU~~	~~#61.2~~	~~782513~~	~~1114~~	~~2.74~~	~~1067~~	~~1.6~~	~~3.7980~~	~~1.0~~	~~0.20343~~	~~1.0~~	~~0.72~~	~~2165~~	~~6~~	~~1194~~	~~12~~	~~1592~~	~~9~~	~~55.1~~
~~NU~~	~~#49.2~~	~~619336~~	~~652~~	~~2.36~~	~~2770~~	~~2.4~~	~~5.9937~~	~~1.2~~	~~0.27073~~	~~1.2~~	~~0.49~~	~~2459~~	~~6~~	~~1544~~	~~14~~	~~1975~~	~~9~~	~~62.8~~
~~NU~~	~~#34.1~~	~~0.010~~	~~365~~	~~1.08~~	~~1958~~	~~83.4~~	~~4.1969~~	~~4.4~~	~~0.20201~~	~~3.7~~	~~0.86~~	~~2222~~	~~38~~	~~1186~~	~~41~~	~~1671~~	~~34~~	~~53.4~~
~~NU~~	~~#33.2~~	~~680057~~	~~344~~	~~0.96~~	~~4385~~	~~158.3~~	~~13.2438~~	~~1.1~~	~~0.48441~~	~~1.0~~	~~0.88~~	~~2798~~	~~10~~	~~2546~~	~~31~~	~~2696~~	~~15~~	~~91.0~~
~~NU~~	~~#15.2~~	~~559560~~	~~557~~	~~1.63~~	~~205~~	~~5.0~~	~~7.7541~~	~~1.3~~	~~0.27245~~	~~1.1~~	~~0.22~~	~~2873~~	~~44~~	~~1553~~	~~16~~	~~2199~~	~~26~~	~~54.1~~

[1] concentration uncertainty c.20%, [3] Concordance calculated as (^{206}Pb-^{238}U age/^{207}Pb-^{235}U age)*100, NU = not used for age calculations

supplementary table 5 LA-ICP-MS data for sample ASM13 mafic granulite

Location - lat: 557880			long:9428575				Radiogenic ratios					apparent ages						
identifier	Spot number	^{206}Pb cps	U ppm[1]	Th/U	$^{206}Pb/^{204}Pb$	1s%	$^{207}Pb/^{235}U$	2s%	$^{206}Pb/^{238}U$	2s%	Rho	$^{207}Pb/^{206}Pb$	2s (abs)	$^{206}Pb/^{238}U$	2s (abs)	$^{207}Pb/^{235}U$	2s (abs)	% conc [2]
Pop. 1.	#10.1	0.021	364	0.21	118184	10.5	7.4593	3.4	0.41863	3.0	0.86	2066	31	2254	56	2167	30	109.1
Pop. 1.	#34.1	0.020	375	0.16	128700	36.1	7.5457	3.4	0.41605	2.8	0.82	2064	34	2242	53	2177	30	108.6
Pop. 1.	#20.1	0.013	255	0.28	240763	3.3	7.2938	3.3	0.40390	2.8	0.85	2070	30	2187	51	2147	29	105.7
Pop. 1.	#39.1	0.013	262	0.35	95462	11.5	6.8695	3.5	0.39093	3.0	0.85	2052	33	2127	55	2093	31	103.6
Pop. 1.	#27.2	398116	220	0.71	14548	47.8	6.7231	1.7	0.38115	1.1	0.02	2066	25	2082	19	2076	15	100.8
Pop. 1.	#80.2	209982	126	0.53	8811	23.1	6.8571	1.7	0.38393	1.2	0.35	2087	27	2096	22	2094	16	100.4
Pop. 1.	#74.2	174988	99	0.82	2573	76.2	6.8278	1.8	0.38204	1.3	0.10	2087	32	2085	23	2089	16	99.9
Pop. 1.	#62.2	773099	472	0.22	6786	138.5	6.7244	1.7	0.37618	1.0	0.50	2088	24	2058	18	2076	15	98.6
Pop. 1.	#31.2	312802	182	0.72	14926	43.3	6.5948	1.7	0.37033	1.2	0.35	2082	26	2031	20	2058	15	97.5
Pop. 1.	#63.2	579911	347	0.28	1796	349.6	6.2332	1.7	0.35441	1.1	0.71	2055	25	1956	19	2009	15	95.2
Pop. 1.	#76.2	465156	293	0.27	5496	65.4	6.3058	1.7	0.35664	1.0	0.42	2066	25	1966	18	2019	15	95.1
Pop. 1.	#21.1	0.023	524	0.21	61029	22.9	6.1266	3.5	0.35102	3.1	0.88	2061	29	1939	52	1993	30	94.1
Pop. 1.	#49.2	560236	339	0.52	3197	162.8	6.1967	1.9	0.34892	1.2	0.69	2073	26	1929	20	2003	16	93.0
Pop. 1.	#81.2	430217	285	0.35	6747	48.0	6.0957	1.8	0.34618	1.2	0.76	2061	26	1917	20	1989	16	93.0
Pop. 1.	#29.2	416729	264	0.68	2375	276.4	5.8333	2.0	0.33592	1.4	0.88	2040	26	1866	23	1950	17	91.5
Pop. 1.	#66.2	547297	409	0.27	13601	47.5	5.1714	1.7	0.30246	1.1	0.74	2008	25	1703	16	1847	15	84.8
Pop. 1.	#60.2	642517	496	0.56	23431	22.8	5.0480	1.7	0.29581	1.1	0.77	2007	24	1670	16	1827	14	83.2
Pop. 1.	#47.2	441555	323	0.74	2802	136.9	5.0188	2.2	0.29136	1.5	0.88	2014	27	1649	22	1819	19	81.9
Pop. 1.	#57.2	670945	543	0.39	14200	47.1	4.6169	1.7	0.27515	1.0	0.27	1975	26	1567	14	1752	14	79.3
Pop. 1.	#65.2	419759	356	1.07	10075	45.9	4.5493	1.9	0.27248	1.3	0.82	1967	26	1553	18	1739	16	78.9
Pop. 1.	#19.1	0.015	431	0.30	33028	60.9	4.4111	3.9	0.26674	3.5	0.90	1933	31	1524	48	1714	32	78.9
Pop. 1.	#48.2	633464	514	0.33	3440	79.8	4.4082	1.9	0.26053	1.1	0.67	1989	27	1492	15	1713	16	75.0
Pop. 1.	#44.2	629732	550	0.61	10543	82.4	4.3311	2.2	0.25760	1.5	0.77	1981	30	1477	20	1700	17	74.6
Pop. 1.	#50.2	623791	563	0.34	5601	67.7	4.1594	1.8	0.25145	1.1	0.53	1952	28	1446	15	1665	15	74.1
Pop. 1.	#42.1	0.010	410	1.07	15333	61.2	2.6346	7.2	0.17742	5.9	0.82	1610	75	1052	57	1306	50	65.4

Pop. 1.	#40.1	0.011	480	0.37	18826	33.5	2.7367	5.5	0.18265	5.0	0.91	1707	42	1081	50	1335	39	63.3
Pop. 1.	#33.2	516131	575	0.21	11920	78.4	2.9751	1.7	0.19354	1.0	0.36	1822	26	1140	11	1401	13	62.6
Pop. 1.	#37.1	0.010	443	0.19	23931	62.4	2.4986	4.6	0.17214	3.2	0.70	1641	66	1024	31	1271	33	62.4
Pop. 1.	#12.1	0.011	452	0.15	21277	22.3	2.5539	5.1	0.17182	4.3	0.85	1644	50	1022	41	1286	36	62.2
Pop. 1.	#59.2	584424	684	0.46	12680	26.3	2.8965	1.8	0.18941	1.2	0.77	1806	26	1118	12	1380	14	61.9
Pop. 1.	#43.2	595229	693	0.51	17911	69.0	2.7492	1.9	0.18353	1.2	0.86	1768	27	1086	12	1340	14	61.4
Pop. 1.	#78.2	442400	554	0.23	6116	62.2	2.7125	1.8	0.18089	1.1	0.73	1769	26	1072	11	1331	13	60.6
Pop. 1.	#77.2	495258	653	0.33	19141	65.2	2.5927	2.6	0.17628	1.7	0.93	1734	30	1046	17	1296	19	60.3
Pop. 1.	#46.2	450276	585	0.17	219	2212.1	2.3021	1.8	0.16145	1.2	0.74	1682	26	965	10	1213	13	57.4
Pop. 2	#05.1	0.020	413	0.28	135802	11.6	5.8895	3.4	0.35897	2.9	0.87	2039	29	1977	50	1959	29	97.0
Pop. 2	#33.1	0.014	512	0.65	18409	93.7	3.2203	4.1	0.21290	3.4	0.84	1791	42	1244	39	1461	31	69.5
Pop. 2	#11.2	1120908	622	0.21	10889	74.6	5.5916	1.8	0.34968	1.0	0.21	1892	27	1933	17	1914	15	102.2
Pop. 2	#15.2	266397	165	0.46	2783	53.5	5.2136	1.7	0.32330	1.1	0.50	1908	26	1806	18	1855	15	94.6
Pop. 2	#28.2	105770	167	0.16	1284	17.4	1.8079	2.3	0.13441	1.8	0.55	1569	38	813	13	1047	15	51.8
Pop. 2	#17.2	798889	483	0.30	518	1956.1	5.5320	1.7	0.34118	1.0	0.40	1918	25	1892	17	1905	15	98.6
NU	#06.1	0.016	726	0.82	6066	13.3	2.2072	6.1	0.16417	5.2	0.85	1614	62	980	48	1180	41	60.7
NU	#11.1	0.015	582	0.26	27910	15.9	2.9548	4.2	0.20406	3.7	0.87	1813	38	1197	40	1395	32	66.0
NU	#22.1	0.014	633	0.29	21583	37.3	2.5328	4.1	0.18336	3.5	0.87	1740	37	1085	35	1281	29	62.4
NU	#27.1	0.015	300	0.29	251136	7.9	7.1471	3.3	0.40984	2.7	0.82	2072	34	2214	51	2129	29	106.9
NU	#35.1	0.011	514	0.32	17303	5.0	2.1867	5.5	0.16181	4.5	0.82	1534	61	966	41	1175	38	63.0
NU	#36.1	0.016	757	0.23	14576	66.0	2.4683	4.6	0.17909	3.8	0.84	1707	45	1062	38	1262	33	62.2
NU	#82.2	508485	655	0.83	983	350.6	2.4354	1.9	0.17114	1.1	0.78	1672	27	1018	11	1252	14	60.9
NU	#25.2	521428	608	0.55	2206	12.4	2.5341	1.7	0.16992	1.1	0.54	1765	26	1012	10	1282	13	57.3
NU	#26.2	539110	577	0.58	4139	162.9	2.9158	1.9	0.19864	1.2	0.80	1737	26	1168	13	1385	14	67.2
NU	#30.2	315075	399	0.71	3570	29.3	2.2682	1.8	0.16376	1.1	0.53	1627	27	978	10	1202	13	60.1
NU	#34.2	484615	489	0.96	6807	49.8	3.1004	1.8	0.20355	1.1	0.75	1800	26	1194	12	1432	14	66.3
NU	#41.2	415700	481	0.41	24666	52.1	2.6733	1.9	0.17583	1.2	0.56	1797	27	1044	11	1321	14	58.1
NU	#42.2	793039	541	0.21	61066	74.0	5.8364	2.4	0.32929	1.6	0.90	2073	28	1834	26	1949	21	88.5
NU	#32.2	543418	570	1.65	10563	21.6	3.1150	1.8	0.20515	1.2	0.80	1801	26	1203	13	1436	14	66.8
NU	#45.2	560268	480	0.91	208202	33.9	4.5546	1.9	0.26788	1.2	0.96	2002	31	1530	16	1741	16	76.4
NU	#58.2	539947	613	1.29	3429	234.1	2.7440	1.9	0.19009	1.2	0.55	1697	29	1122	12	1340	14	66.1
NU	#61.2	556298	966	1.60	50438	45.7	1.4582	1.8	0.12109	1.1	0.37	1357	29	737	8	913	11	54.3
NU	#64.2	545824	615	0.41	67928	33.4	2.8873	1.8	0.19329	1.0	0.62	1762	28	1139	11	1378	14	64.6
NU	#73.2	576866	699	0.68	2815	200.7	2.9213	2.0	0.19469	1.2	0.72	1772	28	1147	13	1387	15	64.7
NU	#75.2	635728	442	0.52	214096	29.1	5.7619	1.8	0.32929	1.2	0.76	2051	25	1835	19	1939	16	89.4
NU	#79.2	550550	630	0.81	6676	95.3	3.1004	1.9	0.20404	1.1	0.50	1796	29	1198	13	1432	15	66.7
NU	#23.1	0.015	951	0.11	13477	33.6	1.6045	7.9	0.13639	5.9	0.75	1444	97	824	46	969	48	57.1
NU	#08.1	0.012	218	0.78	98449	7.0	6.7471	3.7	0.36975	3.2	0.88	2049	31	2028	56	2078	32	99.0
NU	#26.1	0.019	824	1.06	7432	7.5	2.6576	6.7	0.18953	4.9	0.73	1661	84	1118	50	1314	48	67.3
NU	#14.1	0.009	175	0.50	112575	3.0	6.7659	3.1	0.39948	2.7	0.86	2072	28	2167	50	2081	28	104.6
NU	#09.2	522226	430	0.88	3728	10.4	3.3153	1.7	0.22699	2.3	0.63	1727	28	1319	14	1484	14	76.3
NU	#12.2	626757	633	1.37	7695	15.3	2.3741	1.8	0.18180	1.1	0.52	1512	28	1077	11	1234	13	71.2

~~NU~~	~~#13.2~~	~~511321~~	~~557~~	~~0.55~~	~~210~~	~~1873.9~~	~~2.2200~~	~~1.8~~	~~0.17065~~	~~1.1~~	~~0.64~~	~~1507~~	~~27~~	~~1016~~	~~10~~	~~1187~~	~~12~~	~~67.4~~
~~NU~~	~~#14.2~~	~~567273~~	~~654~~	~~0.22~~	~~10926~~	~~13.8~~	~~2.2873~~	~~1.7~~	~~0.17076~~	~~1.0~~	~~0.12~~	~~1568~~	~~26~~	~~1016~~	~~10~~	~~1208~~	~~12~~	~~64.8~~
~~NU~~	~~#10.2~~	~~551060~~	~~731~~	~~0.23~~	~~5573~~	~~10.9~~	~~1.7602~~	~~1.8~~	~~0.14563~~	~~1.1~~	~~0.37~~	~~1372~~	~~31~~	~~876~~	~~9~~	~~1031~~	~~12~~	~~63.9~~
~~NU~~	~~#16.2~~	~~536642~~	~~610~~	~~0.34~~	~~456~~	~~1316.8~~	~~2.4410~~	~~1.7~~	~~0.17925~~	~~1.1~~	~~0.48~~	~~1599~~	~~27~~	~~1063~~	~~11~~	~~1255~~	~~12~~	~~66.5~~
~~NU~~	~~#18.2~~	~~507043~~	~~588~~	~~0.18~~	~~9791~~	~~13.6~~	~~2.4341~~	~~1.7~~	~~0.17668~~	~~1.1~~	~~0.45~~	~~1621~~	~~26~~	~~1049~~	~~10~~	~~1253~~	~~12~~	~~64.7~~
~~NU~~	~~#13.1~~	~~0.013~~	~~226~~	~~0.20~~	~~60166~~	~~40.5~~	~~7.7402~~	~~4.8~~	~~0.40933~~	~~4.2~~	~~0.89~~	~~2038~~	~~39~~	~~2211~~	~~79~~	~~2200~~	~~43~~	~~108.5~~
~~NU~~	~~#25.1~~	~~0.018~~	~~485~~	~~0.87~~	~~34056~~	~~7.4~~	~~4.8272~~	~~3.3~~	~~0.29596~~	~~2.9~~	~~0.89~~	~~1963~~	~~27~~	~~1671~~	~~43~~	~~1790~~	~~28~~	~~85.1~~
~~NU~~	~~#09.1~~	~~0.011~~	~~594~~	~~0.12~~	~~14673~~	~~25.9~~	~~1.7283~~	~~4.2~~	~~0.13562~~	~~3.1~~	~~0.74~~	~~1441~~	~~54~~	~~820~~	~~24~~	~~1019~~	~~27~~	~~56.9~~
~~NU~~	~~#41.1~~	~~0.015~~	~~706~~	~~0.21~~	~~18892~~	~~45.3~~	~~2.3226~~	~~3.9~~	~~0.17364~~	~~3.4~~	~~0.87~~	~~1676~~	~~36~~	~~1032~~	~~32~~	~~1218~~	~~27~~	~~61.6~~
~~NU~~	~~#07.1~~	~~0.034~~	~~586~~	~~0.22~~	~~152250~~	~~10.6~~	~~7.4101~~	~~3.3~~	~~0.42804~~	~~2.9~~	~~0.87~~	~~2090~~	~~29~~	~~2297~~	~~56~~	~~2162~~	~~30~~	~~109.9~~
~~NU~~	~~#28.1~~	~~0.005~~	~~187~~	~~0.28~~	~~17676~~	~~102.5~~	~~3.6454~~	~~8.5~~	~~0.21581~~	~~7.4~~	~~0.87~~	~~1812~~	~~75~~	~~1259~~	~~84~~	~~1553~~	~~64~~	~~69.5~~
~~NU~~	~~#24.1~~	~~0.021~~	~~494~~	~~0.24~~	~~70621~~	~~7.9~~	~~5.8237~~	~~9.2~~	~~0.35824~~	~~8.9~~	~~0.97~~	~~2037~~	~~41~~	~~1971~~	~~151~~	~~1946~~	~~79~~	~~96.8~~
~~NU~~	~~#38.1~~	~~0.010~~	~~345~~	~~0.20~~	~~24090~~	~~74.7~~	~~3.7941~~	~~5.2~~	~~0.23095~~	~~4.3~~	~~0.83~~	~~1836~~	~~54~~	~~1339~~	~~52~~	~~1589~~	~~40~~	~~73.0~~

[1] concentration uncertainty c.20%, [3] Concordance calculated as (^{206}Pb-^{238}U age/^{207}Pb-^{235}U age)*100, NU = not used for age calculations

supplementary table 6 LA-ICP-MS data for sample ASM34B cpx-amphibolite

Location – lat: 524950 long: 9433734							Radiogenic ratios					apparent ages						
identifier	Spot number	^{206}Pb cps	U ppm[1]	Th/U	^{206}Pb/^{204}Pb	1s%	^{207}Pb/^{235}U	2s%	^{206}Pb/^{238}U	2s%	Rho	^{207}Pb/^{206}Pb	2s (abs)	^{206}Pb/^{238}U	2s (abs)	^{207}Pb/^{235}U	2s (abs)	% conc [2]
Pop. 1.	#39	0.024	364	3.48	194130	9.2	7.1303	2.9	0.40550	2.8	0.97	2063	11	2194	52	2128	26	106.4
Pop. 1.	#07	0.007	95	3.56	3269	97.7	6.5763	3.4	0.38380	3.1	0.93	2026	22	2094	56	2056	30	103.3
Pop. 1.	#14	0.022	367	3.99	140517	6.2	6.6391	3.3	0.37430	3.1	0.96	2076	16	2050	55	2065	29	98.7
Pop. 1.	#38	0.020	427	5.16	18336	52.9	5.1590	2.9	0.30781	2.8	0.98	1976	9	1730	43	1846	25	87.5
Pop. 1.	#40	0.007	132	4.51	14721	110.9	4.9789	3.2	0.29919	3.1	0.98	1969	13	1687	46	1816	27	85.7
Pop. 1.	#19	0.005	104	2.39	23631	61.1	4.5861	3.2	0.27949	2.9	0.90	1937	25	1589	41	1747	27	82.0
Pop. 1.	#34	0.041	1074	4.53	2571	65.4	4.0419	3.1	0.25454	3.0	0.98	1881	12	1462	39	1643	25	77.7
Pop. 1.	#23	0.024	534	4.60	17317	112.0	3.9252	3.1	0.24940	2.9	0.95	1862	17	1435	38	1619	25	77.1
Pop. 1.	#26	0.009	184	4.27	3344	109.9	4.0440	3.6	0.25346	3.2	0.89	1891	30	1456	42	1643	30	77.0
Pop. 1.	#22	0.007	149	3.15	7324	99.3	3.8605	3.5	0.24324	3.2	0.91	1877	27	1404	41	1605	29	74.8
Pop. 1.	#20	0.005	107	4.21	12779	143.6	3.6747	3.6	0.23307	3.2	0.88	1865	31	1351	39	1566	29	72.4
Pop. 1.	#09	0.009	205	4.49	10554	100.0	3.6277	3.1	0.23104	2.9	0.96	1870	16	1340	35	1556	25	71.6
Pop. 1.	#05	0.005	111	1.88	7629	81.4	3.3750	3.8	0.22048	3.3	0.87	1824	35	1284	39	1499	30	70.4
Pop. 1.	#21	0.004	118	3.16	28066	74.3	2.6119	3.1	0.18026	2.9	0.95	1712	17	1068	29	1304	23	62.4
Pop. 1.	#37	0.018	671	0.34	18700	6.5	2.4115	3.0	0.17108	2.9	0.97	1663	14	1018	27	1246	22	61.2
Pop. 1.	#33	0.016	493	6.21	25684	65.7	2.6328	3.1	0.17990	3.0	0.96	1742	16	1066	29	1310	23	61.2
Pop. 1.	#36	0.019	698	7.38	14464	90.6	2.2934	3.3	0.16590	3.3	0.98	1627	13	989	30	1210	23	60.8
Pop. 1.	#08	0.027	978	4.76	7275	74.0	2.4045	3.1	0.16903	2.9	0.93	1681	22	1007	27	1244	23	59.9

Pop. 1.	#27	0.011	392	0.31	14248	55.8	2.3404	3.3	0.16608	3.0	0.91	1665	26	990	27	1224	23	59.5
Pop. 1.	#35	0.018	893	0.32	66110	3.8	1.7057	3.0	0.13514	2.8	0.96	1456	15	817	22	1011	19	56.1
Pop. 1.	#24	0.010	381	0.36	3948	77.9	1.9641	4.3	0.14474	3.7	0.86	1588	41	871	30	1102	28	54.9
Pop. 1.	#25	0.008	309	1.08	11323	84.4	1.7167	4.2	0.13393	3.6	0.85	1483	42	810	27	1014	27	54.6
Pop. 1.	#10	0.009	313	5.30	2676	101.3	1.9183	3.9	0.14299	3.4	0.88	1579	36	862	27	1087	25	54.6
Pop. 1.	#28	0.017	876	0.22	45218	32.7	1.5485	3.4	0.12537	3.0	0.87	1409	32	761	21	950	21	54.0
~~NU~~	~~#41~~	~~0.032~~	~~843~~	~~7.35~~	~~6242~~	~~40.1~~	~~3.5460~~	~~2.9~~	~~0.23240~~	~~2.8~~	~~0.97~~	~~1809~~	~~14~~	~~1347~~	~~35~~	~~1538~~	~~24~~	~~74.5~~
~~NU~~	~~#42~~	~~0.027~~	~~872~~	~~5.49~~	~~2138~~	~~78.6~~	~~2.9697~~	~~3.1~~	~~0.19422~~	~~2.9~~	~~0.93~~	~~1811~~	~~21~~	~~1144~~	~~30~~	~~1400~~	~~24~~	~~63.2~~
~~NU~~	~~#12~~	~~0.016~~	~~876~~	~~0.26~~	~~18003~~	~~42.5~~	~~1.1020~~	~~2.9~~	~~0.10472~~	~~2.8~~	~~0.98~~	~~1107~~	~~13~~	~~642~~	~~17~~	~~754~~	~~16~~	~~58.0~~
~~NU~~	~~#06~~	~~0.024~~	~~1198~~	~~0.33~~	~~23867~~	~~37.7~~	~~1.3315~~	~~2.9~~	~~0.11692~~	~~2.8~~	~~0.95~~	~~1260~~	~~18~~	~~713~~	~~19~~	~~860~~	~~17~~	~~56.6~~
~~NU~~	~~#13~~	~~0.008~~	~~342~~	~~1.18~~	~~5962~~	~~87.8~~	~~1.5155~~	~~3.9~~	~~0.12127~~	~~3.6~~	~~0.93~~	~~1445~~	~~28~~	~~738~~	~~25~~	~~936~~	~~24~~	~~51.1~~
~~NU~~	~~#11~~	~~0.022~~	~~464~~	~~4.76~~	~~10010~~	~~36.9~~	~~5.2421~~	~~3.2~~	~~0.30665~~	~~3.1~~	~~0.96~~	~~2011~~	~~15~~	~~1724~~	~~46~~	~~1859~~	~~27~~	~~85.7~~

[1] concentration uncertainty c.20%, [3] Concordance calculated as (^{206}Pb-^{238}U age/^{207}Pb-^{235}U age)*100, NU = not used for age calculations

13 SUPPLEMENTARY MATERIAL 5 – GEOCHRONOLOGY COMPILATION

supplementary table 7 Summary of crystallization ages from Bacajá domain

Association	Unit	Age (Ma)	Method	Reference
Post-orogenic magmatism	Sant'ana Granodiorite	1986 ± 5	Pb-Pb TIMS, Zrn	12
		2483 ± 11*		12
		2086 ± 5 *		12
Late to post collisional magmatism	Quartzdiorite	2071 ± 3	Pb-Pb TIMS, Zrn	10
	João Jorge intrusive suite	2037 ± 33	U-Pb LA-ICP-MS, Zrn	16
		2076 ± 6	Pb-Pb TIMS, Zrn	13
		2076 ± 2		5
		2077 ± 5		15
		2077 ± 2		11
		2097 ± 7*		9
		2115 ± 9*		9
		2219 ± 3*		9
	Felicio Turvo Granite	2069 ± 6	Pb-Pb TIMS, Zrn	8
		2085 ± 4		2
	Arapari intrusive suite	2059 ± 4	Pb-Pb TIMS, Zrn	16

		2070 ± 3		11
		2072 ± 4		16
		2077 ± 3		2
		2079 ± 3		6
		2824 ± 22*		6
		2613 ± 8*		6
		2415 ± 10*		6
		2157 ± 3*		6
		2086 ± 5	U-Pb SHRIMP, Zrn	7
		2088 ± 2	Pb-Pb TIMS, Zrn	16
		2086 ± 5	U-Pb SHRIMP, Zrn	5
		2540 ± 14*	Pb-Pb TIMS, Zrn	16
Syn to late collisional magmatism	Babaquara granodiorite	2102 ± 3	Pb-Pb TIMS, Zrn	10
	Canãa Granite	2104 ± 5	Pb-Pb TIMS, Zrn	9
		2121 ± 5*		9
		2139 ± 5*		9
		2156 ± 7*		9
	Bacajaí Complex	2094 ± 4	Pb-Pb TIMS, Zrn	6
		2084 ± 2		6
		2108 ± 5*		6
		2436 ± 3*		6
		2090 ± 6		15
		2113 ± 3	U-Pb SHRIMP, Zrn	1
		2112 ± 8	Pb-Pb TIMS, Zrn	16
		2113 +35/-33	U-Pb SHRIMP, Zrn	1
		2673 ± 2*		1
		2114 ± 3	Pb-Pb TIMS, Zrn	6
		2573 ± 2*		6
Pre collisional magmatism	Metatonalite Tapiranga	2133 ± 10	Pb-Pb TIMS, Zrn	8
	Piranhaquara Monzogranite	2147 ± 5	U-Pb SHRIMP, Zrn	11
	Belo Monte Granodiorite	2154 ± 2	Pb-Pb TIMS, Zrn	2
	Oca Granodiortie	2160 ± 3	U-Pb SHRIMP, Zrn	11

	Rhyacian granitoids	2191 ± 2	U-Pb SHRIMP, Zrn	2
	Brasil Novo tonalite	2182 ± 6	U-Pb SHRIMP, Zrn	3
		2215 ± 2	Pb-Pb TIMS, Zrn	9
		2182 ± 6	U-Pb SHRIMP, Zrn	7
		2209 ± 2	Pb-Pb TIMS, Zrn	12
		2524 ± 5*		9
	Quartzmonzodiorite enclave	2440 ± 7		9
Paleoproterozoic greenstonebelts	Três Palmeiras greenstone belt	2452 ± 3	Pb-Pb TIMS, Zrn	10
		2419 ± 49	U-Pb LA-ICP-MS, Zrn	14
		2410 ± 11	Pb-Pb TIMS, Zrn	14
		2417 ± 4	Pb-Pb TIMS, Zrn	14
		2359 ± 2	U-Pb SHRIMP, Zrn	2
Granitic-gnaisse-migmatic association	Rio Bacajá Metamonalite	2313 ± 9	U-Pb SHRIMP, Zrn	1
		2338 ± 5		12
	Belmonte Village	2439 ± 4	U-Pb SHRIMP, Zrn	2
		2457 ± 5*		2
	Uruará orthogneiss	2440 ± 7	Pb-Pb TIMS, Zrn	9
		2487 ± 13	U-Pb SHRIMP, Zrn	11
		2581 ± 6*		7
		2521 ± 14*		11
		2548 ± 6*		11
		2503 ± 10		7
		2581 ± 6*		7
	Pacajá ortogneiss	2671 ± 3	U-Pb SHRIMP, Zrn	4
Archean metamorphic complexes	Aruanã complex	2585 ± 4.6	Pb-Pb TIMS, Zrn	16
		2606 ± 4		12
	Rio Preto mafic orthogranulite	2628 ± 3	Pb-Pb TIMS, Zrn	12
	Novolândia Granulite	2766 ± 70	LA-ICP-MS, Zrn	
	Cajazeiras Complex	3009 ± 27	U-Pb SHRIMP, Zrn	3
		2942 ± 4	Pb-Pb TIMS, Zrn	12
		2057 ± 7	U-Pb SHRIMP, Zrn	5

supplementary table 8 Summary of all metamorphic/migmatite ages from Bacajá domain

Unit	Sample	Lithology	metamorphic facies	Age (Ma)	Method	reference number
	PM-23A	Leucomonzogranite injection (leucossome?)	-	1962 ± 15	Sm-Nd, TIMS, grt	
	PM-23A		-	2075 ± 2	Pb-Pb, TIMS, zrn	6
Metatonalite tapiranga	MVD103A		upper amphibolite	2055 ± 6	Pb-Pb, TIMS, zrn	9
Pacajá ortogneiss	PR-125	Tonalític gneiss (migmatization?)	amphibolite	2195 ± 13	Pb-Pb, TIMS, zrn	12
Novolândia granulite	MJ-24	Paragneiss	amphibolite - granulite	2064 ± 4	U-Pb, SHRIMP, mnz	3
Ipiaçava paragneiss	MVD-21	migmatic pelitic gneiss	granulite	2024.6 ± 1.9	Sm-Nd, TIMS, grt	10
			granulite	2278.9 ± 4.8	U-Pb, ID-TIMS, zrn	10
			granulite	2109.0±8.7	U-Pb, SHRIMP, zrn	10
	MVD40	metapsammite	upper amphibolite to granulite	2074 ± 2	U-Pb, SHRIMP, zrn	10
			upper amphibolite to granulite	2208 ± 24	U-Pb, ID-TIMS, zrn	10
	MVD26B	migmatic pelitic gneiss	upper amphibolite to granulite	2123 ± 4.8	U-Pb, SHRIMP, mnz	10
			upper amphibolite to granulite	2071 ± 3.5		10
			upper amphibolite to granulite	2057 ± 3.3		10
	MVD34A	pelitic migmatite	upper amphibolite to granulite	2073.3 ± 2		10
			upper amphibolite to granulite	2132.9 ± 4.6		10
			upper amphibolite to granulite	2147.3 ± 7.4		10
Aruanã complex	PR-21A	Granitic vein (leucossome?)	-	2122 ± 18	U-Pb, LA-ICP-MS, zrn	15
Rio Preto mafic orhtogranulite	PR-87_z2	Mafic granulite	granulite	2072 ± 3	Pb-Pb, TIMS, zrn	12
Cajazeiras Complex	MJ-21	orthogneiss	-	2074 ± 8	U-Pb, SHRIMP, zrn	3

CAPÍTULO 3 – ARTIGO 2

THE MISSING RECORD OF HIGH-PRESSURE-HIGH-TEMPERATURE GRANULITE METAMORPHISM IN THE AMAZONIAN CRATON*

ABSTRACT: We present the first report of HP-HT granulitic rocks in the Amazonian Craton, which suggest a hot collisional orogen developed due to subduction-collision geodynamic processes during Paleoproterozoic times. We identify in the Bacajá domain, the occurrence of kyanite-bearing aluminous granulites interlayered as restricted lenses among charnockites and granitoids. We identified four mineral assemblages in the pelitic granulite corresponding to different metamorphic stages, which define a clockwise *P-T* path. The pre-peak metamorphism (M1) is $Grt_{(core)}$ + Bt + Ky +Rt ± Ms (Qz) recording 10–11 kbar/780–800 °C. The peak P (M2) mineral assemblage of $Grt_{(mantle)}$ + Bt + Ky +Rt (Kfs + Qz + Gr) records 10.6–14 kbar/820–850 °C. The peak T (M3) is characterized by the assemblage: $Grt_{(rim)}$ + Sil + Crd + Spl (Qz + Ilm + Gr) formed in a range of 4.4–5.3 kbar/895–915 °C. The subsequent post-peak isobaric cooling stage (M4) is characterized by $Grt_{(rim)}$ + Bt + Sil + Crd (Pl +Qz + Ilm + Gr) of a range of 700-798 °C/>3-5 kbar. The occurrence of these unique HP rocks ratifies that the younger provinces of the Amazonian Craton were developed due to orogenic processes at the margin of the Archean core, and also it supports a deep connection between the Amazonian and West Africa Cratons.

KEY-WORDS: phase equilibria modeling, high-pressure metamorphism, Columbia supercontinent, Amazonian Craton.

---

*Short communication article to be submitted

Arthur Santos da Silva [a, b, c#], Elton Luiz Dantas [a, b, d], Eliza Inez Nunes Peixoto [a], Reinhart Adolf Fuck [b], Gilmara Regina Lima Feio [c, e], José de Arimatéia Costa de Almeida [c, e], Guilherme de Oliveira Gonçalves [a, d], Roberto Ventura Santos [a, d]

[a] Programa de Pós-graduação em Geologia, Instituto de Geociências (IG), Universidade de Brasília (UnB), Brazil

[b] Grupo de Tectônica e Fluxo de Fluídos, IG-UnB, Brasília, DF, CEP 70910-900, Brazil

[c] Grupo de Mineralogia e Petrologia, Instituto de Geociências e Engenharias (IGE), Universidade Federal do Sul e Sudeste do Pará (Unifesspa), Marabá, PA, CEP 68505080, Brazil

[d] Laboratório de Estudos Geocronológicos, Geodinâmicos e Ambientais, IG-UnB, Brasília, DF, CEP 70910-900, Brazil

[e] Laboratório Multiusuário de Microanálise em Materiais, IGE, Unifesspa, Marabá, PA

Corresponding author: santosarthursilvaa@gmail.com

1 INTRODUCTION

The most internal zone of several worldwide Paleoproterozoic orogens is characterized by the presence of the most extreme baric (HP – high pressure) and thermal (UHT – ultra-high temperature) type of metamorphism (e.g., Trans-North China Orogen, Liu et al., 2019, Khondalite belt, Yin et al., 2015, Jiao-Liao-Ji Belt, Zou et al., 2017). HP pelitic granulites are of particular interest because their pressure-temperature-time (*P*-*T*-t) paths are used as a powerful tool to elucidate ancient geodynamic processes (e.g., Anderson et al., 2012) since HP granulites can form in two distinct tectonic settings. They can be related to a subduction-collision set, (e.g., Tam et al., 2012), or to a deep arc environment related to extension or magmatic underplating (e.g., Zhang et al., 2017). Recent works also suggest that HP metamorphism can be caused by local overpressure in shear zones (Chu et al., 2017; Schmalholz and Podladchikov, 2013).

The recognition of HP assemblages is challenging because later retrogressive processes can obliterate the initial HP metamorphism indicators (e.g., Liu et al., 2019; Zou et al., 2020). The recognition of kyanite associated with garnet and K-feldspar in pelitic granulites is usually the determinant factor to confirm this type of metamorphism (O'Brien and Rötzler, 2003), although kyanite is commonly not preserved in some HP-HT granulites due to LMP-HT (low to middle pressure-high temperature) overprint (e.g., Liu et al., 2019).

The reconstruction of ancient supercontinents usually explores the connection between coeval orogenic belts in distinct continents to define the paleogeography (e.g., Meert and Santosh, 2017; Zhao et al., 2002). During the Paleoproterozoic, the Amazonian and West Africa cratons were connected through the Transamazonian-Birimian orogens in the Columbia supercontinent (e.g., Grenholm et al., 2019). Metamorphic studies on granulitic rocks in these belts are rare, and so the full extension of how the deep crust evolved is still unclear. Only one locality has a confirmed occurrence of HP mafic granulite, in West Africa (Pitra et al., 2010; Triboulet and Feybesse, 1998). Although kyanite has already been described in Suriname, Guiana Shield (Kroonenberg et al., 2016 and references therein), the *P*-*T* conditions have never been precisely determined so it is still unclear if kyanite is related to an amphibolite or granulite metamorphism. Kyanite has also been described associated with a local hydrothermal process (Bijnaar et al., 2016).

In this study, based on petrography, pseudosection modeling, we present the first record of kyanite-bearing high-pressure-(ultra)high-temperature aluminous granulite in the Paleoproterozoic Bacajá domain, Amazonian Craton.

2 REGIONAL GEOLOGY

The Bacajá domain (BD) is located in the Maroní-Itacaiúnas Province, southeastern portion of the Amazonian Craton (Fig. 3.1a, b, Tassinari and Macambira, 2004). According to Vasquez and Rosa-Costa (2008 and references therein), this domain can be divided into distinct lithotectonic associations, which encompass: Archean metamorphic complexes (3.0-2.97 Ga to 2.6 Ga); a Neoarchean granite-gneiss-migmatic association (2.67-2.50 Ga); and Siderian greenstone belts (2.4-2.3 Ga). The Archean to Siderian fragments represents the basement of the orogen. They were strongly reworked during the Paleoproterozoic Transamazonian Orogeny (TO) (Cordani et al., 2000; Hurley et al., 1967; Macambira et al., 2007; Vasquez and Rosa-Costa, 2008). There are restricted lenses and xenoliths of paragneiss and aluminous granulites, among these (meta)igneous rocks with, Archean to Paleoproterozoic detrital sources and metamorphosed during the TO (Vasquez, 2006). The basement is intruded by Rhyacian-Orosirian orogenic granitoids and charnockites grouped in pre-, syn-, late-, and post-collisional suites (2.21-1.98 Ga, Macambira et al., 2009; Vasquez et al., 2008).

There are two main lines of evidence about the extent and exposure of the Bacajá domain. The first suggests that the whole Bacajá domain represents a collisional orogen (Barros et al., 2007; Macambira et al., 2009; Vasquez and Rosa-Costa, 2008). The second suggests that there is no difference between the south portion of Bacajá and north Carajás domains and that they may represent the same crust (Motta et al., 2019).

The late Rhyacian granulite-belts in the Maroní-Itacaiúnas Province (Fig. 3.1a) register similar metamorphic ages that overlap within errors, at 2.05 to 1.98 Ga in the Imataca block (Tassinari et al., 2004), 2.07 to 2.05 Ga in the Bakhuis belt (Klaver et al., 2015; Roever et al., 2003), 2.09 to 2.08 Ga and 2.05 Ga in the southeastern Amapá block (Rosa-Costa et al., 2008). In the western portion of the Bacajá domain, the granulite metamorphism dates from 2.14 to 2.05 Ga (Vasquez, 2006). Know *P-T* conditions are restricted to the Imataca block and Bakhuis belt. In the former, normal granulite temperatures were obtained (750 – 800 °C, 6 – 8 kbar, Tassinari et al., 2004), whereas in the latter, UHT granulite facies rocks were described (~900-1050 ºC, 8.5-9 kbar, Nanne et al., 2020; Roever et al., 2003).

3 GEOLOGY

The studied area is located in North Brazil (Fig. 3.1a), in the south portion of the Bacajá domain, near the proposed boundary with the Carajás domain (Fig. 3.1b, Faraco et al., 2006). This work identified distinct occurrences of lenses of aluminous granulites lenses (Fig. 3.1c), which had initially been considered part of the undifferentiated basement rocks (Cajazeiras Complex), and classified as average low/medium-pressure paragneiss (Barbosa et al., 2016). These rocks are elongated according to the regional NW-SE-trending shear zones. In the outcrop scale, two distinctive metamorphic rocks with contrasting features are observed. The first is a kyanite-bearing granulite, classified as high-pressure granulite (HP). The rocks commonly have kyanite and garnet porphyroblasts (up to 0.5 cm) (Fig 3.2a) with thin quartz-feldspar leucosomes accompanying kyanite porphyroblasts (Fig. 3.2b). Two textural types of kyanite are observed, the first is elongated according to the regional foliation (Fig. 3.2a), and the second does not align with the regional foliation (Fig. 3.2b), probably growing in a post-deformation stage. The second rock is sillimanite-bearing granulite, classified as low/medium-pressure granulite (LMP), usually showing pockets of porphyroblastic garnet and biotite (residue?) (Fig. 3.2c), and trails of sillimanite and biotite defining the foliation (Fig.3.2d), These rocks display similar geological and petrographic aspects as typical LMP described in the western section of the Bacajá domain (Corrêa et al., 2019; Vasquez, 2006). The HP and LMP granulites occur close to the recently described UHT rocks in the Bacajá domain (Silva et al in prep), from which they are divided by a major transcurrent shear zone (Fig. 3.1c).

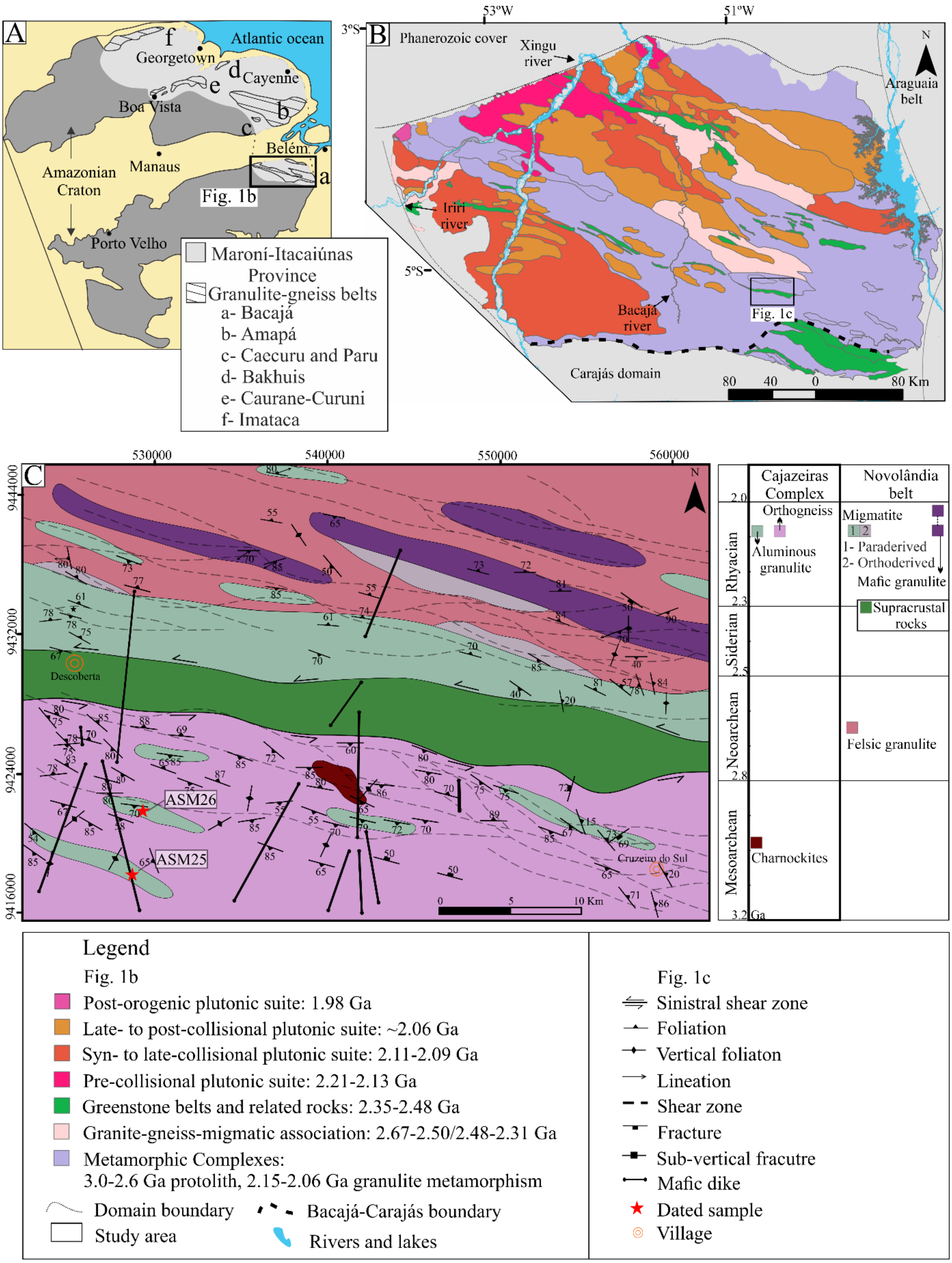

Figure 3.1 (A) the Maroní-Itacaiunas Province in Amazonian Craton (Tassinari and Macambira, 2004) and the location of the granulite-gneiss belts; (B) regional map of the Bacajá domain showing lithotectonic associations (Vasquez and Rosa-Costa, 2008 and references therein), with the localization of the studied area; (C) Geological map of the studied area (modified from Félix-Silva et al., 2016).

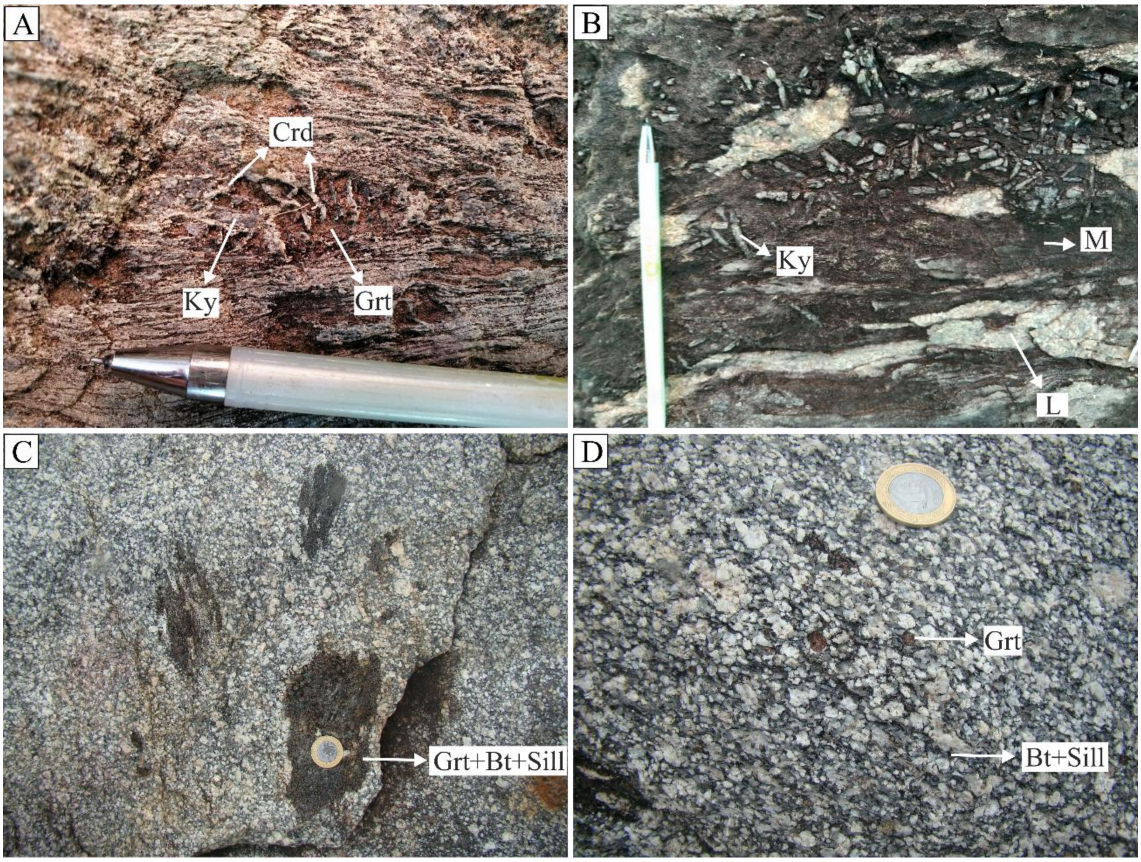

Figure 3.2 Field aspects of the HP (a, b) and LMP (c, d) metamorphic rocks of the studied area. (a) HP metamorphic rock showing kyanite and garnet porphyroblasts surrounded by cordierite coronae, (b) quartz-feldspar rich leucosome (L) associated with kyanite porphyroblasts according to the main foliation and others not aligned, interlayered with granulitic residue (M) in HP granulite; (c) garnet, biotite and sillimanite aggregates (residue?) in LMP granulite, (d) garnet crystals and biotite + sillimanite defining the foliation in an LMP granulite.

4 PETROGRAPHY AND MINERAL CHEMISTRY

Kyanite was found in two samples (ASM 25 and ASM 26) 4 km apart from each order. Sample ASM25 only shows kyanite relics. Therefore, the sample ASM26 was chosen to further investigations because it contains the best-preserved mineral assemblages and textures for *P-T* determination. ASM 26 was classified as stromatic metatexite composed of alternating residue and leucosome bands of pelitic composition. The residue contains K-feldspar, quartz, kyanite, biotite, garnet, sillimanite, and cordierite, with minor plagioclase, spinel, rutile, ilmenite, and graphite. The leucosomes are centimeters thick (Fig. 3.2b), composed mainly of quartz, feldspar and muscovite.

Garnet porphyroblasts are subdioblastic to xenoblastic, and 3-8 mm across (Fig. 3.3a, d). They contain inclusions of biotite, K-feldspar, quartz, kyanite, rutile (in core and mantle), sillimanite (rim), and rutile/ilmenite (Fig. 3.3a, b, c); the grains are usually surrounded by coronae formed of cordierite-sillimanite-spinel-quartz-ilmenite, biotite also occurs associated with cordierite and sillimanite, but not with spinel. Garnet compositions (Fig. S1, supplementary table 1) are dominated by almandine (X_{Alm} 0.751-0.861) and pyrope (X_{Prp} 0.067-0.188), with relatively low grossular (X_{Grs} 0.015-0.037) and spessartine (X_{Sps} 0.031-0.049) contents. Garnet porphyroblasts exhibit compositional zoning. The core is enriched in pyrope with a rim-ward decrease and almandine poor with a rim-ward increase. The core is relatively enriched in grossular with a rim-ward drop and poor in spessartine with a rim-ward increase.

Kyanite occurs as tabular idioblastic grains small grains as associated with garnet (1-3 mm), usually inclusion-poor (Fig. 3.3d), or as larger grains (5-10 mm) in the rock matrix (Fig. 3.3e) with inclusions of biotite, quartz, and tiny muscovite grains (Fig. 3.3d, e). Along cracks and in grain boundaries it is altered to sillimanite (Fig. 3.3d, f). It is surrounded by cordierite-sillimanite-spinel coronae and later biotite (Fig. 3.3d).

Biotite mostly occurs as idio- to subdioblastic flakes of 0.5–2 mm in the matrix, inclusions in garnet and cordierite, and grown after garnet and kyanite/sillimanite (Fig. 3.3d, f). Some biotite flakes grow along the cracks of garnet (Fig. 3.3a, b, c), suggesting later formation. Biotite composition varies according to its textural aspect (supplementary table 1). Biotite included in garnet has TiO_2 between 3.19 and 4.69 wt% the X_{Mg} shows variations between 0.42 and 0.43. Biotite included in kyanite porphyroblasts shows TiO_2 content of 2.51-4.32 wt% and X_{Mg} of 0.28-0.30. Biotite formed in coronae around garnet and kyanite shows TiO_2 3.07-3.56 wt% and 2.66-2.97 wt% and X_{Mg} of 0.30-0.33 and 0.30-0.31, respectively. Biotite in the rock matrix shows X_{Mg} of 0.29-30 and lower TiO_2 content (2.21-3.07 wt%) than on inclusions in garnet.

Cordierite occurs as xenoblastic grains replacing garnet and forming coronae around kyanite together with sillimanite and spinel, this variety is usually altered to pinite (Fig. 3a, e). Cordierite also occurs as medium-grained xenoblastic grains in the rock matrix, with sillimanite and biotite inclusions (Fig. 3.3f). Both types do not show substantial compositional variations (supplementary table 1) in Fe-Mg distribution (X_{Mg} 0.47-0.55). Around garnet, its X_{Mg} is higher (0.48-0.55) compared with the ones around kyanite (0.40-0.41). In the rock matrix, it has the X_{Mg} of 0.40-0.47.

Rutile occurs as small grains (<0.1 mm) within garnet core/mantle and kyanite (Fig. 3.3b), usually replaced by ilmenite. Ilmenite is located at the garnet boundary associated with coronas and as xenoblastic grains in the rock matrix. Spinel occurs only as rounded grains of < 0.05 mm across associated with sillimanite and cordierite in coronae around garnet and kyanite (Fig. 3.3b, f). They are enriched in Fe^{2+} with variable amounts of Fe^{3+} (6.83-7.53 wt%), and

ZnO (3.17-2.88 wt%). Graphite grains occur inside garnet, cordierite, and kyanite porphyroblasts and in the rock matrix.

Quartz and K-feldspar occur as xenoblastic grains of ~2.5 mm across in the rock matrix. Some smaller (<1 mm) grains of quartz and K-feldspar are found as inclusions in garnet. K-feldspar usually contains plagioclase lamellae (Fig. 3.3g). Xenoblastic plagioclase grains are rare (1mm) and show normal zoning from the core (X_{An} 0.42) to the rim (X_{An} 0.32) (supplementary table 1).

Based on the textural observations and mineral compositions presented above, a sequence of four assemblages is inferred, including pre-peak (M1) represent by the inclusions in coarse-grained garnet and kyanite, including rutile, biotite and muscovite. The P_{max} (M2) assemblage consists of garnet, biotite, kyanite and rutile. The T_{max} (M3) is represented by garnet, cordierite, sillimanite, spinel and ilmenite. Post-peak cooling (M4) is marked by the widespread formation of biotite, plagioclase and sillimanite in the rock matrix, as well as some garnet and ilmenite. K-feldspar, graphite, and quartz seem to be stable throughout all the assemblages.

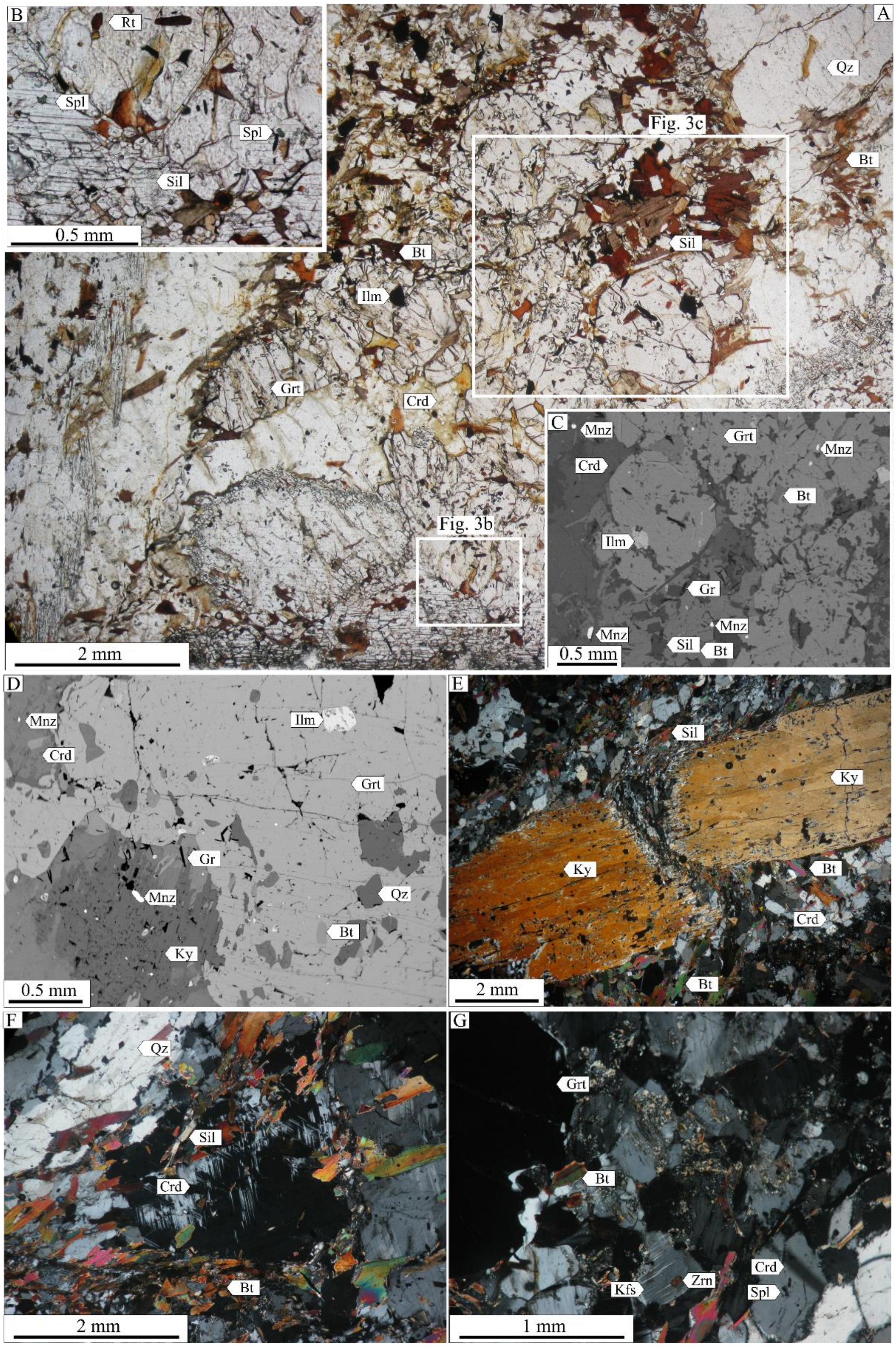

Figure 3.3 Representative photomicrographs of the HP granulite. PPL = parallel-polarized light and CPL = cross-polarized light. (A) Garnet porphyroblast showing small inclusions of biotite, rutile and quartz. It is replaced by cordierite, sillimanite, K-feldspar and later biotite (PPL). (B) Detail of garnet boundary in contact with silimanite containing spinel inclusion (PPL); (C) BSE image showing garnet boundary surrounded by biotite + silimanite + quartz coronae and distinct monazite textural aspects; (D) BSE image of kyanite in contact with garnet porphyroblast; (E) fractures kyanite porphyroblast surrounded by cordierite and small spinel and replaced by silimanite (CPL); (F) Cordierite showing typical twinning associated with biotite and sillimanite

(CPL); (G) K-feldspar with plagioclase lamellae and cordierite with spinel inclusions surrounding garnet porphyroblast (CPL). Mineral abbreviations are after Whitney and Evans (2010).

5 P-T CONDITIONS

5.1 PSEUDOSECTION MODELING

P-T pseudosection was modeled with Theriak-Domino (De Capitani and Petrakakis, 2010), using the MnNCKFMASHTO system. The bulk composition of the sample ASM26 was measured by XRF in ALS laboratories, Brazil (Tab. 3.1). We used the internally consistent thermodynamic dataset of Holland and Powell (1998) with the re-parameterized a-x models: garnet, biotite, and silica melt (White et al., 2007), orthopyroxene (White et al., 2002), cordierite, staurolite (Holland and Powell, 1998), plagioclase and K-feldspar (Holland and Powell, 2003), and an ideal model for ilmenite and spinel-hercynite. Pure phases included water, sillimanite, kyanite, andalusite, rutile and quartz. The water content was defined using the $T\text{-}M_{(H2O)}$ diagram to ensure that water content is enough to saturate the final stage assemblage (e.g., Korhonen et al., 2012). Furthermore, the presence of graphite, ilmenite and absence of magnetite indicates a low oxygen fugacity. Thus we chose the minimum (XFe_2O_3 = 0.01) for calculation (e.g., Indares et al., 2008).

P-T pseudosection (Fig. 3.4) was conducted within a range of 3–15 kbar, 700–950 °C, and it is contoured by the isopleths of grossular in garnet (X_{Grs}). The solidus occurs above 700 ºC. The pattern of X_{Grs} isopleths is mainly affected by calcium-bearing phases. In the plagioclase-absent fields, the isopleths are near vertical and useful temperature indicators. However, in plagioclase-present areas, most of the isopleths are sub-parallel and useful pressure indicators. Rutile becomes stable at the expense of ilmenite above 8.5 kbar, coexisting in a short P interval. Cordierite is stable only below 6.5 kbar.

Although such a *P-T* diagram based on the preserved composition is not suitable to model prograde metamorphic evolution, as the present bulk composition represents a relatively refractory composition after the melt loss (e.g., Wu et al., 2017) the abundance of minerals and composition variations does not change significantly in the supra-solidus field (e.g., Groppo et al., 2010). Therefore, the latest stage of prograde evolution (M1 – pre-peak) defined by the highest X_{Grs} (~0.0.38–0.035) is roughly estimated in a *P-T* range of ~11–11.5 kbar/~770–790 °C. The mineral assemblage of M2 (P_{max}) is Kfs-Grt-Bt-Ky-Rt-Qz-L, with XGrs = ~0.027–0.033 stabilized at ~10.6–14 kbar/~820–850 °C. It is followed by the M3 (T_{max}) stage with assemblages of Kfs-Grt-Sil-Spl-Ilm-Qz-L, and its grossular proportion is X_{Grs} = ~0.018–0.015, within *P-T* ranges of ~4.4–5.3 kbar/~895–915 °C. The cooling stage M4 is featured by biotite and plagioclase-in reactions with conditions of ~700-798 °C/>3-5 kbar until the final melt solidified (T < 750 °C, if P = 6 kbar).

Table 3.1 Bulk rock composition of the sample ASM26

X-ray fluorescence whole-rock composition (wt%)												
Sample	SiO_2	TiO_2	Al_2O_3	FeO^T	MnO	MgO	CaO	Na_2O	K_2O	P_2O5	LOI	Total
ASM26	61.64	0.62	20.37	6.74	0.11	2.13	0.21	0.7	4.08	0.08	1.53	98.21
Normalized molar proportions used for modeling (mol%)												
Sample	SiO_2	TiO_2	Al_2O_3	FeO	Fe_2O_3	MnO	MgO	CaO	Na_2O	K_2O	H_2O	-
ASM09A	56.85	0.43	22.15	5.20	0.01	0.09	2.93	0.21	1.25	4.80	6.90	-

5.2 CONVENTIONAL THERMOBAROMETRY

The X_{Grs} isopleths are vertical in most fields of the pseudosection (Fig. 3.3b), so reliable temperature estimates were retrieved from the pseudosection and used for pressure calculation with the GBAQ (Wu, 2017), later the Ti-in-biotite thermometer (Wu and Chen, 2015) was also used based on the GBAQ pressures. For pre-peak (M1 late prograde evolution) using biotite in the garnet core, we obtained a mean pressure of 11 ± 1.8 kbar (T=750 ºC), a *P-T* condition similar to the pseudosection calculations. The temperature for this stage is also consistent with the Ti-in-biotite of 780 ± 14 ºC (considering a possible P=10.5 kbar). For the P_{max} stage (M2), we obtained pressure of 13.5 ± 1.8 (T=830 ºC) and temperatures of 849 ± 14 ºC (P=13.5 kbar), using biotite in kyanite porphyroblasts and garnet mantle. For the $T_{max,}$ as there is no biotite in this stage, we could not use both conventional methods. Still, we suggest that the temperature is higher than ~850 ºC because it was the maximum temperature obtained in the biotite-bearing assemblages (P_{max}). For the isobaric cooling, we obtained pressures of 5.5 ± 1.8 kbar (T=700 ºC) and temperature of 705 ± 14 ºC (P=5.5 kbar) using biotite from the rock matrix.

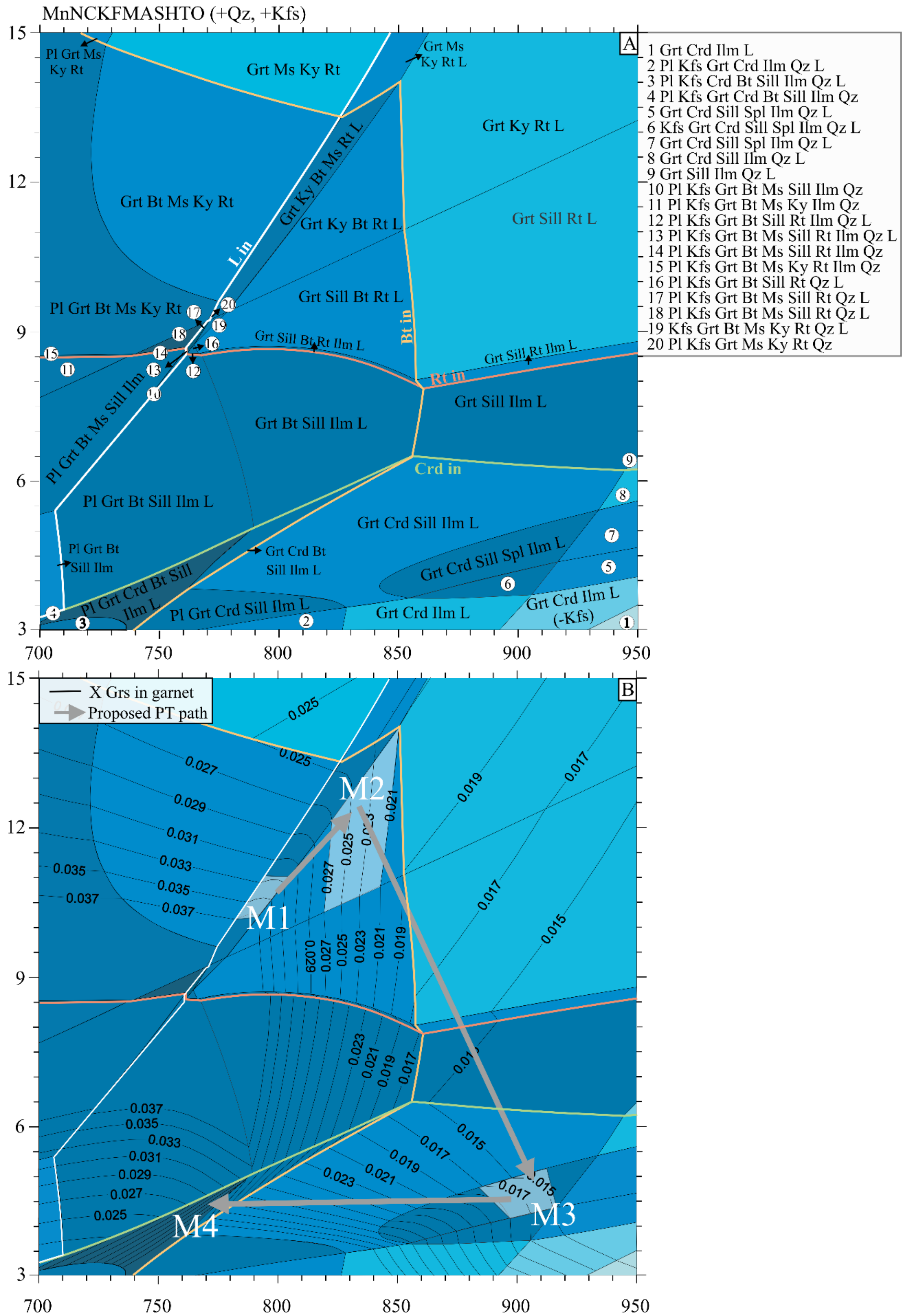

240 Figure 3.4 (A) *P-T* pseudosection from the sample ASM-26A, (B) *P-T* evolution based on mineral assemblages and X_{Grs} in garnet.

6 DISCUSSION

6.1 *P*-*T*-(t) EVOLUTION

The integration of pseudosection modeling, X_{Grs} in garnet, and conventional thermobarometry defined four stages of metamorphic evolution, encompassing a pre-peak stage with an increasing *P*-*T* reaching HP conditions that were followed by a decompression-heating reaching HT conditions and later near isobaric cooling (Table 2).

The late prograde (M1 – pre-peak) stage is inferred by the inclusion mineral inclusions in garnet cores and in kyanite porphyroblasts, which consist of Kfs-$Grt_{(core)}$-Ky-Bt-Rt-Qz-L±Ms. The *P*-*T* conditions are mainly based on the highest grossular content in the garnet inner core (X_{Grs} = ~0.037-0.35), which defines *P*-*T* conditions of ~10–11 kbar/~780–800 °C and is consistent with the conventional calculations 11 ± 1.8 kbar (if T = 750 ºC, GBAQ barometer) and 783 ± 14 °C (if P = 11 kbar, Ti-in-biotite temperatures derived from biotite in the garnet core).

The P_{max} (M2) is characterized by the continuous growth of garnet, exhaustion of muscovite, and the typical high-pressure assemblage Kfs-$Grt_{(mantle)}$-Ky (O'Brien and Rötzler, 2003) accompanied by Bt-Rt-Qz-L. The X_{Grs} = ~0.027-0.23 in the garnet mantle define a *P*-*T* range of ~10.6–14 kbar/~820–850 °C. These conditions are similar to the pressure obtained by the GBAQ barometer 13.5±1.8 kbar (if T=830ºC). The temperatures are also consistent with the results (849±14 °C, P = 13.5 kbar) derived from Ti-in-biotite inclusions in kyanite porphyroblasts.

The P_{max} is followed by continuous decompression and heating, accompanied by a decreasing abundance of biotite until M3, when the rock reaches the peak temperature (M4). The growth of garnet rims features the T_{max} (Fig. S1), exhaustion of biotite, the transition from kyanite to sillimanite (Fig. 3.3d, g), replacement of rutile by ilmenite, and formation of cordierite-spinel-sillimanite-ilmenite coronas around garnet and kyanite porphyroblasts (Fig. 3.3d, e). The inferred assemblage of M3 is Kfs-Grt-Crd-Sil-Spl-Ilm-Qz-L, and the corresponding grossular component is X_{Grs} = ~0.017–0.015 (garnet rim), which defines a *P*-*T* range of ~4.4–5.3 kbar/~895–915 °C.

The cooling stage from M3 to M4 is characterized by the formation of biotite around garnet and kyanite, along with the widespread formation of cordierite, biotite and sillimanite in the rock matrix (Fig. 3.3f), until reaching the solidus. This stage is marked by the continuous rise of XAlm and decrease of XPrp towards the garnet rim (Fig. S1), which represents diffusion-controlled retrograde zoning due to the exchange of Fe–Mg between garnet rims and biotite during cooling (Florence and Spear, 1991). The inferred assemblage is Pl-Kfs-Grt-Crd-Bt-Sil-Ilm-Q-L, and the corresponding *P-T* conditions are estimated around >3-5 kbar/~700-798 °C in the pseudosection and confirmed by conventional calculations of 5.5 ± 1.8 kbar (T=700 ºC), and ~710 ± 25ºC (if P= 5 kbar),

The time evolution of these rocks is still unsolved due to the absence of consistent geochronological data. Macambira et al. (2007) reported a single age of 2075 ± 8 Ma (SHRIMP zircon age) of an orthogneiss sample in the studied area, interpreted as the time of metamorphism. On a regional scale, the ages of ca. 2.07 Ga are interpreted as low-pressure granulite metamorphism (Vasquez, 2006) and as the cooling age to the solidus in UHT migmatic rocks (Silva et al in prep). Therefore, the previous age of 2.07 Ga obtained by Macambira et al (2007) is considered as the probable LMP imprint on our studied samples, in the transition to the M3-M4 stage, during cooling to the solidus.

Table 3.1 Summary of petrography, geochronological and isotopic data, and *P-T* conditions (pseudosection) for the representative HP granulite from south Bacajá and other confirmed occurrences in the Transamazonian-Birimian orogens

Locality	Lithology	Mineral assemblages	Ages (Ga)	*P-T* conditions			
				Pre-peak	P_{max}	T_{max}	Post-peak
South Bacajá domain, Amazonian Craton	Garnet-cordierite-silimanite-kyanite granulitic residue	Pre-peak: Grt$_{(core)}$ + Bt + Rt ± Ky ± Ms (Qz) Peak P: Grt$_{(mantle)}$ + Bt + Ky +Rt (Kfs + Qz + Gr) Peak T: Grt$_{(rim)}$ + Sill + Crd + Spl (Qz + Ilm + Gr) Post-peak: Grt$_{(rim)}$ + Bt + Sill + Crd (Pl +Qz + Ilm + Gr)	n.d HP 2.06 (U)HT	10–11 kbar	10.6–14 kbar	4.4–5.3 kbar	>3-5 kbar
				780–800 °C	820–850 °C	895–915 °C	700-798°C
Kouibli area, Man Rise, West Africa Craton[1]	Mafic granulite	M1: Grt + Cpx +Amp + Pl + Rt +Ilm + Qz M2: Opx + Cpx + Pl +Amp +Ilm + Mt	2.03 Sm-Nd grt-WR	M1: 13 kbar 850 ºC M2: <7 kbar 700–800 ºC			

n.d – not determined, [1] Pitra et al., (2010)

6.2 HP METAMORPHISM IN THE TRANSAMAZONIAN-BIRIMIAN OROGENIES AND IMPLICATIONS FOR COLUMBIA ASSEMBLY

The majority of the Columbia supercontinent reconstructions place the Amazonian and the West Africa cratons together, based on the common geological history and sinistral shear zones (e.g., Grenholm et al., 2019; Meert and Santosh, 2017). There are several granulite-gneiss belts developed and/or reworked in both cratons during the Columbia assembly (e.g., Amapá Block, Milhomem Neto and Lafon, 2019; Cauarani-Curuni, Fraga et al., 2008). Among these Transamazonian-Birimian orogens, only two localities register high-pressure granulite metamorphism so far (Fig. 3.5). At the Archean KénémaMan block margin, West Africa Craton (~13 kbar/850ºC, at 2.03 Ga, Pitra et al., 2010), and south Bacajá domain, Amazonian Craton (~13.5 kbar/820-850ºC, before 2.07 Ga, this work).

According to Pitra et al. (2010), the HP mafic granulites from West Africa were formed during the convergence of the hot and weak Paleoproterozoic (Birimian) juvenile crust against the colder Archean craton as well as the syn-tectonic emplacement of juvenile magmas induced local re-heating and thickening of the Archean crust close to the boundary zone.

We propose a hot collisional setting for the formation of HP-HT pelitic granulites in the Bacajá domain similar to the one proposed by Pitra et al. (2010), based on the following evidence: (i) the consistent clockwise *P-T* path, which is related to subduction and collision processes that brought sedimentary protoliths to a deep crustal level (<40 km) where they experienced HP granulite-facies conditions. Clockwise *P-T* paths with significant decompression heating/cooling or isothermal decompression have been generally considered as metamorphic evidence of collisional tectonics (e.g., Liu et al., 2019; Thompson and England, 1984); (ii) there is also a large volume of juvenile syn-tectonic granitoids in Bacajá (e.g., Barros et al., 2007; Macambira et al., 2009) that could have induced heating and thickening of the boundary zone between the cold Archean Carajás and the hot Bacajá domains. This proposition ratifies previous tectonic models proposed for the evolution of the Bacajá domain, taken as a collisional orogen (e.g., Barros et al., 2007).

The similarity of geological processes in the evolution of both HP occurrences implies that similar collisional tectonics were taking place during the Paleoproterozoic and support previous reconstruction models of the Columbia supercontinent (e.g., Meert and Santosh, 2017; Zhao et al., 2002).

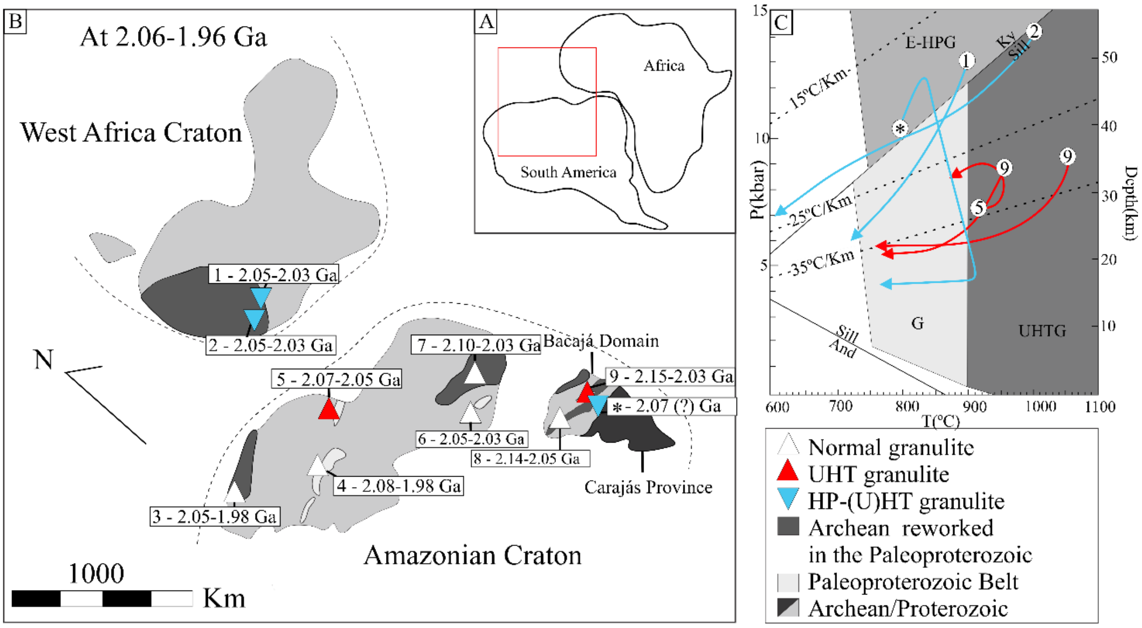

Figure 3.5 Reconstruction of Maroni-Itacaiúnas Province (Amazonian Craton) and south West Africa Craton at 2.06-1.96 Ga after Grenholm et al (2019). (A) localization of the area in reconstructed South America and Africa during the Columbia assembly. (B) Localization of all the granulite facies rocks in both Amazonian and West Africa Craton with their respective metamorphic ages, *- data obtained in this work, 1- Pitra et al., (2010), 2 Triboulet and Feybesse (1998), 3 – Imataca Complex, Tassinari et al., (2004), 4- Cauarane-Curuni belt, Fraga et al., (2008), 5 – Bakhuis Belt, Roever et al., (2003), 6 – Tartarugal Complex, 7- Amapá Block, Rosa-Costa et al., (2003), 8 – West Bacajá domain, Vasquez, (2006), 9 – South Bacajá, Silva et al. (in prep); (C) All *P-T* paths of UHT and HP granulites in the Transamazonian-Birimian orogens; G- granulite, UHTG- ultra-high temperature granulite, E-HPG – eclogite-high-pressure granulite after Brown (2007).

6.3 RELATIONSHIP BETWEEN LMP AND HP GRANULITES

Understanding the relationship between low-medium and high-pressure granulites is a challenging task, because HP granulites exposures are rare, even in regions where they have already been reported (e.g., Zou et al., 2020), which makes it more difficult to determine their link. The lack of exposure allows to rise two main hypothesis: (i) if the dominant LMP types represent retrogressive HP rocks (e.g., (Zou et al., 2017), or (ii) local HP assemblages were formed due to an overpressure scenario (e.g., Chu et al., 2017).

In the Bacajá domain and coeval granulite belts within the Amazonian craton, the metamorphic conditions are mainly based on conventional thermobarometry and petrogenetic grids (Feio et al., 2016; Roever et al., 2003; Tassinari et al., 2004), only local studies using pseudosection modeling and feldspar thermometry are available (Klaver et al., 2015; Nanne et al., 2020). However, based on accessible information, it is safe to state that LPM granulites are the most common aluminous rock type in these belts, typical for several other orogens worldwide (e.g., Harley, 1989).

In this study, we consider the newly identified kyanite-bearing granulites (ASM26), implying in an early HP metamorphism, the kyanite relics (ASM25) and also the consider the previous reports of typical LMP in Bacajá (Corrêa et al., 2019; Vasquez, 2006) in an attempt to understand their relationship between them and the implications for the evolution of the Bacajá domain.

The distance between two kyanite-bearing samples (~4 km), the kyanite relics (ASM25), and the well-preserved kyanite crystals in weakly foliated domains (Fig. 3.2a) overrules the possible overpressure scenario for the origin of these HP rocks (Chu et al., 2017), and suggests that they were formed due to subduction-collision processes at greater depths than the LMP types. Also, the local random growth of kyanite (Fig. 3.2b) might suggest that they were locally formed due to post-collisional metasomatic/hydrothermal processes in shear zones(Bijnaar et al., 2016). However, the local occurrence of kyanite relics in other samples away from the main shear zones discards this possibility, and suggests a regional more than local metamorphism. Therefore, the studied samples suggest that at least some LMP are retrogressive HP granulites.

6.4 PALEOPROTEROZOIC TECTONICS IN THE AMAZONIAN CRATON

The current models for the Amazonian Craton compartmentation are based mainly on granitoids geochronology, isotope geochemistry and geophysics (Santos et al., 2006; Tassinari and Macambira, 2004). These authors consider that the Archean Carajás nucleus was stable at the end of the Archean and that the other provinces represent collisional and/or accretionary orogens surrounding the older core. Nonetheless, a precise compartmentation model also needs a systematic metamorphic study (e.g., Santosh et al., 2012), which is lacking for most of the Amazonian Craton. Our new finding fully supports the idea that the newer provinces represent orogens developed at the Archean core border, given that the HP rocks were formed in subduction-collision processes on the margin of the Carajás Domain.

This study also supports the hypothesis that modern plate tectonics have been established at least since the Paleoproterozoic era in the Amazonian Craton, which is typical for other cratons (e.g., North China Craton, Zou et al., 2020) because only tectonic processes related to plate tectonics can generate such crustal thickening and following rapid uplift that characterized the obtained *P-T* path in this work.

7 CONCLUSIONS

We present the first record of high-pressure-high-temperature aluminous granulite in the Amazonian Craton. These granulites follow a typical clockwise *P-T* path with increasing pressure and temperature until the peak pressure conditions, followed by decompression-heating reaching high-temperature conditions and later isobaric cooling probably at ca. 2.06 Ga. They were probably formed during a subduction-collision process between the Bacajá and Carajás blocks during the Transamazonian Orogeny. This study also suggests that modern plate tectonics has been established at least since the Paleoproterozoic era in the Amazonian Craton.

ACKNOWLEDGMENTS

Unifesspa is acknowledged for the previous works in the study area and support in fieldwork. The staff of Laboratório de Microssonda is thanked for their support during EPMA analysis. This study was financed in part by the Coordenação de Aperfeiçoamento de Pessoal de Nível Superior - Brasil (CAPES) - Finance Code 001. The authors thank Instituto Nacional de Ciência e Tecnologia – Estudos Tectônicos (INCT-ET, CNPq grant n° 46.5613/2014-4, CAPES grant 88887.136350/2017-00, FAPDF grant n° 193.001.263/2017) for financial support and to CAPES scholarship granted to the first author (n° 88882.347170/2019-01). ELD, RAF acknowledge CNPq research grants.

REFERENCES

Anderson, J.R., Payne, J.L., Kelsey, D.E., Hand, M., Collins, A.S., Santosh, M., 2012. High-pressure granulites at the dawn of the Proterozoic. Geology 40, 431–434. https://doi.org/10.1130/G32854.1

Barbosa, C.H.T., Almeida, J.A.C., Feio, G.R.L., 2016. Petrografia das rochas do Complexo Cajazeiras, vila Cruzeiro do Sul, Domínio Bacajá, Cráton Amazônico, in: 48º Congresso Brasileiro de Geolgia. Sociedade Brasileira de Geologia, Porto Alegre.

Barros, C.E. de M., Macambira, M.J.B., Santos, M.C. da C., Silva, D.C.C., Palmeira, L.C.M., Sousa, M.M., 2007. Estruturas sinmagmáticas e idade de zircão de granitos (evaporação de Pb) paleoproterozóicos da parte leste do domínio Bacajá, Província Maroni-Itacaiúnas. Rev. Bras. Geociências 37, 293–304.

https://doi.org/10.25249/0375-7536.2007373293304

Bijnaar, G., Van Bergen, M.J., Wong, T.E., 2016. The kyanite quartzite of Bosland (Suriname): Evidence for a Precambrian metamorphosed alteration system. Geol. en Mijnbouw/Netherlands J. Geosci. 95, 447–465. https://doi.org/10.1017/njg.2016.38

Chu, X., Ague, J.J., Podladchikov, Y.Y., Tian, M., 2017. Ultrafast eclogite formation via melting-induced overpressure. Earth Planet. Sci. Lett. 479, 1–17. https://doi.org/10.1016/j.epsl.2017.09.007

Cordani, U.G., Sato, K., Teixeira, W., Tassinari, C.G., Basei, M.A.S., 2000. Crustal evolution of the South American Platform. Tecton. Evol. South Am. 19–40.

Corrêa, L.C., Meira, V.T., Vasquez, M.L., 2019. Metamorfismo dos paragnaisses da região oeste do Domínio Bacajá, estado do Pará: dados preliminares, in: 16º Simpósio de Geologia Da Amazonia. Sociedade Brasileira de Geologia, Manaus, pp. 626–630.

De Capitani, C., Petrakakis, K., 2010. The computation of equilibrium assemblage diagrams with Theriak/Domino software. Am. Mineral. 95, 1006–1016. https://doi.org/10.2138/am.2010.3354

Faraco, M.T.L., Vale, A.G., Santos, J.O.S., Luzardo, R., Ferreira, A. l., Oliveira, M.A., Marinho, P.A.C., 2006. Levantamento geológico da região ao norte da Província Carajás in: Souza, in: Souza, Valmir; Horbe, A.C. (Ed.), Contribuições a Geologia Da Amazônia. Sociedade Brasileira de Geologia, Belém, pp. 32–44.

Feio, G.R.L., Sousa, J.T., Almeida, J.A.C., 2016. Geotermobarometria de granulitos do Complexo Novolândia, porção sul do Domínio Bacajá, Província Tranzamazonas, in: 48º Congresso Brasileiro de Geolgia. Sociedade Brasileira de Geologia, Porto Alegre.

Félix-Silva, A.D., Almeida, J.A.C., Feio, G.R.L., 2016. Mapa e banco de dados geológico da vila Cruzeiro do Sul, porção sul do Domínio Bacajá, in: 48º Congresso Brasileiro de Geolgia. Sociedade Brasileira de Geologia, Porto Alegre.

Florence, F.P., Spear, F.S., 1991. Effects of diffusional modification of garnet growth zoning on P-T path calculations. Contrib. to Mineral. Petrol. 107, 487–500. https://doi.org/10.1007/BF00310683

Fraga, L.M., Reis, N.J., Agnol, R.D., 2008. Cauarane - Coeroeni Belt – the Main Tectonic Feature of the Central Guyana Shield , Northern Amazonian Craton. Unknown 2–5.

Grenholm, M., Jessell, M., Thébaud, N., 2019. A geodynamic model for the Paleoproterozoic (ca. 2.27–1.96 Ga) Birimian Orogen of the southern West African

Craton – Insights into an evolving accretionary-collisional orogenic system. Earth-Science Rev. 192, 138–193. https://doi.org/10.1016/j.earscirev.2019.02.006

Groppo, C., Rubatto, D., Rolfo, F., Lombardo, B., 2010. Early Oligocene partial melting in the Main Central Thrust Zone (Arun valley, eastern Nepal Himalaya). Lithos 118, 287–301. https://doi.org/10.1016/j.lithos.2010.05.003

Harley, S.L., 1989. The origins of granulites: A metamorphic perspective. Geol. Mag. 126, 215–247. https://doi.org/10.1017/S0016756800022330

Holland, T., Powell, R., 2003. Activity-compositions relations for phases in petrological calculations: An asymetric multicomponent formulation. Contrib. to Mineral. Petrol. 145, 492–501. https://doi.org/10.1007/s00410-003-0464-z

Holland, T.J.B., Powell, R., 1998. An internally consistent thermodynamic data set for phases of petrological interest. J. Metamorph. Geol. 16, 309–344.

Hurley, P.., Almeida, F.F.., Melcher, G.., Cordani, U.., Rand, J., Kawashita, K., Vandoros, P., Pinson, W.., Fairbairn, H.., 1967. Test of continental drift by means of radiometric ages. Science (80-.). 495–500.

Indares, A., White, R.W., Powell, R., 2008. Phase equilibria modelling of kyanite-bearing anatectic paragneisses from the central Grenville Province. J. Metamorph. Geol. 26, 815–836. https://doi.org/10.1111/j.1525-1314.2008.00788.x

Klaver, M., de Roever, E.W.F., Nanne, J.A.M., Mason, P.R.D., Davies, G.R., 2015. Charnockites and UHT metamorphism in the Bakhuis Granulite Belt, western Suriname: Evidence for two separate UHT events. Precambrian Res. 262, 1–19. https://doi.org/10.1016/j.precamres.2015.02.014

Korhonen, F.J., Powell, R., Stout, J.H., 2012. Stability of sapphirine + quartz in the oxidized rocks of the Wilson Lake terrane, Labrador: Calculated equilibria in NCKFMASHTO. J. Metamorph. Geol. 30, 21–36. https://doi.org/10.1111/j.1525-1314.2011.00954.x

Kroonenberg, S.B., De Roever, E.W.F., Fraga, L.M., Reis, N.J., Faraco, T., Lafon, J.M., Cordani, U., Wong, T.E., 2016. Paleoproterozoic evolution of the Guiana Shield in Suriname: A revised model. Geol. en Mijnbouw/Netherlands J. Geosci. 95, 491–522. https://doi.org/10.1017/njg.2016.10

Liu, H., Li, X.P., Kong, F.M., Santosh, M., Wang, H., 2019. Ultra-high temperature overprinting of high pressure pelitic granulites in the Huai'an complex, North China Craton: Evidence from thermodynamic modeling and isotope geochronology. Gondwana Res. 72, 15–33. https://doi.org/10.1016/j.gr.2019.02.003

Macambira, M.J.B., Pinheiro, V.L., Armstrong, R.A., 2007. A fronteira Arqueano-Paleoproterozoico no SE do Cráton Amazônico: abrupta no tempo, suave na tectônica?, in: X Simpósio de Geologia Da Amazônia. pp. 97–100.

Macambira, M.J.B., Vasquez, M.L., Silva, D.C.C., Galarza, M.A., Barros, C.E.M., Camelo, J.F., 2009. Crustal growth of the central-eastern Paleoproterozoic domain, SW Amazonian craton: Juvenile accretion vs. reworking. J. South Am. Earth Sci. 27, 235–246. https://doi.org/10.1016/j.jsames.2009.02.001

Meert, J.G., Santosh, M., 2017. The Columbia supercontinent revisited. Gondwana Res. 50, 67–83. https://doi.org/10.1016/j.gr.2017.04.011

Milhomem Neto, J.M., Lafon, J.M., 2019. Zircon U-Pb and Lu-Hf isotope constraints on Archean crustal evolution in Southeastern Guyana Shield. Geosci. Front. 10, 1477–1506. https://doi.org/10.1016/j.gsf.2018.09.012

Motta, J.G., Souza Filho, C.R. d., Carranza, E.J.M., Braitenberg, C., 2019. Archean crust and metallogenic zones in the Amazonian Craton sensed by satellite gravity data. Sci. Rep. 9. https://doi.org/10.1038/s41598-019-39171-9

Nanne, J.A.M., De Roever, E.W.F., de Groot, K., Davies, G.R., Brouwer, F.M., 2020. Regional UHT metamorphism with widespread, primary CO2-rich cordierite in the Bakhuis Granulite Belt, Surinam: A feldspar thermometry study. Precambrian Res. 350. https://doi.org/10.1016/j.precamres.2020.105894

O'Brien, P.J., Rötzler, J., 2003. High-pressure granulites: Formation, recovery of peak conditions and implications for tectonics. J. Metamorph. Geol. 21, 3–20. https://doi.org/10.1046/j.1525-1314.2003.00420.x

Pitra, P., Kouamelan, A.N., Ballevre, M., Peucat, J.J., 2010. Palaeoproterozoic high-pressure granulite overprint of the Archean continental crust: Evidence for homogeneous crustal thickening (Man Rise, Ivory Coast). J. Metamorph. Geol. 28, 41–58. https://doi.org/10.1111/j.1525-1314.2009.00852.x

Roever, E.W.., Lafon, J., Delor, C., Cocherie, A., Rossi, P., Guerrot, C., Portel, A., 2003. The Bakhuis ultrahigh-temperature granulite belt (Suriname): I. petrological and geochronological evidence for a counterclockwise P-T path at 2.07-2.05 Ga. Géologie la Fr. 175–205.

Rosa-Costa, L.T., Lafon, J.M., Cocherie, A., Delor, C., 2008. Electron microprobe U-Th-Pb monazite dating of the Transamazonian metamorphic overprint on Archean rocks from the Amapá Block, southeastern Guiana Shield, Northern Brazil. J. South Am. Earth Sci. 26, 445–462. https://doi.org/10.1016/j.jsames.2008.05.007

Rosa-Costa, L.T., Ricci, P., Lafon, J., Vazquez, M.L., Carvalho, J., Klein, E., Macambira, E., 2003. Geology and geochronology of Archean and Paleoproterozoic domains of southwestern Amapa and northwestern Para, Brazil, southeastern Guiana shield. Géologie la Fr. 101–120.

Santos, J.O.S., Hartmann, L.A., Faria, M.S., Riker, S.R., Miguel, M., Almeida, M.E., Mcnaughton, N.J., 2006. a Compartimentação Do Cráton Amazonas Em Províncias : Avanços Ocorridos No Período 2000-2006, in: IX Simpósio de Geologia Da Amazônica. Sociedade Brasileira de Geologia, Belém.

Santosh, M., Liu, S.J., Tsunogae, T., Li, J.H., 2012. Paleoproterozoic ultrahigh-temperature granulites in the North China Craton: Implications for tectonic models on extreme crustal metamorphism. Precambrian Res. 222–223, 77–106. https://doi.org/10.1016/j.precamres.2011.05.003

Schmalholz, S.M., Podladchikov, Y.Y., 2013. Tectonic overpressure in weak crustal-scale shear zones and implications for the exhumation of high-pressure rocks. Geophys. Res. Lett. 40, 1984–1988. https://doi.org/10.1002/grl.50417

Tam, P.Y., Zhao, G., Zhou, X., Sun, M., Guo, J., Li, S., Yin, C., Wu, M., He, Y., 2012. Metamorphic P-T path and implications of high-pressure pelitic granulites from the Jiaobei massif in the Jiao-Liao-Ji Belt, North China Craton. Gondwana Res. 22, 104–117. https://doi.org/10.1016/j.gr.2011.09.006

Tassinari, C.C.G., Macambira, M.J.., 2004. A evolução tectônica do Craton Amazônico, in: Mantesso-Neto, V., Bartorelli, A., Carneiro, C.D.R., Brito Neves, B.B. (Eds.), Geologia Do Continente Sul Americano: Evoluc¸ Ão Da Obra de Fernando Flávio Marques Almeida. São Paulo, pp. 471–486.

Tassinari, C.C.G., Munhá, J.M.U., Teixeira, W., Palácios, T., Nutman, A.P., Sosa, C.S., Santos, A.P., Calado, B.O., 2004. The Imataca Complex, NW Amazonian Craton, Venezuela: Crustal evolution and integration of geochronological and petrological cooling histories. Episodes 27, 3–12. https://doi.org/10.18814/epiiugs/2004/v27i1/002

Thompson, A.B., England, P.C., 1984. Pressure - temperature - time paths of regional metamorphism II. their inference and interpretation using mineral assemblages in metamorphic rocks. J. Petrol. 25, 929–955. https://doi.org/10.1093/petrology/25.4.929

Triboulet, C., Feybesse, J., 1998. Les métabasites birimiennes et archéennes de la région de Toulepleu-lty (Côte d’Ivoire) : des roches portées à 8 kbar et 14 kbar au

Paléorprotérozoïque. Académie Sci. Paris , Sci. la terre des planètes 61–66.

Vasquez, M.L.., Rosa-Costa, L.T.., 2008. Geologia e Recursos Minerais do Estado do Pará : Sistema de Informações Geográficas – SIG : texto explicativo dos mapas Geológico e Tectônico e de Recursos Minerais do Estado do Pará, 1st ed. Brazilian Geological Service, CPRM, Belém.

Vasquez, M.L., 2006. Geocronologia em zircão, monazita e granada e isótopos de Nd das associações litológicas da porção oeste do Domínio Bacajá: evolução crustal da porção meridional da Província Maroni-Itacaiúnas – Sudeste Do Cráton Amazônico. Universidade Federal do Pará.

Vasquez, M.L., Macambira, M.J.B., Armstrong, R.A., 2008. Zircon geochronology of granitoids from the western Bacajá domain, southeastern Amazonian craton, Brazil: Neoarchean to Orosirian evolution. Precambrian Res. 161, 279–302. https://doi.org/10.1016/j.precamres.2007.09.001

White, R.W., Powell, R., Clarke, G.L., 2002. The interpretation of reaction textures in Fe-rich metapelitic granulites of the Musgrave Block, Central Australia: Constraints from mineral equilibria calculations in the system. J. Metamorph. Geol. 20, 41–55. https://doi.org/10.1046/j.0263-4929.2001.00349.x

White, R.W., Powell, R., Holland, T.J.B., 2007. Progress relating to calculation of partial melting equilibria for metapelites. J. Metamorph. Geol. 25, 511–527. https://doi.org/10.1111/j.1525-1314.2007.00711.x

Wu, C.M., 2017. Calibration of the garnet–biotite–Al2SiO5–quartz geobarometer for metapelites. J. Metamorph. Geol. 35, 983–998. https://doi.org/10.1111/jmg.12264

Wu, C.M., Chen, H.X., 2015. Revised Ti-in-biotite geothermometer for ilmenite- or rutile-bearing crustal metapelites. Sci. Bull. 60, 116–121. https://doi.org/10.1007/s11434-014-0674-y

Wu, J., Zhang, Huafeng, Zhai, M., Guo, J., Li, R., Wang, H., Zhao, L., Jia, X., Wang, L., Hu, B., Zhang, Haidong, 2017. Paleoproterozoic high-pressure-high-temperature pelitic granulites from Datong in the North China Craton and their geological implications: Constraints from petrology and phase equilibrium modeling. Precambrian Res. 303, 727–748. https://doi.org/10.1016/j.precamres.2017.09.011

Yin, C., Zhao, G., Sun, M., 2015. High-pressure pelitic granulites from the Helanshan Complex in the Khondalite Belt, North China craton: Metamorphic P-T path and tectonic implications. Am. J. Sci. 315, 846–879. https://doi.org/10.2475/09.2015.03

Zhang, Z., Xiang, H., Dong, X., Li, W., Ding, H., Gou, Z., Tian, Z., 2017. Oligocene HP metamorphism and anatexis of the Higher Himalayan Crystalline Sequence in Yadong region, east-central Himalaya. Gondwana Res. 41, 173–187. https://doi.org/10.1016/j.gr.2015.03.002

Zhao, G., Cawood, P.A., Wilde, S.A., Sun, M., 2002. Review of global 2.1-1.8 Ga orogens: Implications for a pre-Rodinia supercontinent. Earth-Science Rev. 59, 125–162. https://doi.org/10.1016/S0012-8252(02)00073-9

Zou, Y., Zhai, M., Mitchell, R.N., Zhao, L., Zhou, L., Liu, B., Wang, Y., Chen, M., 2020. Discovery of kyanite in typically cordierite/sillimanite-bearing low- to medium-pressure pelitic granulites from the Jiaobei terrain, North China Craton. Precambrian Res. 342. https://doi.org/10.1016/j.precamres.2020.105677

Zou, Y., Zhai, M., Santosh, M., Zhou, L., Zhao, L., Lu, J., Shan, H., 2017. High-pressure pelitic granulites from the Jiao-Liao-Ji Belt, North China Craton: A complete P-T path and its tectonic implications. J. Asian Earth Sci. 134, 103–121. https://doi.org/10.1016/j.jseaes.2016.10.015

SUPLLEMENTARY MATERIAL 1 -METHODOLOGY

FIELDWORK

Fieldwork in the Cruzeiro do Sul covered an area of 1050 Km² in a scale 1:100.00, a total of 36 points were described. The work was carried out during 2019 to investigate the structural pattern and stratigraphic relations between the distinct lithological associations that outcrop in that area. Geological mapping was supported by geochronology, geophysical, and petrographic surveys.

PETROGRAPHY AND MINERAL CHEMISTRY

Petrography was performed using the microscope Zeiss Axio Imager.A2M with transmitted and reflected light. The main reactions and microstructural features were described as proposed by Passchier and Trouw (2005) and Vernon (2004). Mineral abbreviations follow Whitney and Evans (2010).

Representative samples were selected for mineral chemical analyses based on petrography. The analyzed minerals were garnet. orthopyroxene. clinopyroxene. cordierite. amphibole. plagioclase. biotite. K-feldspar. and spinel. Polished thin sections of the selected samples were submitted to wavelength dispersive spectroscopy (WDS) quantitative analyses at the Laboratório de Microssonda (LABSON) from Universidade de Brasília (UnB) using a JEOL JXA-8230 electron microprobe analyzer. Analyses were performed under the following operating conditions: a column accelerating voltage of 15 kV; a current of 10 nA; an analysis time of 10 s. The standards used for instrument calibration were andradite (Ca and Fe), microcline (Si. Al and K), olivine (Mg), albite (Na), pyrophanite (Ti and Mn), vanadinite (V and Cl), nickel oxide (Ni), chromium trioxide (Cr), and Celestine (Sr). All thin sections selected for electron microprobe analyses were previously carbon-coated. The data was treated using the software AX (Holland; http://www.esc.cam.ac.uk/astaff/holland/ax.html)8

SUPPLEMENTARY MATERIAL 2 - FIGURES

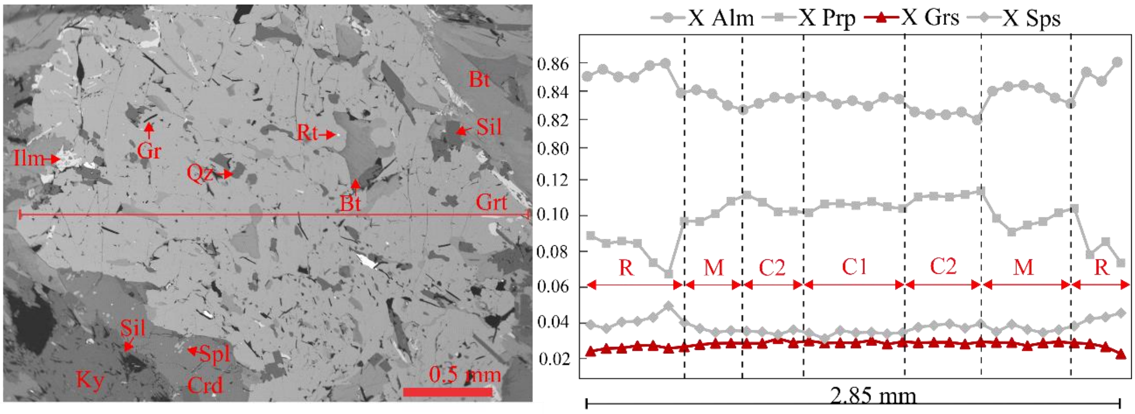

Supplementary figure 1 schematic drawing of garnet porphyroblasts and their inclusions, and respective growth zones, and a representative garnet profile from sample ASM26

SUPPLEMENTARY MATERIAL 2 – MINERAL COMPOSITIONS

supplementary table 9 representative EPMA analyses from sample ASM26

Mineral	Grt						Bt								Pl		Crd						Mineral	Spl	
-	Min	Max	Min	Max	Min	Max	Min	Max	Min	Max	Min	Max	Min	Max	Min	Max	Min	Max	Min	Max	Min	Max	-	-	-
texture	Core		Mantle		Rim		In Grt		In Ky		Around Grt		Matrix		Matrix		around Grt		Around Ky		Matrix		texture	Around Grt	Around ky
SiO_2 (wt%)	36.56	36.38	36.92	35.75	37.45	36.08	34.71	34.56	34.39	34.25	34.27	34.45	34.33	34.70	60.50	59.15	47.66	47.72	47.38	48.24	47.96	47.57	SiO_2	0.06	0.00
TiO_2	0.00	0.06	0.04	0.06	0.00	0.00	4.69	3.19	2.51	4.32	3.07	3.56	2.78	3.07	0.00	0.01	0.01	0.00	0.02	0.00	0.00	0.00	TiO_2	0.00	0.00
Al_2O_3	21.69	21.72	20.94	21.44	20.86	21.98	18.22	19.03	18.70	17.76	17.52	17.55	19.48	19.64	25.87	26.82	32.72	32.34	32.59	32.29	32.19	32.44	Al_2O_3	59.86	59.71
Cr_2O_3	0.03	0.12	0.02	0.03	0.03	0.02	0.24	0.04	0.01	0.03	0.05	0.15	0.02	0.02	0.01	0.00	0.00	0.03	0.00	0.00	0.00	0.00	Cr_2O_3	0.15	0.11
Fe_2O_3	0.45	0.38	0.00	2.05	0.00	0.73	0.00	0.00	0.00	0.00	0.00	0.00	0.00	0.00	0.22	0.07	0.42	1.80	0.00	0.00	0.00	2.04	Fe_2O_3	6.83	7.53
FeO	36.18	35.94	36.36	34.80	37.60	36.72	19.10	20.55	23.03	23.52	25.15	24.05	23.59	23.23	0.00	0.00	11.28	9.35	12.81	12.97	12.84	10.07	FeO	28.82	28.11
MnO	1.53	1.66	1.60	1.59	1.50	2.02	0.00	0.02	0.12	0.09	0.05	0.04	0.07	0.06	0.00	0.00	0.12	0.12	0.23	0.22	0.24	0.21	MnO	0.14	0.22
MgO	2.51	2.38	2.89	2.88	2.24	1.92	8.08	8.24	5.55	5.03	6.15	6.66	5.74	5.86	0.04	0.00	5.88	6.31	4.84	4.96	4.80	5.06	MgO	1.10	1.84
CaO	1.08	1.25	0.71	0.97	0.51	0.63	0.00	0.00	0.00	0.00	0.00	0.00	0.00	0.00	6.28	8.28	0.02	0.04	0.04	0.05	0.03	0.04	CaO	0.04	0.00
Na_2O	0.03	0.02	0.02	0.00	0.02	0.03	0.17	0.15	0.10	0.05	0.14	0.13	0.13	0.13	6.88	6.20	0.11	0.27	0.05	0.08	0.09	0.28	Na_2O	0.11	0.00
K_2O	0.01	0.00	0.01	0.00	0.03	0.00	9.26	9.21	8.85	8.12	8.67	9.25	9.09	8.88	0.66	0.11	0.09	0.22	0.01	0.01	0.00	0.66	K_2O	0.00	0.02
total	100.07	99.91	99.51	99.57	100.24	100.13	94.47	94.99	93.26	93.17	95.07	95.84	95.23	95.59	100.46	100.64	98.31	98.20	97.97	98.82	98.15	98.37	ZnO	3.17	2.88
O	12						11								8		18						NiO	0.16	0.19
Si	2.954	2.946	2.997	2.906	3.027	2.928	2.669	2.656	2.721	2.712	2.691	2.677	2.667	2.673	2.676	2.618	4.983	4.980	4.998	5.044	5.047	4.988	Totoal	100.44	100.61
Ti	0.000	0.004	0.003	0.003	0.000	0.000	0.271	0.184	0.149	0.257	0.181	0.208	0.162	0.178	0.000	0.000	0.001	0.000	0.002	0.000	0.000	0.000	O	4	
Al(total)	2.066	2.073	2.005	2.055	1.988	2.103	1.652	1.724	1.744	1.658	1.622	1.608	1.784	1.784	1.349	1.399	4.033	3.979	4.053	3.980	3.993	4.010	Si	0.002	0.000
Cr	0.002	0.008	0.001	0.002	0.002	0.001	0.015	0.002	0.001	0.002	0.003	0.009	0.001	0.001	0.000	0.000	0.000	0.002	0.000	0.000	0.000	0.000	Ti	0.000	0.000
Fe3+	0.027	0.023	0.000	0.126	0.000	0.044	0.000	0.000	0.000	0.000	0.000	0.000	0.000	0.000	0.007	0.002	0.033	0.142	0.000	0.000	0.000	0.161	Al(total)	2.018	2.002
Fe2+	2.445	2.434	2.468	2.366	2.542	2.492	1.228	1.321	1.524	1.558	1.651	1.563	1.533	1.497	0.000	0.000	0.986	0.816	1.130	1.134	1.130	0.883	Cr	0.003	0.002
Mn	0.104	0.114	0.110	0.109	0.103	0.139	0.000	0.001	0.008	0.006	0.003	0.003	0.005	0.004	0.000	0.000	0.011	0.011	0.021	0.019	0.021	0.019	Fe3+	0.147	0.161
Mg	0.302	0.287	0.350	0.349	0.270	0.232	0.926	0.944	0.655	0.594	0.720	0.771	0.665	0.673	0.003	0.000	0.916	0.981	0.761	0.773	0.753	0.791	Fe2+	0.689	0.668
Ca	0.093	0.108	0.062	0.084	0.044	0.055	0.000	0.000	0.000	0.000	0.000	0.000	0.000	0.000	0.298	0.393	0.002	0.004	0.005	0.006	0.003	0.004	Mn	0.003	0.005
Na	0.004	0.003	0.003	0.000	0.003	0.005	0.025	0.022	0.015	0.008	0.021	0.020	0.020	0.019	0.590	0.532	0.022	0.055	0.010	0.016	0.018	0.057	Mg	0.047	0.078

K	0.001	0.000	0.001	0.000	0.003	0.000	0.908	0.903	0.893	0.820	0.868	0.917	0.901	0.873	0.037	0.006	0.012	0.029	0.001	0.001	0.000	0.089	Ca	0.001	0.000
XGrs	0.032	0.037	0.021	0.029	0.015	0.019	-	-	-	-	-	-	-	-	-	-	-	-	-	-	-	-	Na	0.006	0.000
XAn	-	-	-		-	-	-	-	-	-	-	-	-	-	0.32	0.42	-	-	-	-	-	-	K	0.000	0.001
XMg	-	-	-	-	-	-	0.43	0.42	0.30	0.28	0.30	0.33	0.30	0.31	-	-	0.48	0.55	0.40	0.41	0.40	0.47	-	-	-

$X_{Grs} = Ca^{2+}/(Ca^{2+} + Mg^{2+} + Fe^{2+})$; $X_{Mg} = Mg^{2+}/(Fe^{2+} + Mg^{2+})$; $X_{An} = Ca^{2+}/(Ca^{2+} + Na^{+} + K^{+})$;

Min and Max are depending on the XGrs content for Grt, TiO_2 in Bt, XAn for Pl, XMg for Crd

CAPÍTULO 4 – CONCLUSÕES

1 CONCLUSÕES

A partir da integração de dados de campo, petrográficos, termobarométricos e geocronológicos das rochas de alto grau metamórfico da região sul do domínio Bacajá, obtiveram-se as seguintes conclusões:

As rochas agrupadas no cinturão granulítico Novolândia apresentam diferentes protólitos (sedimentares e ígneos) que foram metamorfisados em fácies granulito e apresentam graus variados de migmatização. Os resíduos granulíticos aluminosos registram a primeira ocorrência de metamorfismo de temperaturas ultra altas no domínio Bacajá. Eles apresentam uma trajetória P-T horária com picos de temperatura entre 950~1050 ºC e pressões entre ~8-9 kbar, seguidos por um processo de descompressão-resfriamento e posterior resfriamento isobárico. Os granulitos aluminosos apresentam fontes detríticas predominantemente arqueanas entre ~3,3-2,6 Ga. Os granulitos félsicos apresentam idade mínima de cristalização em ~2.74 Ga e registram um evento de perda de Pb ou metamorfismo em ~2,56 Ga. Os granulitos máficos e anfibolitos foram cristalizados em ~2,08 Ga e ~2,03 Ga, respectivamente. Todas as litologias estudadas apresentam idades de metamorfismo entre 2,1-2,05 Ga que foram interpretadas como idades de resfriamento até o *solidus* e uma idade mais nova em 1,92 Ga. Essas rochas foram provavelmente formadas em um ambiente orogênico quente e as temperaturas ultra altas também foram propiciadas devido ao intenso magmatismo granitoide juvenil difundido no domínio Bacajá e magmatismo máfico local registrado na área de estudo.

As lentes de granulitos aluminosos que ocorrem entre as rochas ortoderivadas do Complexo Cajazeiras apresentam duas associações distintas: as portadoras de cianita (alta pressão) e as portadoras de silimanita (média ou baixa pressão). As rochas com cianita apresentam uma trajetória P-T horária com aumento progressivo de P-T até condições de alta pressão, com a formação da assembleia típica Kfs + Grt + Ky, seguida por descompressão e aquecimento até atingir temperaturas altas a ultra altas e seguido por resfriamento isobárico. A idade regional de ~2,07 Ga foram interpretadas como a superposição do metamorfismo de média-baixa pressão registrados nessas rochas. Essas associações foram formadas provavelmente em um ambiente de subducção-colisão, na interface entre os domínios Bacajá e Carajás. A presença de rochas de alta pressão indica que o processo de subducção-colisão era atuante pelo menos desde o Paleoproterozoico no domínio Bacajá.